University of Southampton

# Numerical Studies of Wave Propagation Phenomena in Shock and Expansion Tubes

by

Te-Wei Po

A thesis submitted for the degree of

Master of Philosophy

Aerodynamics and Flight Mechanics Research Group

School of Engineering Sciences

Faculty of Engineering and Applied Science

June 2001

UNIVERSITY OF SOUTHAMPTON

**ABSTRACT**

FACULTY OF ENGINEERING AND APPLIED SCIENCE

DEPARTMENT OF AERONAUTICS AND ASTRONAUTICS

Master of Philosophy

NUMERICAL STUDIES OF WAVE PROPAGATION PHENOMENA IN
SHOCK AND EXPANSION TUBES

By Te-Wei Po


The results from numerical simulations of one-dimensional inviscid and two-dimensional axisymmetric viscous simulations in shock and expansion tubes are presented. A code using the HLLC approximate Riemann solver developed by Toro et al [43] was used to carry out the simulations.

The ability of the code to provide accurate solutions for one-dimensional Euler equations has been verified by examining Sod's ideal shock tube problem and the details in shock wave and contact surface were investigated. It shows that the details were accurate as the initial pressure ratio across a primary diaphragm was low. For high initial pressure ratio across the primary diaphragm, the numerical simulations of the simple shock tube problem were carried out. It shows that there is an initial overestimation in shock speed. The computed heat transfer rate compared to Mirels' theory and the duration of the test time were investigated.

The tailoring interface technique used widely in shock tube researches was considered because of the possibility to increase the test time. The simulations for inviscid flow with tailored, under-tailored and over-tailored conditions were carried out and the results are given here. Some simulations for viscous flow were also carried out and there was a pressure loss in the driver chamber due to heat transfer. The acoustic transverse wave propagation phenomenon caused by the interaction between heat transfer and pressure loss was investigated.

The simulations of expansion tube with two different pressure ratios across the secondary diaphragm were carried out. The details of wave propagation of the primary shock interaction with the secondary diaphragm and the interaction between the reflected shock and the secondary expansion were investigated. The durations of the test gas with good quality were also discussed here.

# Acknowledgements

I would like to thank my supervisor, Dr. Owen Tutty, and my advisor, Dr. Graham Roberts, for providing me the assistance and guidance that more than I could desire during the past few years. And for that I am most grateful.

I would like to thank the Department of Education in Taiwan for the scholarship that provides me a chance to learn more knowledge. I would also like to thank Cultural Division, Taipei Representative Office in the U.K. for their support and encouragement, in particular the last few years.

I would deeply like to thank my parents, Heng-Chi Po and Yi-Wen Chao for their encouragement, enthusiasm and financial support during my formal education. I would also like to thank my special brother and aunties for their encouragement and care.

I would like to thank a special person in my life, Chien-Chien, for her support, faith, encouragement and patience.

And to those dear friends I have known for a few years in Southampton, I couldn't thank you all enough for your warm encouragement when things were not going very well. I would like to thank Salvador Navarro-Martinez for his help in the codes for this thesis. I would like to thank Ed Rayner for his great help to sort out many computer problems for five years!

*To memory of my grand father, Hsi-Che Chao, in my mother side*

He was an officer in the Chinese Air Force, as a fighter pilot initially and as aircraft maintenance officer in the front line later, during the Sino-Japanese War. His spirit and personal characteristics affected my view of life.

I'd like to share this poem with people, for the right but hard decision, that my family made for me, and which has decided which path I am walking now after I lost most of hearing ability during my childhood.

## *The Road Not Taken*

TWO roads diverged in a yellow wood,
And sorry I could not travel both
And be one traveller, long I stood
And looked down one as far as I could
To where it bent in the undergrowth;

Then took the other, as just as fair,
And having perhaps the better claim,
Because it was grassy and wanted wear;
Though as for that, the passing there
Had worn them really about the same,

And both that morning equally lay
In leaves no step had trodden black.
Oh, I kept the first for another day!
Yet knowing how way leads to way,
I doubted if I should ever come back.

I shall be telling this with a sigh
Somewhere ages and ages hence:
Two roads diverged in a wood, and I--
I took the one less travelled by,
And that has made all the difference.

~Robert Frost (1874-1963)

# Contents

# Chapter 1

# Introduction

Since Chunk Yeager proved the sound barrier was a myth a little over 50 years ago, engineers have been striving for the ultimate speed machine. Commercial passenger carriers wanted to beat their competitors to point destinations and the military sought a rapid delivery for weapons and ordnance. Hence, the concepts of hypersonic aerospace transport vehicle have been developed, and the research projects include Reusable Launch Vehicle (RLV) such as X-33 (Venture Star) and X-38 are undertaken in USA and other countries. The goals of RLV projects are to develop the technologies which to achieve single-stage-to-orbit vehicle, and to prove the flight performance by experiments.

In early space vehicles, they needed to have efficient control abilities and withstand the severe aerodynamic and thermal loading when they were cruising at hypersonic speed or entering the Earth's atmosphere. The problems involved in hypersonics can be defined as compressible flow field problems. To study the physical phenomena of these problems, ground based experimental facilities have been the usual approach investigating tools. However, it appears to be impossible to mimic the real conditions requested in ground based experiments. Therefore, computational fluid dynamics (CFD), which plays an important role of aerospace technologies, has been developed and applied in aerodynamics and aerothermodynamics.

CFD is a powerful tool brought by the intensive use of computers for studying fluid mechanics problems. Although the costs of numerical simulations are cheaper than ground based experiments, they have many uncertainties and inaccuracies. Numerical methods applied to fluid dynamics have been progressively increasing accuracy and speed, extending its use among scientists. A wide range of techniques has applied to different systems with acceptable results. However, the computational techniques have increased in accuracy progressively. In this work, the computational approach has been used to investigate the phenomena of wave propagation in shock and expansion tubes. The numerical approach is based on a Godunov's method [14] with the HLLC Riemann solver [43, 44]. The HLLC solver code used to carry out the work is developed for that created by Amaratunga [1] and, later, by Murray [32].

Previous researches have been carried out to simulate the shock/expansion tube flows by using the finite-volume method [20, 33] and Total Variation Diminishing (TVD) methods [48, 49 and 50]. Most of their works were to simulate the large size high enthalpy pulse facilities such as the NASA Langley expansion tube. In this work, for the first time shock/expansion tube flows have been simulated with the HLLC solver code, although some researchers have carried out shock tube investigations with the HLLC solver for low diaphragm pressure ratios, and short length of the tubes, primarily as test cases.

This work presented in this thesis is divided into five parts. First, Chapter 1 will give a brief introduction of CFD, then Chapter 2 will present numerical techniques of modelling inviscid flow, then Chapter 3 will describe the numerical implementations of the viscous solver and some results of shock and expansion tube simulations will be discussed in Chapter 4. Finally, some conclusions and recommendations for future work will be given in Chapter 5.

# Chapter 2

# Numerical Methods

## 2.1 Governing Equations

The governing equation of flow field problems requires a set of equations which can describe the physical phenomena of the flow field. In this section, the forms of the Euler equations and the Navier-Stokes equations are defined as follows.

### 2.1.1 Euler Equations

In general, the basic inviscid compressible flow field is described by the inviscid Euler equations for an ideal gas. The equations can effectively represent a non-physical fluid of zero viscosity without rotational factors and chemical reactions involved in the flow field. For describing two-dimensional or axisymmetric flow problems the conservation form of the inviscid Euler equations can be written in Cartesian space co-ordinates system as follows:

$$\frac{\partial U}{\partial t} + \frac{\partial F}{\partial x} + \frac{\partial G}{\partial y} + \alpha H = 0 \tag{2.1}$$

where $\alpha = 0$ for two-dimensional and $\alpha = 1$ for axisymmetric problem, and vectors $U$, $F$, $G$ and $H$ can be given by

$$U = \begin{bmatrix} \rho \\ \rho u \\ \rho v \\ \rho E \end{bmatrix}, \quad F = \begin{bmatrix} \rho u \\ \rho u^2 + P \\ \rho uv \\ u(\rho E + P) \end{bmatrix}, \quad G = \begin{bmatrix} \rho v \\ \rho vu \\ \rho v^2 + P \\ v(\rho E + P) \end{bmatrix}, \quad H = \frac{1}{y} \begin{bmatrix} \rho v \\ \rho uv \\ \rho v^2 \\ v(\rho E + P) \end{bmatrix} \qquad (2.2)$$

Here, vector $U$ is the solution vector of conserved variables and vectors $F$ *and* $G$ are the inviscid flux vectors, $H$ is the axisymmetric source term, $\rho$ denotes the density, $u$ and $v$ represent velocity components in the $x$ and $y$ Cartesian directions respectively. We denote the pressure by $P$, the total internal energy per unit mass by $E$, and the total enthalpy per unit mass by $h$. $E$ is related to $h$ through the following relationship as

$$E = h - \frac{P}{\rho} \qquad (2.3)$$

In this work, the ideal gas equation of state is assumed the pressure relating the $E$ as:

$$P = (\gamma - 1)\rho \left( E - \frac{u^2 + v^2}{2} \right) \qquad (2.4)$$

where $\gamma$ is the specific heat ratio.

## 2.1.2 Navier-Stokes Equations

The two-dimensional planar or axisymmetric Navier-Stokes equations for the flow of a viscous, compressible flow fluid may be written in conservative form, Cartesian co-ordinates system [18] as follows:

$$\frac{\partial U}{\partial t} + \frac{\partial F}{\partial x} + \frac{\partial G}{\partial y} + \alpha H = \frac{\partial F_v}{\partial x} + \frac{\partial G_v}{\partial y} + \alpha H_v \qquad (2.5)$$

where vectors $U$, $F$, $G$, $H$ are the same as the Euler relations (2.2), and vectors $F_v$ and $G_v$ denote the viscous fluxes and $H_v$ is the axisymmetric source term expressed in non-dimensional form by

$$F_v = \frac{1}{Re}\begin{bmatrix} 0 \\ \sigma_x \\ \tau_{yx} \\ R_x \end{bmatrix}, G_v = \frac{1}{Re}\begin{bmatrix} 0 \\ \tau_{xy} \\ \sigma_y \\ R_y \end{bmatrix}, H_v = \frac{1}{y\,Re}\begin{bmatrix} 0 \\ \tau_{xy} \\ 2\mu(\,v_y - v/y\,) \\ R_y \end{bmatrix} \qquad (2.6)$$

Assuming a Newtonian fluid, the viscous flux terms can be expressed in usual fashion by

$$\sigma_x = 2\mu u_x - \frac{2}{3}\mu(\,u_x + v_y + \alpha\frac{v}{y}\,),$$

$$\sigma_y = 2\mu v_y - \frac{2}{3}\mu(\,u_x + v_y + \alpha\frac{v}{y}\,),$$

$$\tau_{xy} = \tau_{yx} = \mu(\,u_y + v_x\,), \qquad (2.7)$$

$$R_x = u\sigma_x + v\tau_{xy} - q_x,$$

$$R_y = u\tau_{yx} + v\sigma_y - q_y,$$

where $\sigma$ and $\tau$ are the shear stresses, and $q$ are the heat fluxes. *Re* is the Reynolds number expressed as:

$$Re = \frac{\rho UL}{\mu} \qquad (2.8)$$

For the details of the non-dimensionalisation procedure, see Appendix A.

## 2.2 Numerical Solvers

In this section, the Euler equation (2.1) are considered for an inviscid compressible flow. The conservation form of these equations in one Cartesian space variable is

$$\frac{\partial U}{\partial t} + \frac{\partial F}{\partial x} = 0 \qquad\qquad (2.9)$$

and can be written in integral form over the distance bounded by $x_1$ and $x_2$ as

$$\frac{d}{dt} \int_{x_1}^{x_2} U(x,t)dx = F(x_1,t) - F(x_2,t) \qquad\qquad (2.10)$$

These Euler equations, due to its hyperbolic nature, admit discontinuous solutions (shock waves, contact surfaces). The correct resolution of the discontinuities presents the major hazards while modelling inviscid compressible flow. Many numerical schemes have been reported to solve equations in the form of equation (2.10). Artificial viscosity methods, flux splitting techniques and Godunov's method are the most popular techniques in finite volume methods [17, 44].

The Godunov's methods or reconstruction evolution have been successfully used modelling hypersonic flows. This method has been used throughout this work with the high order extension MUSCL (Monotone Upstream-centred Schemes for Conservation Laws) [46].

In this section, the numerical method will be presented with the approximate Riemann solver and the MUSCL extension [17]. We will discuss the test case which was suggested by Sod [41] to compare the numerical schemes.

## 2.2.1 Godunov's Methods

Let $\rho$ be the density, $m = \rho u$ be the momentum per unit length and $e = \rho E$ be the total energy per unit length. The time is divided into intervals of length $l$ and let $\Delta x$ be the spatial increment. The solution is to be evaluated at time $t^n = nl$ where $n$ is a positive integer at the spatial increments $x_i = \Delta x_i$, $i = 0$, $\pm 1$, $\pm 2$. The vector $U_i^n$ which approximate the cell average can be expressed mathematically as

$$U_i^n = \frac{1}{\Delta x} \int_{x_{i-\frac{1}{2}}}^{x_{i+\frac{1}{2}}} U(x,t^n)\,dx$$

$$\Delta x = \int_{x_{i-\frac{1}{2}}}^{x_{i+\frac{1}{2}}} dx$$

(2.11)

where $i + \frac{1}{2}$ denotes the interface between cell $i$ and $i+1$.

In Godunov's upwind differencing scheme [14] which was presented in 1959, the fluid is described as a sequence of cell-averaged conserved quantities $\rho_i^n$, $m_i^n$, $e_i^n$. The averages $U_i^{n+1} = (\rho_i^{n+1}, m_i^{n+1}, e_i^{n+1})$ at the next time level $t^{n+1} = t^n + l$ can be obtained by averaging over a cell $(\Delta x_{i-\frac{1}{2}}, \Delta x_{i+\frac{1}{2}})$.

With Godunov's scheme, the flow domain is treated as a succession of cells with cell interfaces lying between consecutive grid points. The variation of vector $U$ over these cells can be approximated by averaging into piecewise constant quantities. These piecewise constant quantities are assigned to the grid point representing the cell as showed in Fig. 2-1.

Hence, the integral form of Euler equation (2.10) which can be evaluated by using the numerical flux through a cell over the time increment $\Delta t$ at the next time level $t^{n+1}$ can be written in conservation form as

$$U_i^{n+1} = U_i^n - \frac{\Delta t}{\Delta x}(F_{i+\frac{1}{2}}^n - F_{i-\frac{1}{2}}^n) \qquad (2.12)$$

where $F_{i+\frac{1}{2}}^n$ and $F_{i-\frac{1}{2}}^n$ are the time averaged fluxes through cell interfaces $i + \frac{1}{2}$ and $i - \frac{1}{2}$ respectively.
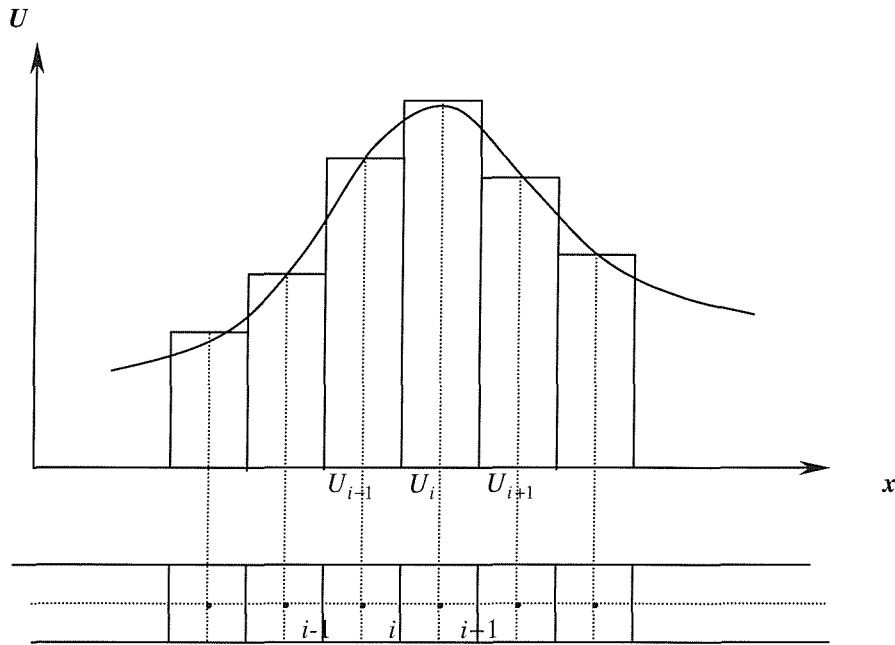


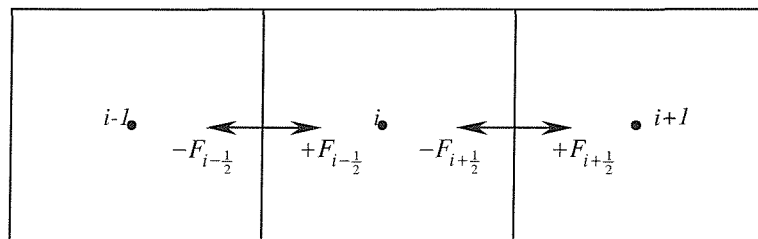Fig. 2-1 Cell averaged representation of conserved variables for Godunov's scheme



Fig. 2-2 Time averaged fluxes through cell interfaces in a 1-D flow domain

It is more efficient to calculate the fluxes to the two cells bounded by each interface rather than to calculate the fluxes to one cell bounded by two interfaces. This is shown in Fig. 2-2.

Let the fluxes in $U_i$ be written in the form through interfaces $i+\frac{1}{2}$ and $i-\frac{1}{2}$ as

$$\delta U_i^{\,L} = +\frac{\Delta t}{\Delta x} F_{i-\frac{1}{2}}^{\,n} \qquad (2.13)$$

$$\delta U_i^{\,R} = -\frac{\Delta t}{\Delta x} F_{i+\frac{1}{2}}^{\,n} \qquad (2.14)$$

The equations (2.13) and (2.14) can be combined to give $U_i$ at the next time as follows:

$$U_i^{n+1} = U_i^{n} + \delta U_i^{\,L} + \delta U_i^{\,R} \qquad (2.15)$$

which updates the equation (2.15).

With Godunov's scheme, the equation (2.15) is completely defined once the fluxes have been specified. Godunov's scheme uses the solution of the local Riemann problem with data ($U_i^{n}, U_{i+1}^{n}$) to define the numerical flux $F_{i+\frac{1}{2}}^{\,n}$.

## 2.2.2 The Riemann Problem

The Riemann problem for equation (2.9) is the initial value problem in the domain $-\infty < x < \infty$, $t > 0$ with initial data

$$U(x,0) = \begin{cases} U_L, & x < 0, \\ U_R, & x > 0, \end{cases} \qquad (2.16)$$

as illustrated in Fig. 2-3.

The Riemann problem with two intermediate states $U_L^*$ and $U_R^*$ separated by the middle wave $V$ was defined as

$$U(\frac{x}{t}, U_L, U_R) = \begin{cases} U_L & if \quad a_L > \dfrac{x}{t} \\[2ex] U_L^* & if \quad a_L < \dfrac{x}{t} < V \\[2ex] U_R^* & if \quad V < \dfrac{x}{t} < a_R \\[2ex] U_R & if \quad a_R < \dfrac{x}{t} \end{cases} \tag{2.17}$$
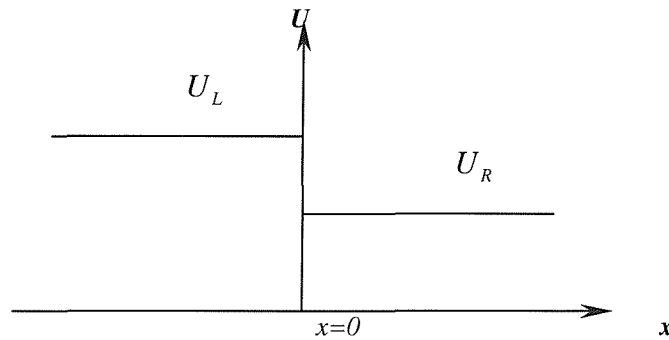


Fig. 2-3 Initial state values of the Riemann problem defined at time $t=0$

The structure of the solution of the Riemann problem is depicted in Fig. 2-4. There are three waves. The middle wave is always a contact discontinuity. The left and right waves, which due to their character are called non-linear waves, can be either shock waves or rarefaction waves depending on the states $U_L$ and $U_R$ [6, 15]. Hence, there are four possible wave patterns. Contacts and shocks are discontinuities, rarefaction waves are continuous solutions.

The region bounded by the two non-linear waves is defined as the star * region. The * region has constant pressure $p^*$ and constant normal velocity $u^*$. The other

variables that appear in vector $U$ have differing left and right states of the contact discontinuity $U_L^*$ and $U_R^*$. Finding exact solutions of the Riemann problem is computationally expensive. For this reason approximate Riemann solvers were developed.

To modify the exact solution of the Riemann problem, a number of approximate Riemann solvers have been developed following ideas of some researchers, e.g.: the HLL (Harten, Lax and van Leer) approximate Riemann solver [15], the HLLE (Harten, Lax, van Leer and E stands for Einfedlt) approximate Riemann solver and the HLLC (Harten, Lax, van Leer and C stands for Contact) approximate Riemann solver [43]. The choice of approximate Riemann solver is heavily dependent on the type and conditions of flow to be simulated. An example of this will be discussed later in a test case of shock tube problems. The HLLC solver is the most accurate, can mimic the exact Riemann problem and will be presented here.
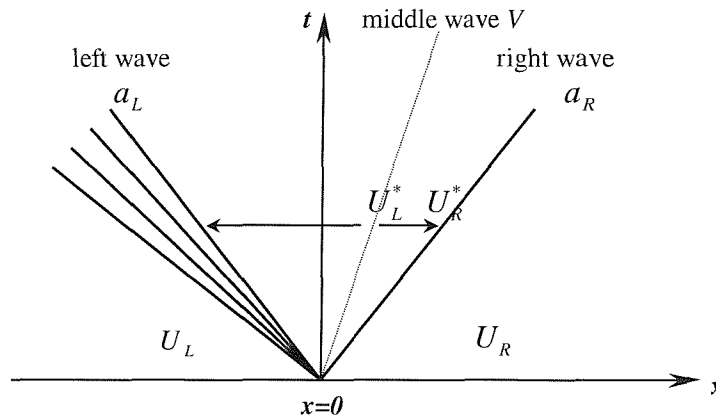


Fig. 2-4 The time dependant solution of the Riemann problem in the *x-t* plane. The three waves present define four piece-wise constant states $U_L$, $U_R$, $U_L^*$ and $U_R^*$

## 2.2.3 The HLLC Approximate Riemann Solver

This improved version HLLC solver was presented by Toro et al. [43]. This solver is based on the HLL solver put forward by Harten, et al. [15]. It accounts for the

contact discontinuity in the physics of the problem by incorporating the contact surface into the wave pattern.

In Fig. 2-5, we consider two averaged intermediate states, $U_L^*$, $U_R^*$, separated by the contact wave, whose speed is denoted by $S_M$. The two-state approximate Riemann solution was defined by Toro et al. [43] as

$$U_{HLLC} = \begin{cases} U_L & if \ S_L > 0 \\ U_L^* & if \ S_L \leq 0 < S_M \\ U_R^* & if \ S_M \leq 0 \leq S_R \\ U_R & if \ S_R < 0 \end{cases} \tag{2.18}$$

The corresponding interface flux, denoted $F_{HLLC}$, is defined as

$$F_{HLLC} = \begin{cases} F_L & if \ S_L > 0 \\ F_L^* & if \ S_L \leq 0 < S_M \\ F_R^* & if \ S_M \leq 0 \leq S_R \\ F_R & if \ S_R < 0 \end{cases} \tag{2.19}$$

Integrating over the rectangle *ABCD* and using the criterion which is given by HLLC approximate Solver [43] shown as

$$U^*(S_R - S_L) = U_R^*(S_R - S_M) + U_L^*(S_M - S_L), \tag{2.20}$$

which simply states that the weighted average of $U_L^*$ and $U_R^*$ must give the mean value of the exact solution, $U^*$, between the two acoustic waves.

Considering various ways of computing the $U_L^*$ and $U_R^*$ states from estimates of the flux across the contact line suggested by Harten et al. [15] and the simplest approach for computing these star states suggested by Toro et al. [43], we can

observe that the particle velocity may be assumed constant between the acoustic waves if we ignore the influence factor of expansion fans.
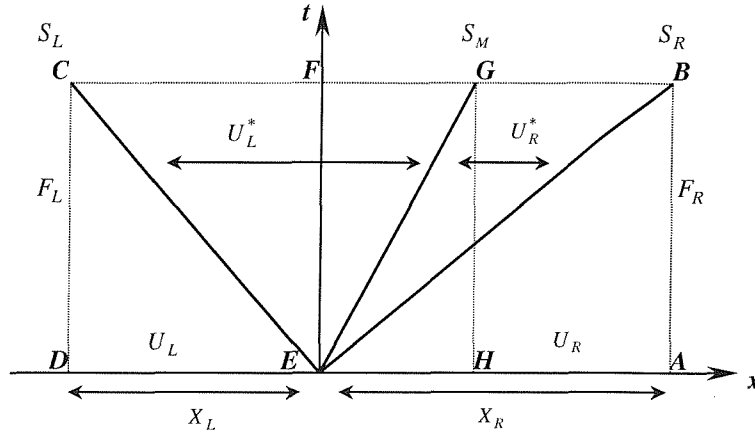


Fig. 2-5 Simplified Riemann fan with two intermediate states

Applying the Rankine-Hugoniot conditions across the $S_L$ wave in the quadrilateral *CDEF* gives

$$F_L^* = F_L + S_L(U_L^* - U_L)$$ (2.21)

Similarly, the $S_R$ wave in the rectangle *ABGH* gives

$$F_R^* = F_R + S_R(U_R^* - U_R)$$ (2.22)

Equations (2.21) and (2.22) can be written as

$$S_L U_L^* - F_L^* = S_L U_L - F_L$$ (2.23)

$$S_R U_R^* - F_R^* = S_R U_R - F_R$$ (2.24)

For the three-dimensional Euler equations with states $U_L$, $U_R$ separated by an interface with unit normal vector $\vec{n}$, equation (2.23) can be expressed in full as

$$S_L \begin{bmatrix} \rho_L^* \\ \rho_L^* u_L^* \\ \rho_L^* \upsilon_L^* \\ \rho_L^* \omega_L^* \\ \rho_L^* E_L^* \end{bmatrix} - \begin{bmatrix} \rho_L^* q_L^* \\ \rho_L^* u_L^* q_L^* + P_L^* n_x \\ \rho_L^* \upsilon_L^* q_L^* + P_L^* n_y \\ \rho_L^* \omega_L^* q_L^* + P_L^* n_z \\ q_L^* (\rho_L^* E_L^* + P_L^*) \end{bmatrix} = S_L \begin{bmatrix} \rho_L \\ \rho_L u_L \\ \rho_L \upsilon_L \\ \rho_L \omega_L \\ \rho_L E_L \end{bmatrix} - \begin{bmatrix} \rho_L q_L \\ \rho_L u_L q_L + P_L n_x \\ \rho_L \upsilon_L q_L + P_L n_y \\ \rho_L \omega_L q_L + P_L n_z \\ q_L (\rho_L E_L + P_L) \end{bmatrix} \qquad (2.25)$$

where $q = un_x + \upsilon n_y + \omega n_z$. For one-dimensional problem, it can be expressed as $q = u$ using $n_x = 1$, $n_y = 0$ and $n_z = 0$.

For finding values of the vectors $U_L^*$ and $U_R^*$, Toro et al. [43] assumed that

$$S_M = q_L^* = q_R^* = q^c \qquad (2.26)$$

where $q^c$ was taken as some estimate of the contact velocity. However, Batten et al. [4] made the assumption that

$$S_M = q_L^* = q_R^* = q^* \qquad (2.27)$$

where $q^*$ is the average directed velocity between the two acoustic waves. Now, assuming that the wave speed of the contact discontinuity is $u^* = S_M$. The expression for $S_M$ within the HLLC approximate solver to $U^*$ can be given by

$$S_M = \frac{\rho_R q_R (S_R - q_R) - \rho_L q_L (S_L - q_L) + P_L - P_R}{\rho_R (S_R - q_R) - \rho_L (S_L - q_L)} \qquad (2.28)$$

Then, the first equation can be given by

$$\rho_L^* = \rho_L \frac{(S_L - q_L)}{(S_L - S_M)} \qquad (2.29)$$

The second equation can be given by

$$P_L^* = \rho_L(q_L - S_L)(q_L - S_M) + P_L \tag{2.30}$$

The final equation gives

$$\rho_L^* E_L^* = \frac{\rho_L E_L(S_L - q_L) - \rho_L q_L + P_L^* S_M}{S_L - S_M} \tag{2.31}$$

As the pressure in the star region is constant, it is possible to construct the vector of conserved averaged variables. Then the fluxes can be calculated using equation (2.23). For the case where $S_L > 0$, it is the right supersonic case. Similarly, for the case where $S_R < 0$, it is the left supersonic case. In the star region, for the two cases where $S_L \leq 0 < S_M$ and $S_M \leq 0 \leq S_R$, they are both the subsonic cases. These equations can be solved exactly in the same way just switching L for R subscripts. The solution of the relevant fluxes is available once an accurate estimation of wave speeds $S_L$ and $S_R$ is obtained.

### 2.2.4 Roe Average state

Many Riemann solvers make use of the eigenvalues and eigenvectors of the Jacobian matrix $A = \dfrac{\partial F}{\partial U}$. For a general gas, the Jacobian matrix $\dfrac{\partial F}{\partial U}$ of the Euler equation can be written as

$$A = \begin{bmatrix} 0 & 1 & 0 \\ \dfrac{(\gamma-3)}{2}u^2 & (3-\gamma)u & (\gamma-1) \\ (\gamma-1)u^3 - u\gamma E & \dfrac{3}{2}(1-\gamma)u^2 + \gamma E & \gamma u \end{bmatrix} \tag{2.32}$$

The three eigenvalues of A are

$$
\begin{aligned}
\lambda_1 &= u + c \\
\lambda_2 &= u - c \\
\lambda_3 &= u
\end{aligned}
$$

(2.33)

where $c$ is the speed of sound.

In this one-dimensional shock tube problem, these eigenvalues represent the speed of the right, left extreme waves and the velocity of the fluid respectfully. However, a discontinuity can be given effectively in the flow with the left and right hand initial states each producing a Jacobian matrix $A$ at the interface of the two cells. Then, the right and left states of the interface can be defined as two Jacobian matrices, $A_R$ and $A_L$. So it is required to form an average matrix $\tilde{A}$, so as not to violate the laws of conservation. For formulating an average matrix, Roe [37] and Yee [51] showed this to be true by constructing an average state $\tilde{U}(U_L, U_R)$ using the following relations

$$
\begin{aligned}
\tilde{\rho} &= \frac{\rho_L + \alpha \rho_R}{1 + \alpha} \\
\tilde{u} &= \frac{u_L + \alpha u_R}{1 + \alpha} \\
\tilde{H} &= \frac{H_L + \alpha H_R}{1 + \alpha} \\
\tilde{c}^2 &= (\gamma - 1)\left[ \tilde{H} - \frac{\tilde{u}^2}{2} \right]
\end{aligned}
$$

(2.34)

where $\alpha = \sqrt{\dfrac{\rho_R}{\rho_L}}$.

For finding the linearised estimates of the two waves for the HLL approximate Riemann solver, Roe defined the eigenvalues $\lambda_1$ and $\lambda_2$ as

$$S_L^{Roe} = \tilde{u} - \tilde{c}$$
$$S_R^{Roe} = \tilde{u} + \tilde{c} \qquad\qquad (2.35)$$

Then the new lower and upper limits of the acoustic wave speed estimates can be expressed as

$$S_L = min(\, 0, S_L^{Roe}, u - c\,)$$
$$S_R = max(\, 0, S_R^{Roe}, u + c\,) \qquad\qquad (2.36)$$

No matter which approximate Riemann solver we use, the accuracy of the solver is fully dependant on the choice of these wave speed estimates [43]. Hence, another method of implementing the Riemann solver was presented by Einfeldt (known as HLLE) [10] to improve the results obtained. Einfeldt suggested an improvement on the wave speed estimates regarding the numerical dissipation near rarefaction waves, and chose the wave speed estimates as

$$S_L = min(\, 0, S_L^{Roe}, u_L - \beta c_L\,)$$
$$S_R = max(\, 0, S_R^{Roe}, u_R + \beta c_R\,) \qquad\qquad (2.37)$$

where $\beta = \sqrt{\dfrac{\gamma - 1}{2\gamma}}$. However, according to Toro [43], this method can lead to problems with the undesirable feature of smearing of contact surfaces for certain applications, and so in this work, Equation (2.36) has been used.

## 2.2.5 MUSCL Schemes

The procedure to be followed here is based on an extension of the Godunov type schemes. The projection stage, whereby the solution is projected in each cell $(i - \tfrac{1}{2}, i + \tfrac{1}{2})$ on piecewise constant states, is the cause of the low accuracy of the Godunov schemes. This step is completely decoupled from the physical stage

where the Riemann problems are solved at the interfaces of the cells. Therefore, it is possible to modify the projection process without modifying the Riemann solver, in order to generate higher spatial approximations. The state variables at the interfaces can be obtained from an extrapolation of the neighbouring cells. This method for the generation of second-order upwind schemes via variable extrapolation can be referred to in the literature as the MUSCL scheme (Monotone Upstream-centred Schemes for Conservation Laws) which was developed by van Leer [46].

Let us consider the general local representation, valid within cell $i$, at a given instant, see Fig. 2-6:

$$U(x) = U_i + \frac{1}{\Delta x}(x - x_i)\delta_i U + \frac{3\kappa}{2\Delta x^2}\left[(x - x_i)^2 - \frac{\Delta x^2}{12}\right]\delta_i^2 U \qquad (2.38)$$

where $x_{i-\frac{1}{2}} < x < x_{i+\frac{1}{2}}$ and $U_i$ is the average value, defined by

$$U_i = \frac{1}{\Delta x}\int_{i-\frac{1}{2}}^{i+\frac{1}{2}} U(x)dx \qquad (2.39)$$
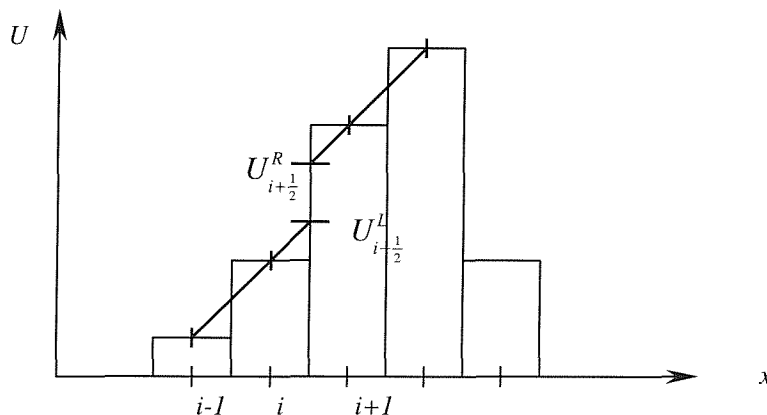


Fig. 2-6 Linear extrapolation for a more accurate prediction of interface values

and $\delta_i U, \delta_i^2 U$ are estimations of the first and second order differences within cell
$i$. The derivatives with cell $i$ must be computed in order to preserve the monotone
of the solution, clipping the extremes to avoid oscillations near discontinuities.
The MUSCL schemes are first order accurate near discontinuities.

Actually, the resolution of the Riemann problem or the numerical flux estimation
requires only the values at the cell boundaries. For the second order accuracy,
setting $x = x_i \pm \frac{\Delta x}{2}$ within cell $i$ expresses the linear extrapolation of $U$ as

$$U^L_{i+\frac{1}{2}} = U_i + \frac{1}{2}\Delta x \frac{\partial U}{\partial x}\bigg|_{lim}$$
$$U^R_{i-\frac{1}{2}} = U_i - \frac{1}{2}\Delta x \frac{\partial U}{\partial x}\bigg|_{lim}$$

(2.40)

$\frac{\partial U}{\partial x}\bigg|_{lim}$ is computed through a function of neighbour cells in a slope limiter process

as Amaratunga [1].

if$(U_{i+1} - U_i)(U_i - U_{i-1}) \leq 0$

$$\frac{\partial U}{\partial x}\bigg|_{lim} = 0$$

(2.41)

else

$$\frac{\partial U}{\partial x}\bigg|_{lim} = min\left\{2k\left|\frac{U_{i+1}-U_i}{\Delta x}\right|, \frac{1}{2}\left|\frac{U_{i+1}-U_{i-1}}{2\Delta x}\right|, 2k\left|\frac{U_i-U_{i-1}}{\Delta x}\right|\right\}$$
$$sgn\left(\frac{U_{i+1}-U_{i-1}}{2\Delta x}\right)$$

(2.42)

Here, $k$ is defined as a parameter to switch the MUSCL step on and off. If $k=1$, the
MUSCL step is fully on and if $k=0$, then the MUSCL step is off. This parameter $k$

allows us to control the degree of dissipation of the scheme. If $k$ increases, the formal accuracy also increases as we add numerical dissipation through the limiter. However, near boundary layers this numerical dissipation can mask natural diffusion related to viscosity, creating convergence problems. In this shock tube problem test $k=0.8$ has been used.

Although the MUSCL implementation was seen to work well with a simple test case (Sod's problem, see Section 4.1), when applied to a more realistic shock tube or expansion tube configuration, the MUSCL scheme provoked an oscillatory behaviour with results. The problem appears to be worse at higher diaphragm pressure ratios, where the wave propagations are stronger. Therefore, in these cases only non-MUSCL results are implemented, restricting the results to first order accuracy in space.

## 2.3 Inviscid Boundary Conditions

In general, specification of the boundary conditions and their numerical implementation when solving the Euler equations is an important part of the overall algorithm construction. For satisfying the conservation of mass, at a solid wall boundary, the normal velocity must be set to zero (shown in Fig. 2-7), this implies that no mass or other flux can penetrate the solid wall. Hence, the physical condition imposed is $u_n = 0$. The other variables at the solid wall, velocity and pressure, can be calculated using a symmetry condition.

### 2.3.1 Solid Walls

In terms of parameters, for two-dimensional flow problems, zero wall gradients of density, energy and tangential velocity, and a zero normal velocity can be imposed at a solid wall in the conserved vector components as follows:

$$
\begin{aligned}
(\rho)_{ghost} &= (\rho)_{fluid} \\
(\rho u_t)_{ghost} &= (\rho u_t)_{fluid} \\
(\rho u_n)_{ghost} &= -(\rho u_n)_{fluid} \\
(\rho E)_{ghost} &= (\rho E)_{fluid}
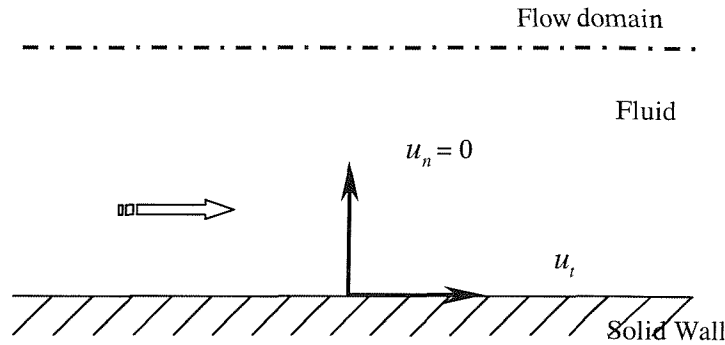\end{aligned}
\tag{2.43}
$$



Fig. 7: A zero normal velocity at a solid wall.

## 2.4 Time Stepping and Stability

The time step, $\Delta t$, is obtained from the inviscid explicit solver. In order to maintain stability, it is necessary to limit the time step. For the first time step in the solution, $\Delta t$ is set very small, and then later time steps are computed by using the Courant condition (also known as Courant-Friedrichs-Lewyor (CFL) condition) with a Courant number (CFL) of 0.7 and the wavespeeds $S$ obtained from the Riemann solvers as follows:

$$
\Delta t = CFL \frac{\Delta x}{S_{max}}
\tag{2.44}
$$

## 2.5 Multi-Dimensional Flow

In general though, most flow fields can be categorised into either two-dimensional, axisymmetric or three-dimensional flow problems. They are all

defined as multi-dimensional flows. As we know, these multi-dimensional flows always involve many problems; i.e., the complex shape problems and surface catalytic effect problems.

In general, numerical solution of multidimensional fluid problem is more complex than its one-dimensional counterpart. The operator splitting method is a simple technique to reduce the multi-dimensional problem to a series of one-dimensional problems. In this section an operator splitting methodology which can simply calculate multi-dimensional flows is considered [5, 24, 25, 42].

### 2.4.1 Dimensional Operator Splitting

This method is similar to that used in the one-dimensional flow. For two-dimensional problems, the whole domain is divided into rectangular cells. Four cell boundaries can be considered with Godunov's method as shown in Fig. 2-8.
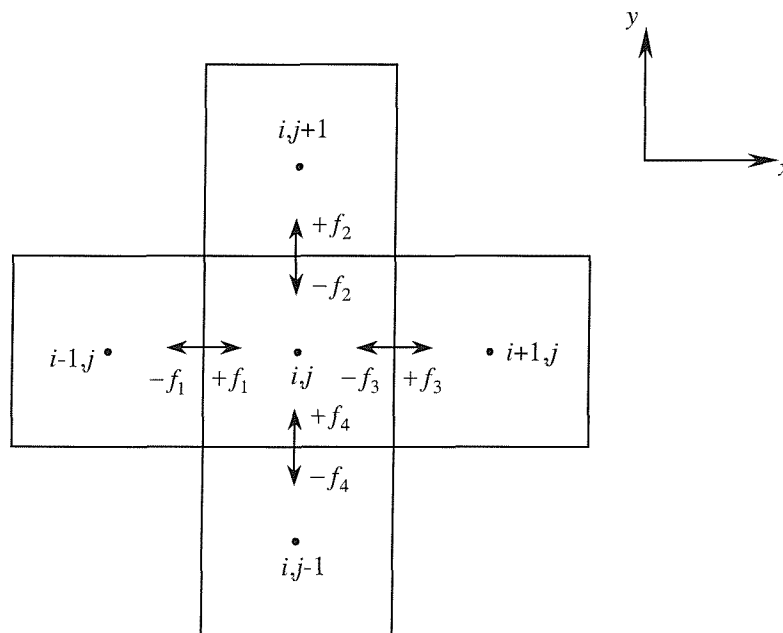


Fig. 2-8 An arbitrary cell $i,j$ for two-dimensional flow

The governing equations are given as

$$\frac{\partial U}{\partial t} + \frac{\partial F}{\partial x} + \frac{\partial G}{\partial y} = 0 \tag{2.45}$$

where

$$U = \begin{bmatrix} \rho \\ \rho u \\ \rho v \\ \rho e \end{bmatrix}, F = \begin{bmatrix} \rho u \\ \rho u^2 + p \\ \rho uv \\ u(\rho e + p) \end{bmatrix}, G = \begin{bmatrix} \rho v \\ \rho vu \\ \rho v^2 + p \\ v(\rho e + p) \end{bmatrix} \tag{2.46}$$

and in numerical form showed as

$$U_{i,j}^{n+1} = U_{i,j}^{n} - \frac{\Delta t}{\Delta x}\left(F_{i+\frac{1}{2}}^{n} - F_{i-\frac{1}{2}}^{n}\right) - \frac{\Delta t}{\Delta y}\left(G_{j+\frac{1}{2}}^{n} - G_{j-\frac{1}{2}}^{n}\right) \tag{2.47}$$

Then the flux balance at cell *i,j* can be expressed in conservation form as

$$U_{i,j}^{n+1} = U_{i,j}^{n} + \frac{\Delta t}{A_{i,j}} \sum_{k=1}^{4} C_k f_k \tag{2.48}$$

where *i,j* refers to an arbitrary grid point in the *x,y* plane and $f_k$ is the time averaged flux through an interface of the length $C_k$.

Using an operator splitting this solution procedure can be split up into two steps which are considered separately. The first step is the flow in the x-wise direction and gives the fluxes $F_{i+\frac{1}{2}}^{n}$ and $F_{i-\frac{1}{2}}^{n}$. Simultaneously, the second step is the flow in the y-wise direction and gives the fluxes $G_{i+\frac{1}{2}}^{n}$ and $G_{i-\frac{1}{2}}^{n}$. Here, equation (2.43) can be split into directional operators as follows:

*Chapter 2 Numerical Methods*

$$\frac{\partial U}{\partial t} + \frac{\partial F}{\partial x} = 0$$
$$\frac{\partial U}{\partial t} + \frac{\partial G}{\partial y} = 0$$

(2.49)

Therefore, it is not necessary to consider a new multi-dimensional solver. The standard HLLC solver is utilized twice instead.

## 2.4.2  Extension to Axisymmetric Flow

The algorithm for axisymmetric flow is derived from the two-dimensional version with a number of changes to suit the geometry. This geometry has boundary conditions similar to two-dimensional flow. The volume of each cell varies with radius, as does the area of the cell surface. The simulations for axisymmetric flow are set up the lower edge of the domain to be zero radius, and can be allowed for an offset radius as in an annular domain shown in Fig. 2-9. The grid points in the computing domain are uniformly spaced on $x$-axis and $r$-axis for two-dimensional axisymmetric viscous simulations.
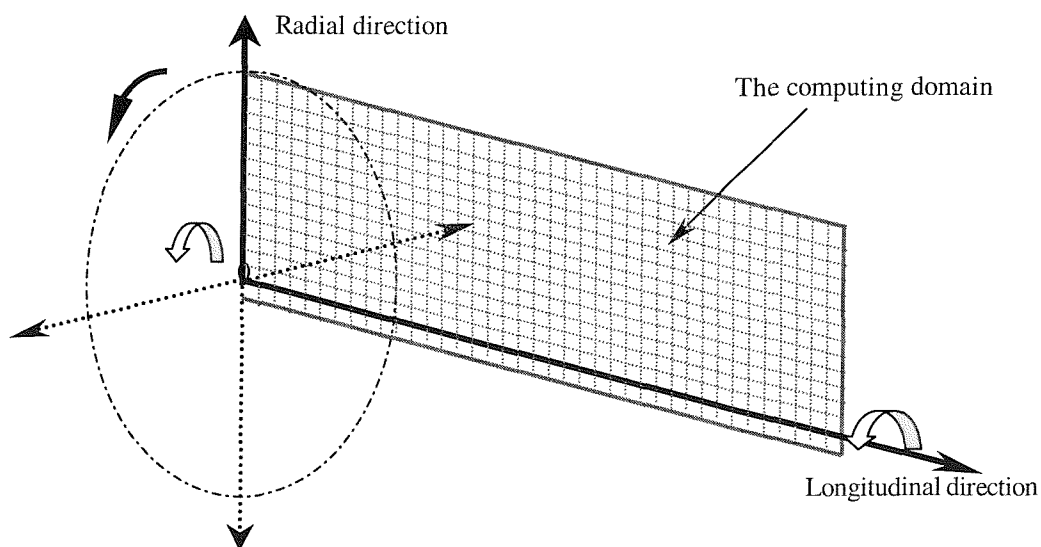


Fig. 2-9 The computing domain in annular space (Not to scale)

## 2.4.3 Numerical Treatments

In the axisymmetric flow case, the boundary conditions can also be treated as in the two-dimensional flow case. However, it may be made more complex when we consider moving the MUSCL into two-dimensional or axisymmetric flow.

# Chapter 3

# Viscous Compressible Flow

In this section, the effects of viscosity in the solution of the governing equations are considered. The Navier-Stokes equations required for the two-dimensional axisymmetric flow problem can be given in conservative form, in cylindrical co-ordinates (x,r) by [32]

$$\frac{\partial \overline{U}}{\partial t} + \frac{\partial \overline{F}}{\partial x} + \frac{\partial \overline{G}}{\partial r} = \frac{\partial \overline{F_v}}{\partial x} + \frac{\partial \overline{G_v}}{\partial r} + A \tag{3.1}$$

where $\overline{U}$ is the vector of conserved variables and $\overline{F}$ and $\overline{G}$ are the inviscid flux vectors in the $x$ and $r$ Cartesian directions respectively, $\overline{F_v}$ and $\overline{G_v}$ are the corresponding viscous fluxes. These fluxes can been given by the relations shown in Equation (2.7) in cylindrical co-ordinates (x,r). $A$ is the additional terms for the axisymmetric flow problem and can be given by

$$A = \frac{1}{r}\begin{pmatrix} 0 \\ 0 \\ P - \tau_{\theta\theta} \\ 0 \end{pmatrix} \tag{3.2}$$

The shear stress of $A$ are given as

$$\tau_{\theta\theta} = -\frac{1}{Re}\left[\frac{2}{3}\mu\left(\frac{\partial u}{\partial x}+\frac{\partial v}{\partial r}-2\frac{v}{r}\right)\right] \qquad (3.3)$$

## 3.1 Transport Properties

The transport properties are important for viscous flow field simulations, particularly for the estimation of the wall heat flux (see 4.2.4.1). These properties include specific heat capacities, viscosity and thermal conductivity. The specific heat capacities are assumed to be these for an ideal gas, i.e.

$$c_v = \frac{R}{\gamma - 1} \qquad (3.4)$$

$$c_p = \frac{\gamma}{\gamma - 1}R \qquad (3.5)$$

where R is the specific gas constant. It is assumed that for the range of conditions considered here with Argon ($R = 208\ J/kgK$, $\gamma = 1.667$) as the test gas, $c_v$ and $c_p$ are constant. The viscosity and thermal conductivity are, however, evaluated as function of temperature.

## 3.1.1 Temperature and Heat Flux

The equation of temperature, *T,* for an ideal gas can be expressed as

$$T = \frac{1}{c_v}\left(E - \frac{u^2 + v^2}{2}\right) \qquad (3.6)$$

where $c_v$ is the specific heat at constant volume. The equation of heat flux, *q*, can be expressed following Fourier's heat conduction law as

$$q = -\lambda\nabla T \qquad (3.7)$$

## 3.1.2 Viscosity

With Sutherland's law, a reasonable estimate for the viscosity of a fluid can be given as

$$\mu = \mu_\infty \left(\frac{T}{T_\infty}\right)^{\frac{3}{2}} \left(\frac{T_\infty + 110}{T + 110}\right) \tag{3.8}$$

where $\mu_\infty$ and $T_\infty$ are free stream viscosity and free stream temperature respectively.

## 3.1.3 Thermal Conductivity

Thermal conductivity is proportional to the viscosity through Prandlt number, *Pr,* by

$$\lambda = \frac{\mu c_p}{Pr} \tag{3.9}$$

where $c_p$ is the specific heat at constant pressure. In the calculations of perfect gas, $c_p$ is assumed to be constant, and $Pr$ is suggested to be a constant. $Pr$ is 0.667 for Argon [47].

## 3.2 Implicit Viscous Solver

The viscous solver chosen to solve the viscous flux in this case was based on an implicit scheme put forward by Batten et al. [3]. In an operator splitting method like this, where separate diffusive and convective solvers are used, it may be found

that the stable time step required by the viscous solver is much smaller than that required by the inviscid solver. Implicit solvers have not such limitations and can use larger time steps. Due to the operator splitting approach, it is possible to use an explicit solver in the inviscid part and an explicit solver in the viscous contribution.

The diffusion split PDE's can be given by the equation (3.1) reduced to

$$\frac{\partial \overline{U}}{\partial t} = \frac{\partial \overline{F}_v}{\partial x} + \frac{\partial \overline{G}_v}{\partial r} \qquad (3.10)$$

Dimensional splitting gives

$$\frac{\partial \overline{U}}{\partial t} = \frac{\partial \overline{F}_v}{\partial x} \qquad (3.11)$$

$$\frac{\partial \overline{U}}{\partial t} = \frac{\partial \overline{G}_v}{\partial r} \qquad (3.12)$$

### 3.2.1 Linearisation in Time

With the implicit backward Euler scheme, the change in the vector of conserved variables due to the viscous effects can be given by

$$\frac{d\overline{U}}{dt} = \frac{\left( \left( \overline{F}_v \right)_{i+\frac{1}{2}} - \left( \overline{F}_v \right)_{i-\frac{1}{2}} \right)}{\Delta x} \qquad (3.13)$$

Then the backward Euler scheme can be written as

$$\delta \overline{U}_i = \Delta t \, \overline{R}_i^{n+1} \qquad (3.14)$$

$$\delta \overline{U} = \overline{U}_i^{n+1} - \overline{U}_i^{n} \qquad (3.15)$$

where

$$\overline{R}_i^{n+1} = \frac{\left(\left(\overline{F}_v\right)_{i+\frac{1}{2}} - \left(\overline{F}_v\right)_{i-\frac{1}{2}}\right)^{n+1}}{\Delta x} \tag{3.16}$$

Linearising the terms in time gives the following system of equations

$$\delta \overline{U} = \Delta t \left( \overline{R}^n + \left( \frac{\delta \overline{R}}{\delta \overline{U}} \right)^n \delta \overline{U} \right) \tag{3.17}$$

where

$$\overline{R}^{n+1} = \overline{R}^n + \frac{\delta \overline{R}}{\delta U} \delta \overline{U} \tag{3.18}$$

Then this is solved in the $\delta$ form as

$$\left[ I - \Delta t \left( \frac{\delta \overline{R}}{\delta \overline{U}} \right)^n \right] \delta \overline{U} = \Delta t \overline{R}^n \tag{3.19}$$

And $I$ is an identity matrix and $\dfrac{\delta \overline{R}}{\delta \overline{U}}$ is a viscous flux Jacobian matrix. This formulation could be solved implicitly for $\delta \overline{U}$ which $U$ is updated by

$$U_i^{n+1} = U_i^n + J_i \delta \overline{U}_i \tag{3.20}$$

With this solver, each of the viscous fluxes is considered separately in the two-dimensional viscous code. The calculations of this solver can be expressed as

$$A \delta \overline{U}_{i-1} + (1 - B) \delta \overline{U}_i + C \delta \overline{U}_{i+1} = \Delta t \overline{R}_i^n + D \tag{3.21}$$

where the values of $A$, $B$, $C$ and $D$ vary with each equation.

The values of A, B and C can be entered into a block tridiagonal matrix to give the following system of the equations. This shows that a simple LU decomposition can be used to invert the tridiagonal matrix solving for the $\delta\overline{U}$ terms and update the vector of conserved variables.

$$\begin{pmatrix} 1-B_1 & C_1 & & & \\ A_2 & 1-B_2 & C_2 & & \\ & A_3 & 1-B_3 & C_3 & \\ & & \ddots & \ddots & \ddots \\ & & & & \end{pmatrix} \begin{pmatrix} \delta\overline{U}_1 \\ \delta\overline{U}_2 \\ \delta\overline{U}_3 \\ \delta\overline{U}_4 \\ \vdots \end{pmatrix} = \begin{pmatrix} \Delta t\overline{R}_1 + D_1 \\ \Delta t\overline{R}_2 + D_2 \\ \Delta t\overline{R}_3 + D_3 \\ \Delta t\overline{R}_4 + D_4 \\ \vdots \end{pmatrix} \qquad (3.22)$$

## 3.3 Viscous Boundary Conditions

A set of boundary and initial conditions for the Navier-Stokes equations can be defined. However, physical experience has to be used to determine the nature of the boundary conditions to impose along solid wall boundaries.

### 3.3.1 Adiabatic Wall

Assuming $r$ to be the direction normal to the wall, the boundary conditions for an adiabatic wall can be defined as:

$$\left( \frac{\partial T}{\partial r} \right)_w = 0 \qquad (3.23)$$

The boundary condition above is the temperature gradient, which namely a specified zero gradient at the wall, referred to the zero heat transfer through an adiabatic wall. The no slip boundary condition for the fluid particles at the wall is defined as:

$$u_{wall} = 0$$
$$v_{wall} = 0$$

(3.24)

In two-dimensional axisymmetric flow shown in Fig. 3-1, using the subscript $w$ and N-1 for the quantities referred to the ghost cell for the wall and the last inner cell, respectively. Then, the boundary conditions can be expressed as:

$$T_w = T_{N-1}$$
$$u_w = -u_{N-1}$$
$$v_w = -v_{N-1}$$

(3.25)



Fig. 3-1 Scheme of the wall showing the ghost and the inner cells

### 3.3.2 Isothermal Wall

For an isothermal wall, the temperature remains constant in the wall and the boundary condition is:

$$(T)_{wall} = T_{wall}$$

(3.26)

which is the well known Dirichlet condition, and is used to define an isothermal wall which can be given by second order extrapolations:

$$T_0 = 2T_w - T_1 \qquad\qquad (3.27)$$

Hence, the boundary conditions for an isothermal wall can be given by:

$$
\begin{aligned}
T_w &= 2T_{wall} - T_{N-1} \\
u_w &= -u_{N-1} \\
v_w &= -v_{N-1}
\end{aligned}
\qquad\qquad (3.28)
$$

### 3.3.3 Centre Line

For two-dimensional axisymmetric flow simulations, the symmetry conditions can be given by:

$$\frac{\partial T}{\partial r} = 0 \qquad\qquad (3.29)$$

$$\frac{\partial u}{\partial r} = 0 \qquad\qquad (3.30)$$

Using the subscript $g$ and 1 for the quantities referred to the ghost cell and fluid cell (the first inner cell) the boundary conditions can be expressed as:

$$
\begin{aligned}
T_g &= T_1 \\
u_g &= u_1 \\
v_g &= -v_1
\end{aligned}
\qquad\qquad (3.31)
$$

# Chapter 4

# Results

## 4.1 Sod's Shock Tube Problem

### 4.1.1 Physical Description

In this section the standard simple test case of the shock tube problem suggested by Sod [41] is utilized to verify the inviscid numerical scheme. In its simplest form, the shock tube consists of a long tube of constant area divided into two sections by a diaphragm. The latter is typically made from a thin sheet of metal which often has grooves cut into it to ensure that it can easily and clearly broken. The tube contains a high pressure driver gas on one side of the diaphragm and a low pressure driven gas on the other side of the diaphragm, as shown in Fig. 4-1. When the diaphragm is broken, a shock wave propagates into the low pressure section and an expansion wave propagates into the high pressure section as illustrated in Fig. 4-2. The driver/driven gas interface, known as the contact surface, lies between the shock wave and the expansion wave. Between the shock wave and the contact surface a uniform region of high velocity and temperature is generated that can be used for many different types of experimental studies.

The flow condition generated in a shock tube can be determined analytically by noting that the velocity and pressure behind the shock wave must be equal to the velocity and pressure behind the expansion wave as indicated in Fig. 4-3 [2]. The shock wave increases the temperature of the driven gas whereas the expansion wave decreases the temperature of the driver gas. The situation illustrated in Fig.

4-3 (b) is where the driver gas temperature is equal to the driven gas temperature ($T_4 = T_1$, for example).

Primary diaphragm

| High Pressure | Low Pressure |

$X = x_0$
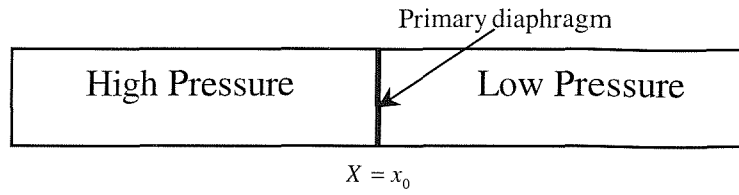
Fig. 4-1 Arrangement of the shock tube

Initial position of primary diaphragm

Expansion Wave          Contact          Shock Wave
                        Surface
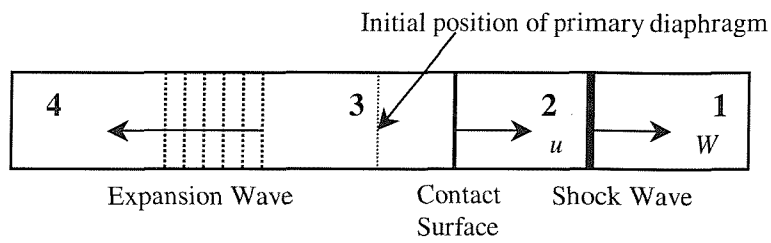
Fig.4-2 Wave generated in the shock tube following
rupture of primary diaphragm
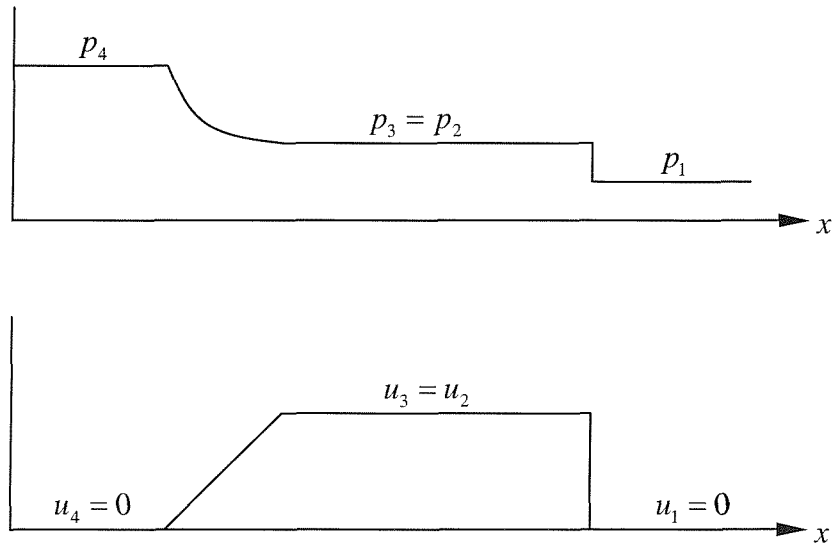
Fig.4-3 (a) Schematic diagram of flow in a shock tube
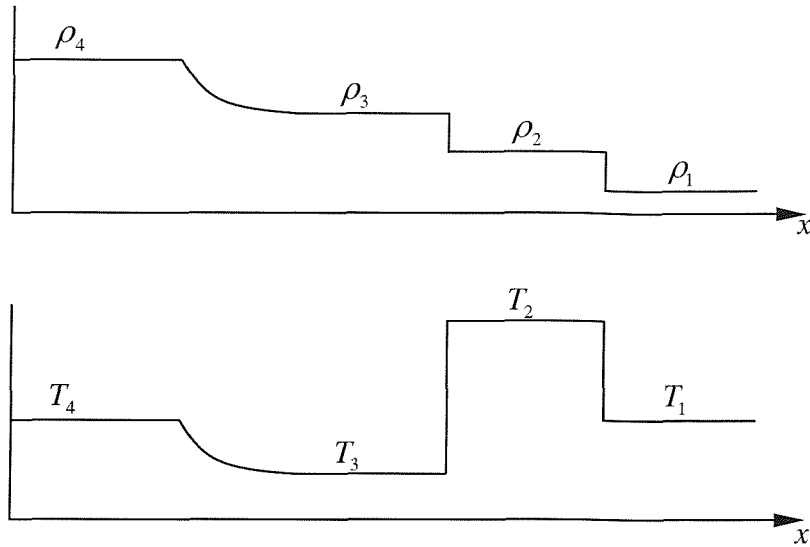
Fig.4-3 (b) Schematic of flow in a shock tube

## 4.1.2 1-D simulation without MUSCL solution

The one-dimensional exact analytical solution consists of a left rarefaction, a contact surface and a right shock. It is used to validate the accuracy of the one-dimensional numerical simulation using the HLLC solver. The initial conditions can be given by

$$U(x,0) = \begin{cases} U_L(\rho_L, u_L, p_L), & x < \dfrac{L}{2}, \\ U_R(\rho_R, u_R, p_R), & x > \dfrac{L}{2}, \end{cases} \qquad (4.1)$$

where the length of the shock tube, $L$, which is taken to be unity, $p_R < p_L$ and the diaphragm is located at $x = x_0$.

In this one-dimensional simulation the driver and test gas are assumed to be the same and behave perfectly. The pressure and density ratios across the diaphragm are chosen to be 10:1 and 8:1, respectively, and the ratio of specific heat capacities is chosen to be that of air, $\gamma = 1.4$. The initial states of the vector of conserved variables can be therefore expressed as

$$U_L = \begin{vmatrix} 1.0 \\ 0.0 \\ 1.0 \end{vmatrix} \quad , \quad U_R = \begin{vmatrix} 0.125 \\ 0.0 \\ 0.1 \end{vmatrix} \tag{4.2}$$

A typical set of results obtained with a uniform grid points of N=200 at time t=0.2 seconds are shown in Fig. 4-4. In Fig. 4-4 the red color line indicates the results calculated by the one-dimensional analytical solution, and the green color line indicates the results calculated by the one-dimensional HLLC solver without MUSCL slope limiter. The shock wave, the expansion wave, and the division between the flow traversed by the shock wave and by the expansion wave will be noted. In Fig. 4-4, overall, the agreement between the CFD results and the analytical theory is good, before then criticising the CFD results inability to resolve the discontinuities sharply. It also shows that, because of the relatively small number of grid points used, the shock wave, the contact surface and the expansion wave are not sharp. The region between the contact surface and the expansion wave is poorly captured compared with the same region calculated by the analytical solution. However, the region between the shock wave and the contact surface was captured well. The effect of increasing the number of grid points on the solution is shown in Fig. 4-5, from which it will be seen that the details of the shock wave, the contact surface and the expansion wave are getting better when a larger number of grid points is used.
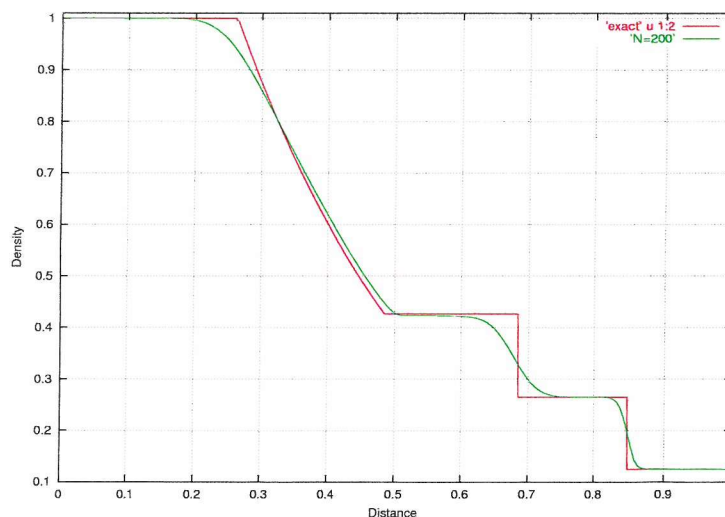


Fig. 4-4 (a) Density profile at t=0.2 using non-MUSCL HLLC solver
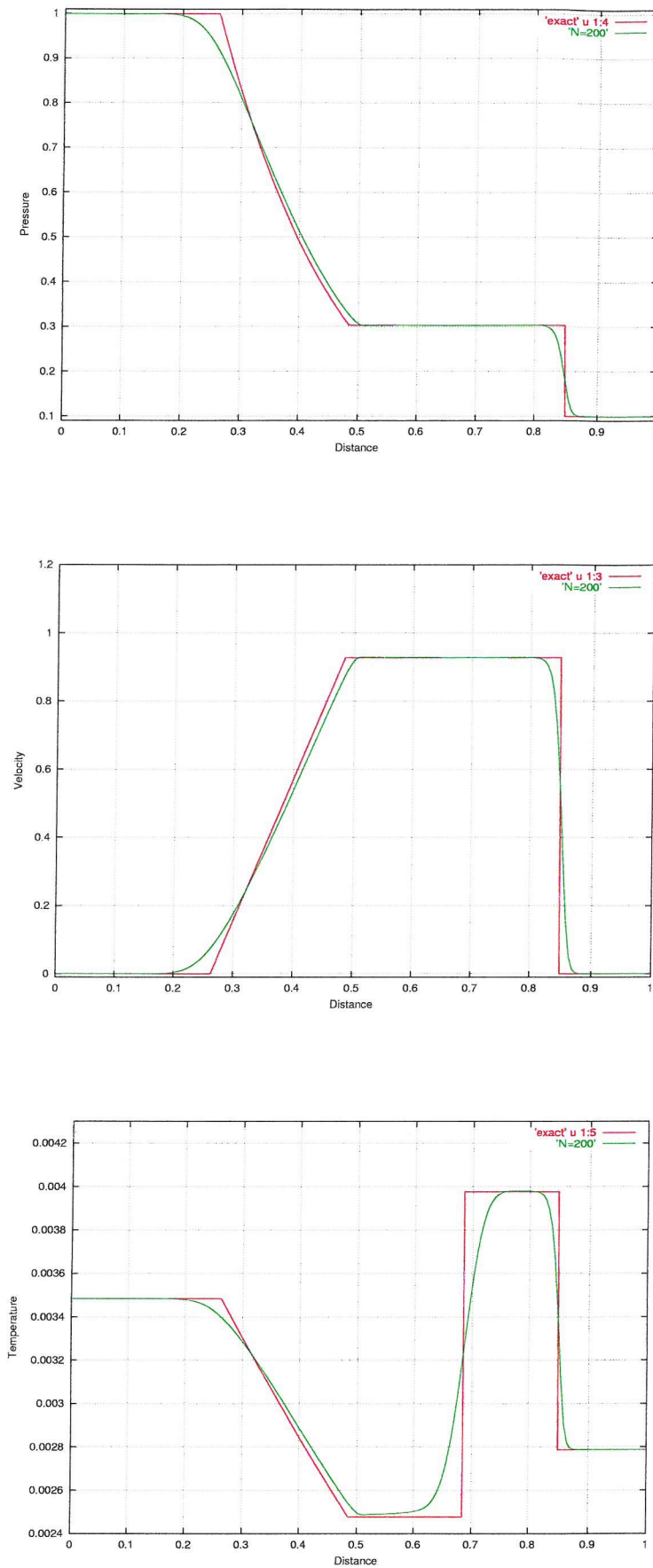
Fig. 4-4 (b) Pressure, velocity and temperature profiles at t=0.2 using non-MUSCL HLLC solver

In Fig. 4-6 it shows that when a number of grid points of 1200 is used, there is no significant change from the details of the shock wave and the contact surface from that when N=1000 is used. This implies that 1000 grid points may be enough for achieving a grid independent solution.

However, ever the grid independent solution shows that a certain amount of numerical diffusion exists near the contact surface in particular (see Fig. 4-5 (b)). As will be shown in the next section, implementing a MUSCL slope limiter improves this situation.
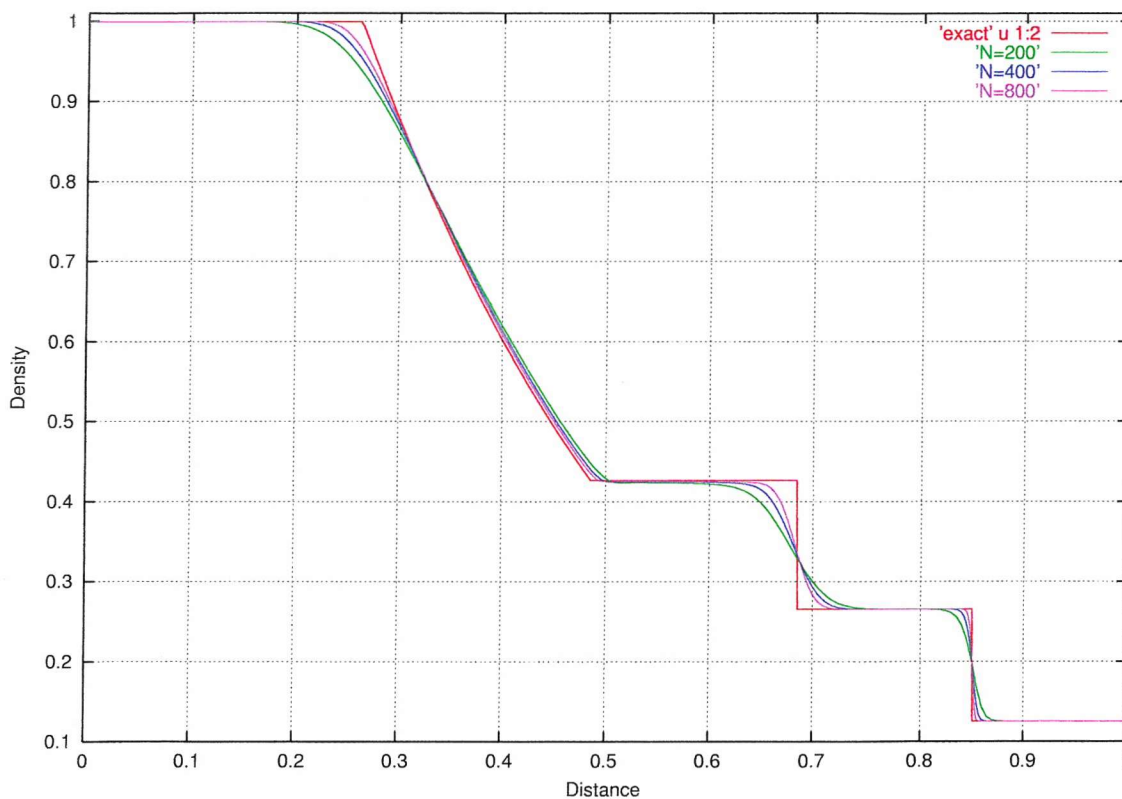


Fig. 4-5 (a) Density profile using non-MUSCL HLLC solver with variable number of grid points
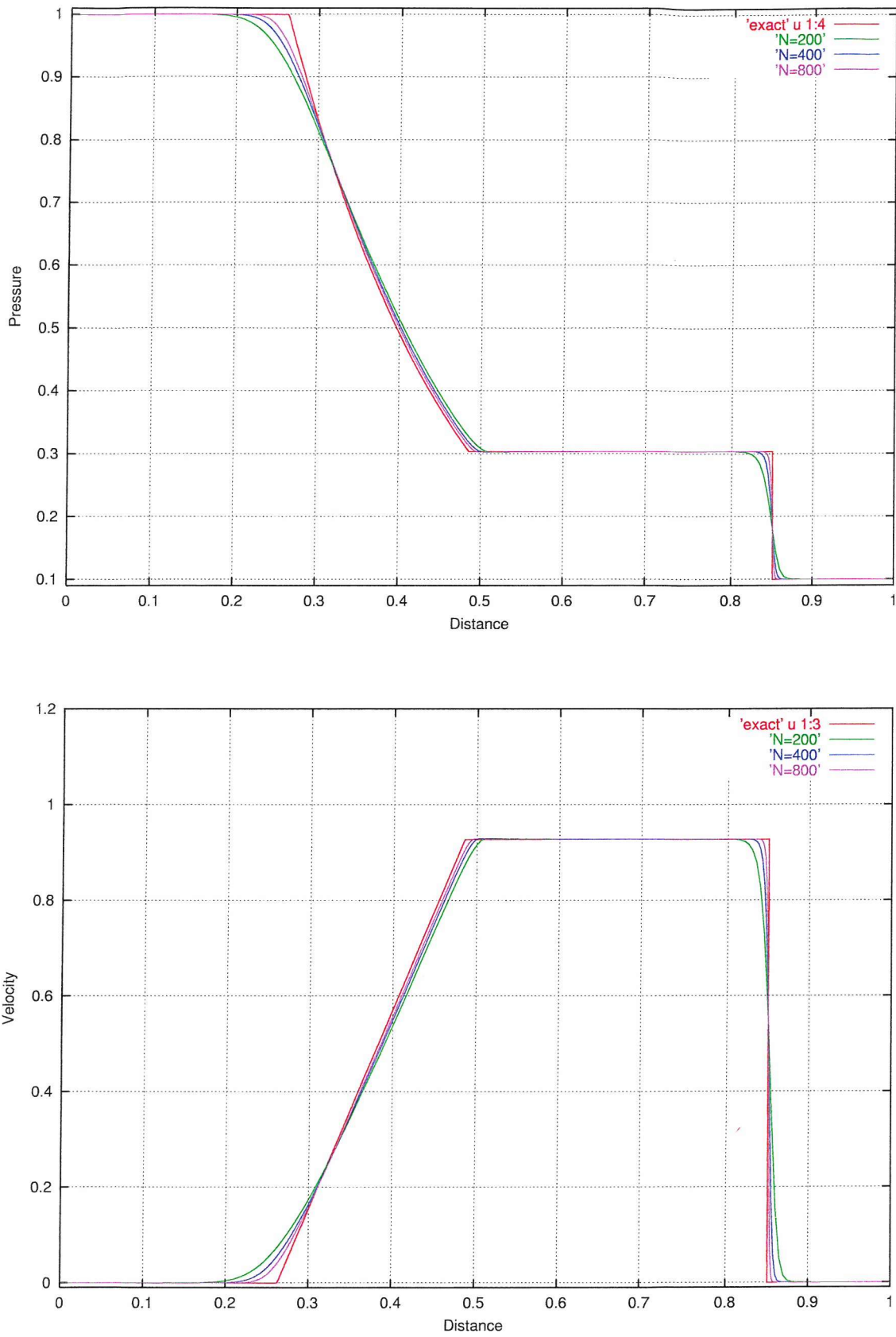
Fig. 4-5 (b) Pressure and velocity profiles using non-MUSCL HLLC solver
with variable number of grid points
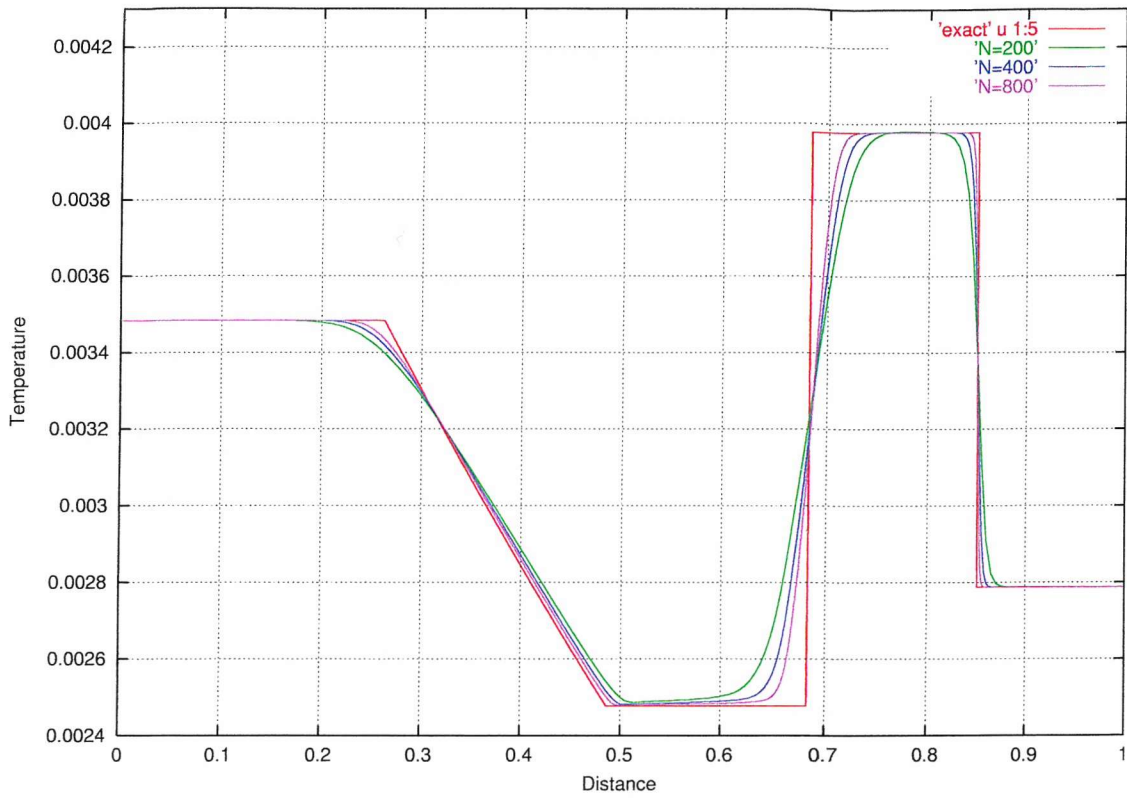
Fig. 4-5 (c) Temperature profile using non-MUSCL HLLC solver with variable number of grid points
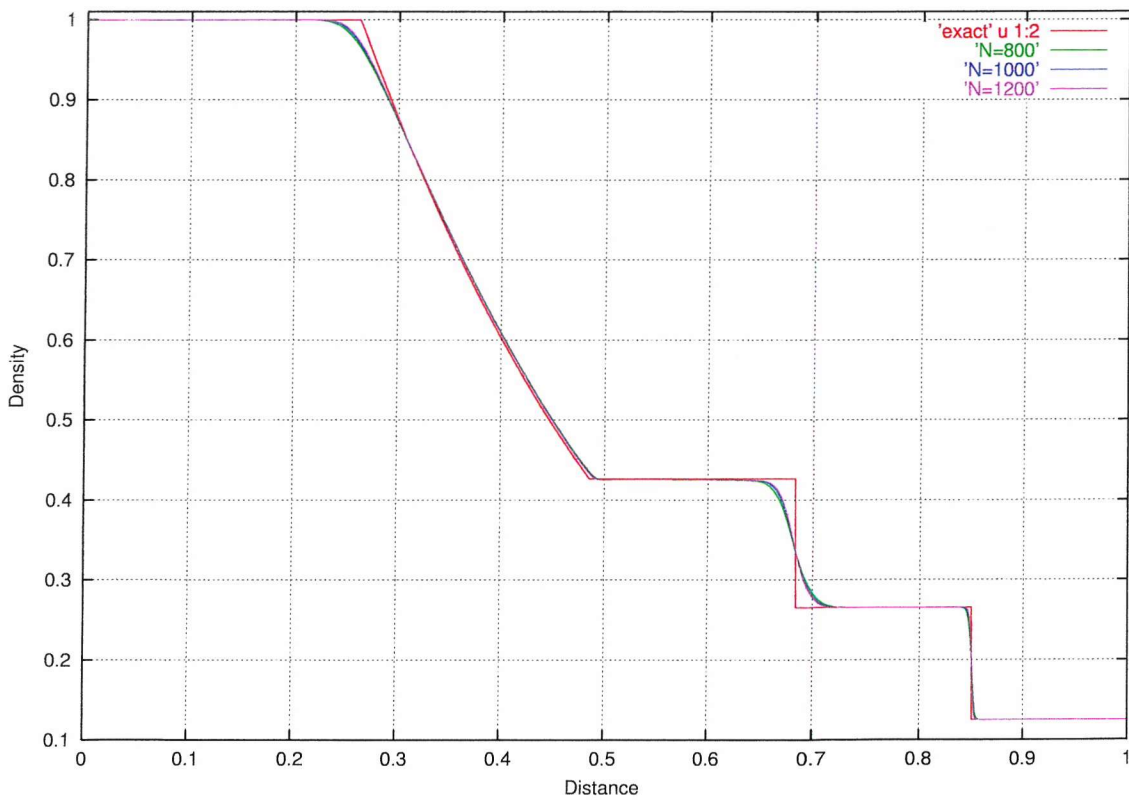


Fig. 4-6 (a) Comparison of density profile using non-MUSCL HLLC solver for N=800, 1000 and 1200
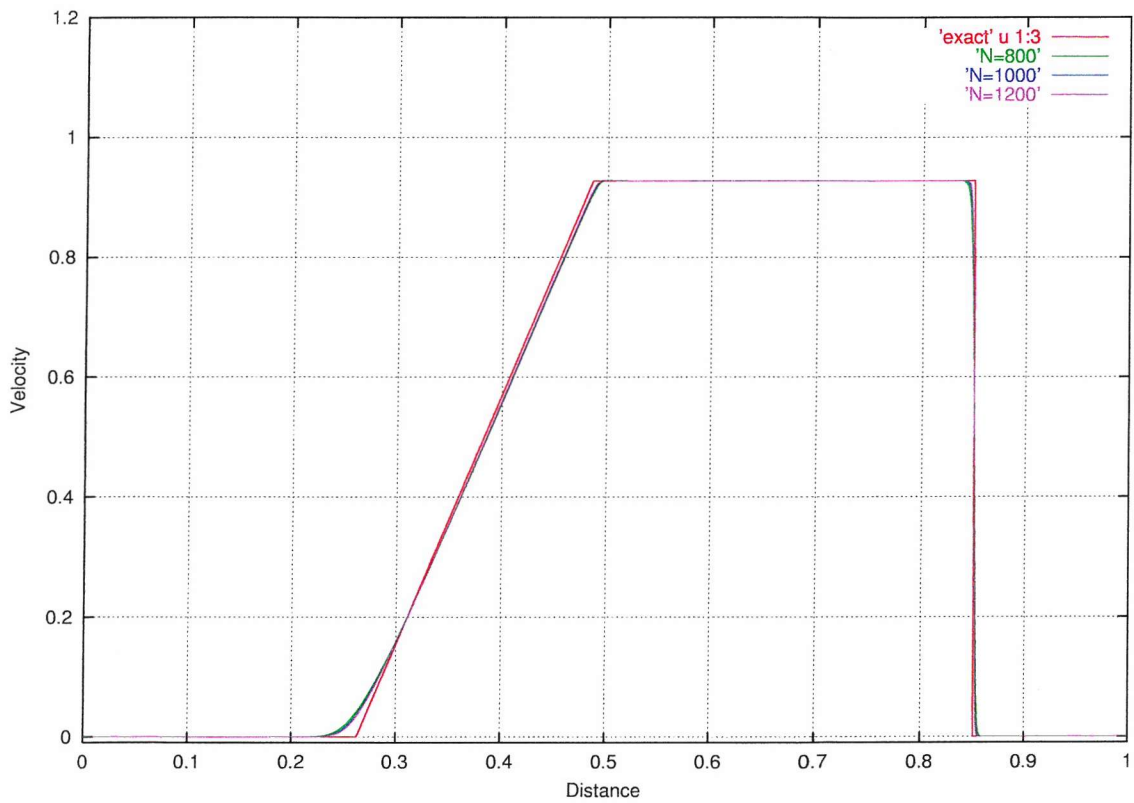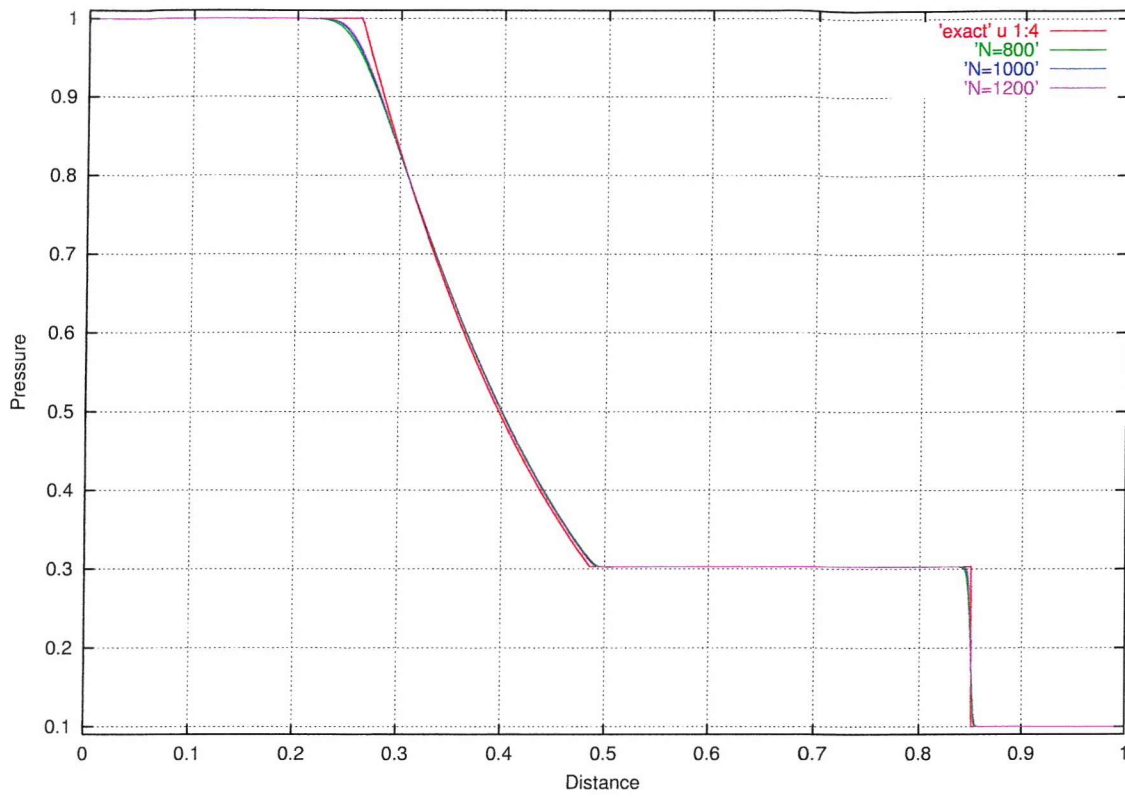
Fig. 4-6 (b) Comparison of pressure and velocity profiles using non-MUSCL HLLC solver
for N=800, 1000 and 1200
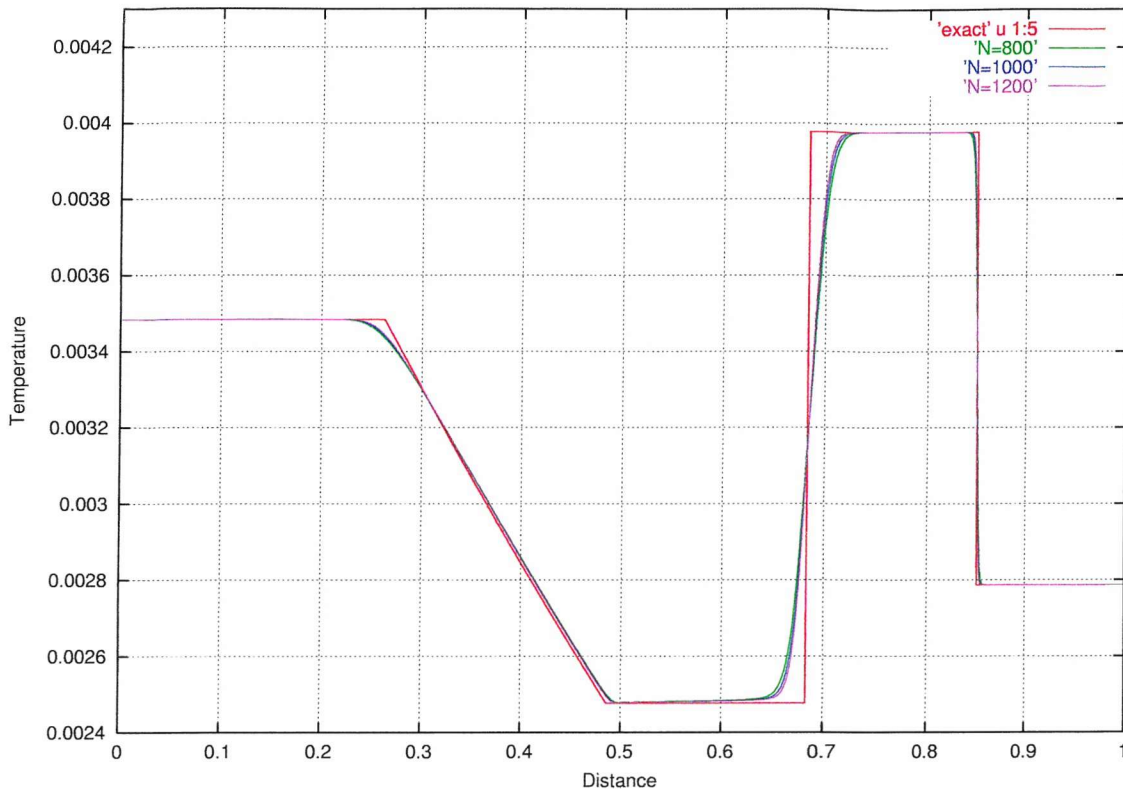
Fig. 4-6 (c) Comparison of temperature profile using non-MUSCL HLLC solver
for N=800, 1000 and 1200

## 4.1.3 1-D simulation with MUSCL solution

Fig. 4-7(a) shows that implementing MUSCL extrapolations, where a number of k=0.8 is used, gives a significant improvement in resolution. Note that, by implementing MUSCL slope limiter, the HLLC solver code becomes effectively second order accurate in space. Fig. 4-8 shows that a number of grid points of 800 may be enough in resolution by using this solution. However, in this resolution, close examination of the results, where a number of grid points of 200, show that there is some little oscillation behavior in the region between the contact surface and the shock wave. By contrast, there is no significant oscillatory behavior in resolution in the non-MUSCL HLLC scheme shown in Fig. 4-7 (b).

Comparing the non-MUSCL HLLC scheme with the MUSCL HLLC scheme, the details of the contact surface and the shock wave show that the MUSCL HLLC scheme gives an apparent improvement in resolution. But, in this solution when a

smaller number of grid points is used, it may be important to choose a suitable value of k for avoiding some little oscillation. However, when a large number of grid points is used, it may be less important to consider a suitable value of k in this solution.

In conclusion, it is suggested that an adequate resolution of the wave phenomena in this case is best obtained by combining the HLLC solver with MUSCL slope limiter with a reasonably large number of grid points.

(a)

(b)
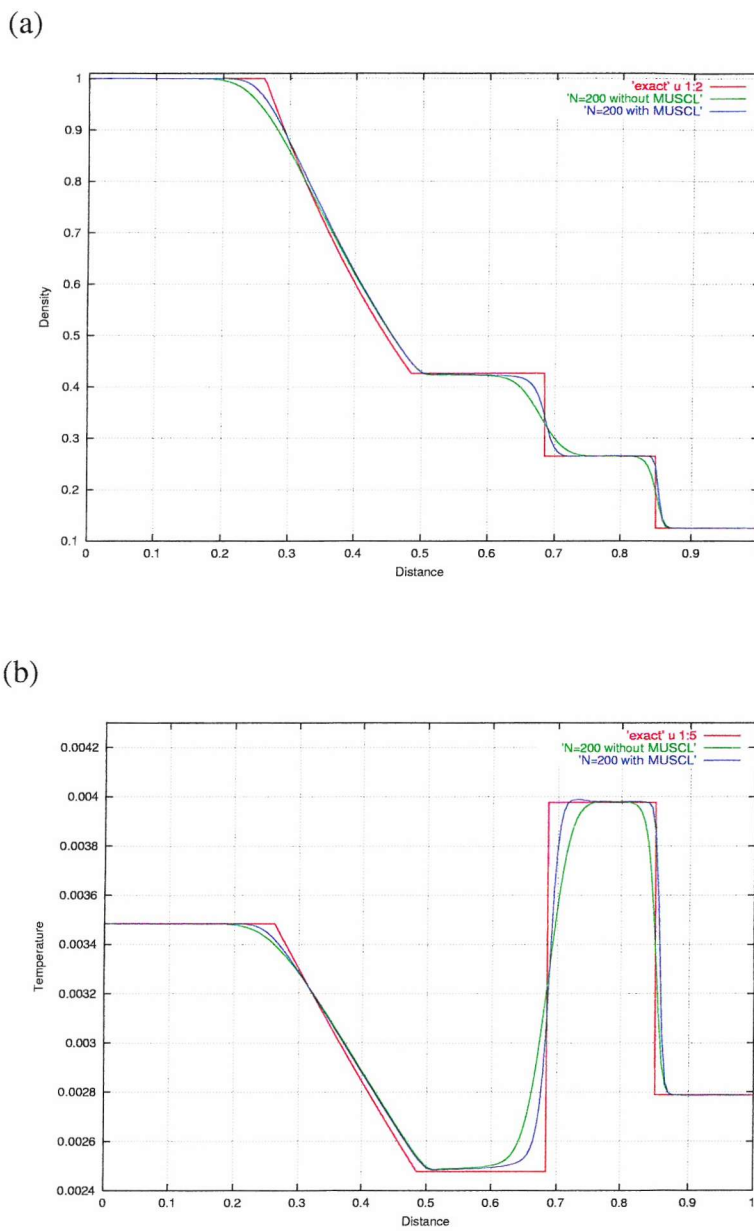
Fig. 4-7 Comparison of density and temperature profiles for N=200
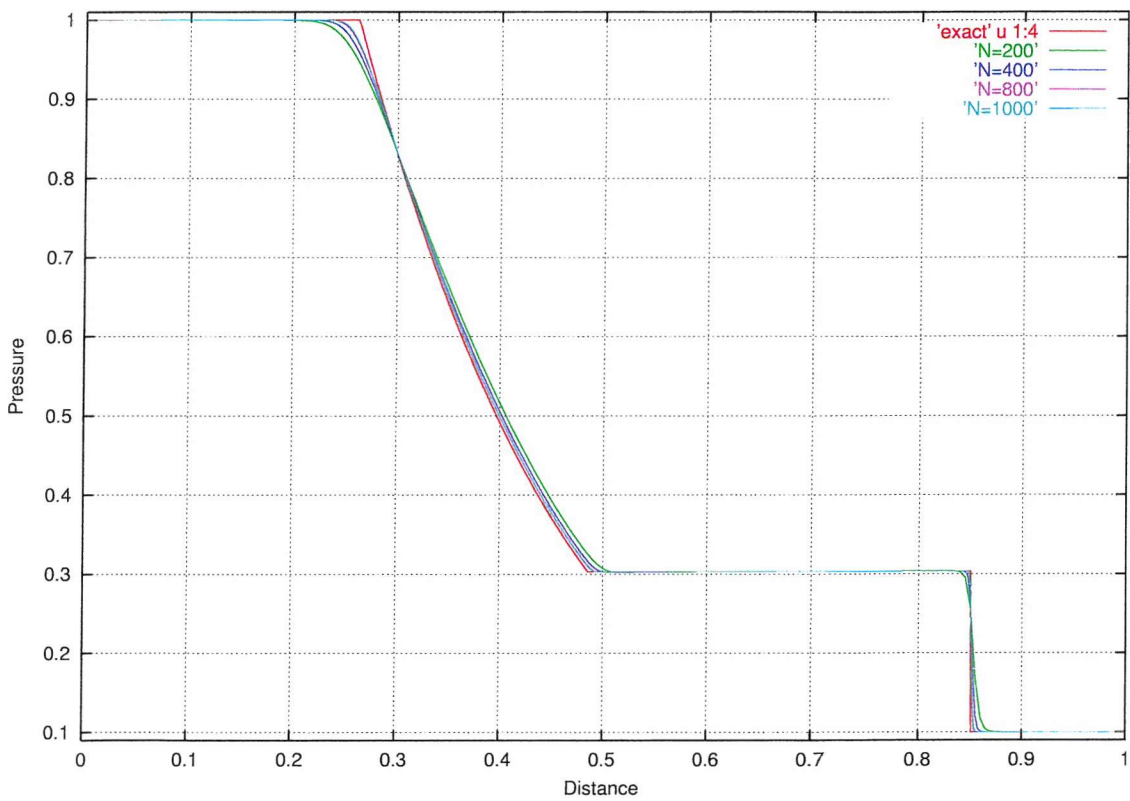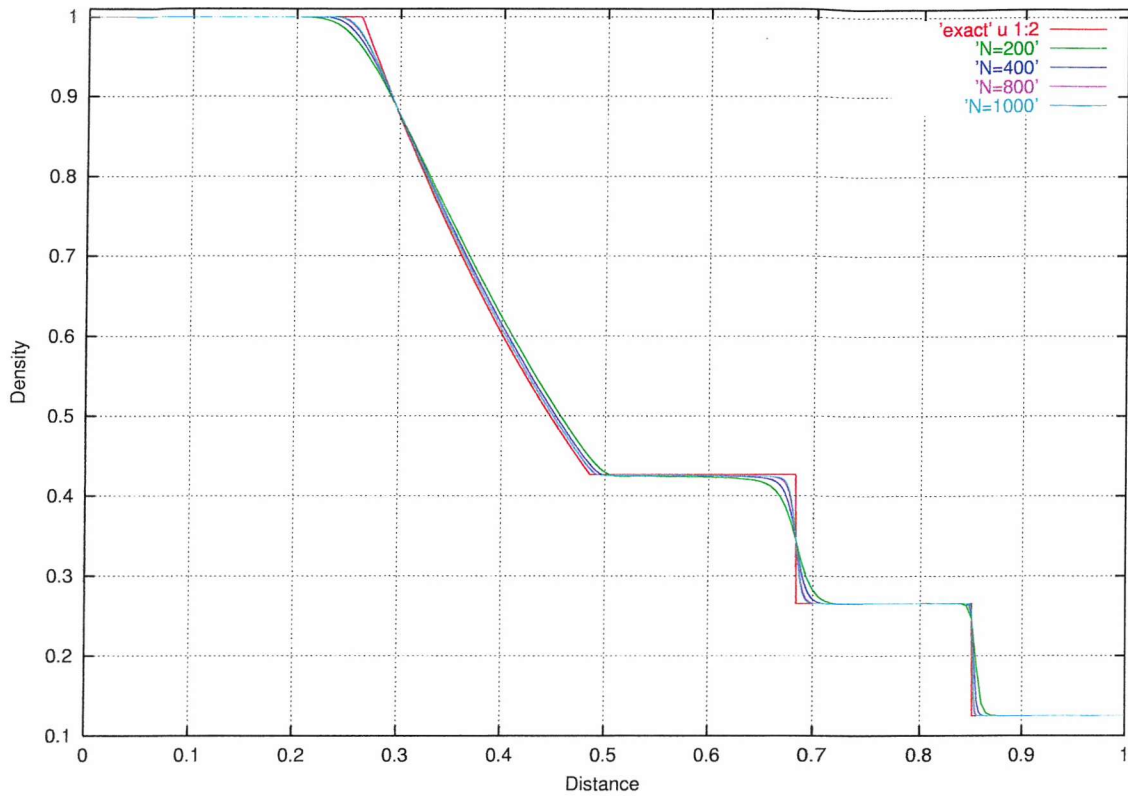
Fig. 4-8 (a) Density and pressure profiles using variable number of grid points with MUSCL
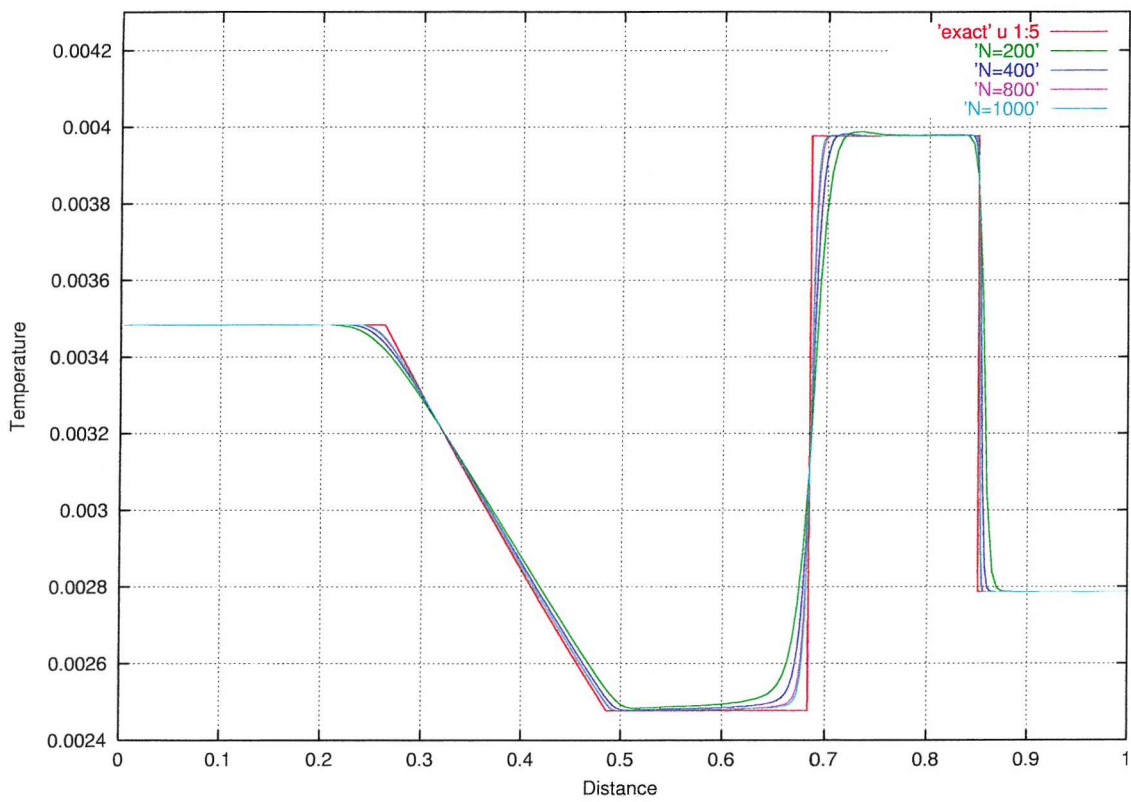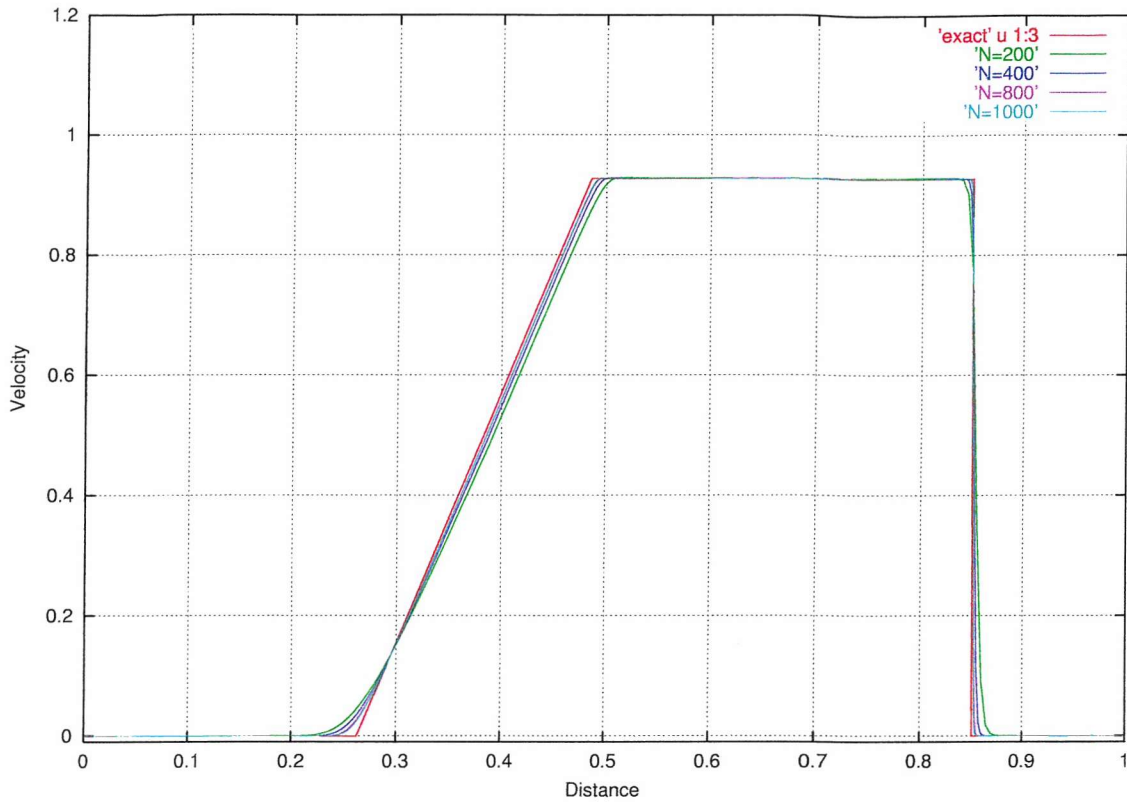
Fig. 4-8 (b) Velocity and temperature profiles using variable number of grid points with MUSCL

## 4.2 Simple Shock Tube

### 4.2.1 Introduction

This section will discuss wave propagation phenomena in simple shock tube without end wall when the high initial pressure ratio ($P_4 / P_1$) of 1000 is used. The grid independent solutions for one-dimensional inviscid and two-dimensional axisymmetric viscous cases will be discussed here. The computed heat transfer rate compared to Mirels' Theory [26, 27, 30] and the duration of the test time will be presented here as well.

### 4.2.2 Grid independent solution

For examining the ability of the non-MUSCL HLLC solver code, a primary diaphragm pressure ratio ($P_4 / P_1$) of 1000 is considered to be a harsh test of the code. The simple shock tube has an overall length of 5.85 *m* and an internal diameter of 0.038 *m*, with the primary diaphragm located at x = 2.11 *m*. Argon is considered as driver and test gas initially at room temperature ($T_4 = T_1 = 300K$). One-dimensional inviscid simulations were performed with uniformly spaced grid points of 1170, 1755 and 2340. The simulations were carried out for times up to 0.003 *sec* after the primary diaphragm burst. The results compared to the one-dimensional analytical solution are shown in Fig. 4-9 and Fig. 4-10. In Fig. 4-10, it shows that when N= 2925 is used, there is no significant change from the details of the shock wave and the contact surface from that when N= 2340 is used. Therefore, N= 2340 may be enough for achieving a grid independent solution for one-dimensional case.

Finally, two-dimensional axisymmetric viscous simulations are also carried out here and the results are shown in Fig. 4-11. The three grid used in the simulations are uniformly spaced on *x*-axis and *r*-axis. It shows that the fine grid (N= 2340 on *x*-axis and N = 70 on *r*-axis) may be enough for achieving a grid independent solution. It also shows that there are some oscillations between the contact surface

and the expansion when the middle grid (N= 1755 on *x*-axis and N= 52 on *r*-axis) and the coarse grid (N= 1170 on *x*-axis and N= 35 on *r*-axis) are used. And there is no significant oscillation between the contact surface and the expansion when the fine grid is used. However, it shows that the numerical diffusion (for the contact surface in particular) is worse when comparing Fig. 4-11 with Fig.4-9. Note that the 'exact' solution shown in Fig. 4-11 is the inviscid results and there is no 'exact' solution for the viscous problem.

The reason to cause some oscillations between the contact surface and the expansion may be due to numerical diffusion when a smaller number of grid points on *r*-axis is used. Hence, it implies that it is important to choose a suitable number of grid points on *r*-axis for avoiding some oscillations caused when the initial pressure ratio ($P_4 / P_1$) is high in this case. Note that, due to the non-steady growth of the boundary layer from the foot of the shock wave, boundary layer properties near the shock wave will not be well reduced no matter how fine the grid. The Reynolds number (based on the diameter of the tube and post-shock freestream conditions) in the viscous solution is approximately $1.95 \times 10^4$.

### 4.2.3 Primary shock speed

From the details of the inviscid shock wave shown in Fig. 4-9, it shows that the shock front positions appear to be incorrect although they have good agreements in the expansion pattern and the region between the contact surface and the shock wave. It also shows that the more the grid points are given, the closer the shock front moves backward to the analytical shock front position. The computed shock (IS) speeds with variable number of grid points compared to the analytical shock (AS) speed are shown in Table 1. The shock speeds are obtained by the distance between two specific locations divided the time difference when the shock arrives the two locations respectively.

A one-dimensional inviscid distance-time wave diagram with grid points of 2340 compared to the analytical solution is shown in Fig. 4-12. It shows that at the

pressure ratio ($P_4/P_1$) of 1000, there is an initial overestimation of shock speed, but the speed of the inviscid shock (IS) decays to the speed of the analytical shock (AS) near the end of the shock tube. It shows that the inviscid and analytical speeds seem to be quite constant in Fig. 4-12, except near the diaphragm. This implies that longer tube length may be required to decay to the analytical shock speed when the initial pressure ratio ($P_4/P_1$) increases. Petrie-Repar and Jacobs [33] explained that the initial overestimation of shock speed when the initial pressure ratio ($P_4/P_1$) is high is due to numerical diffusion, particularly at the contact surface. Sheng et al [40] also described that the smearing of cold and hot gas interfaces is caused by numerical diffusion. Numerical diffusion becomes greater when the distance that the interface travels increases, especially in a strong shock.

Table 1. Comparison of the one-dimensional inviscid computed shock speeds
and the analytical shock speed

|  | Analytical solution | 1170 grid points | 1755 grid points | 2340 grid points |
|---|---|---|---|---|
| Initial (at 2.50m) | 898.74 m/s | 945.89 m/s | 921.18 m/s | 917.07 m/s |
| End (at 5.85m) | 898.74 m/s | 939.48 m/s | 914.11 m/s | 910.71 m/s |

Finally, the computed shock speeds of viscous flow with variable number of grid points compared to the analytical shock speed are shown in Table 2. It shows that the viscous shock (VS) speeds appear to be reduced to be smaller than the analytical shock speed due to the viscous effects. Fig. 4-13, a distance-time plot for the viscous flow also shows that the contact surface (labelled VCS) appears to be accelerated and the shock front is decelerated due to the growth of the boundary layer. For the finest grid used, the final shock speed in the viscous case is approximately 9.5% slower than in the inviscid case at these conditions.

These results obtained with the viscous flow model appear to be consistent with Mirels' theory [30]. A more detailed comparison with this theory will be discussed in the next section.

Table 2. Comparison of the two-dimensional axisymmetric viscous computed shock speeds and the analytical shock speed

|  | Analytical solution | 1170x35 grid points | 1755x52 grid points | 2340x70 grid points |
|---|---|---|---|---|
| Initial (at 2.50m) | 898.74 m/s | 939.27 m/s | 938.84 m/s | 910.47 m/s |
| End (at 5.85m) | 898.74 m/s | 867.17 m/s | 839.21 m/s | 825.1 m/s |
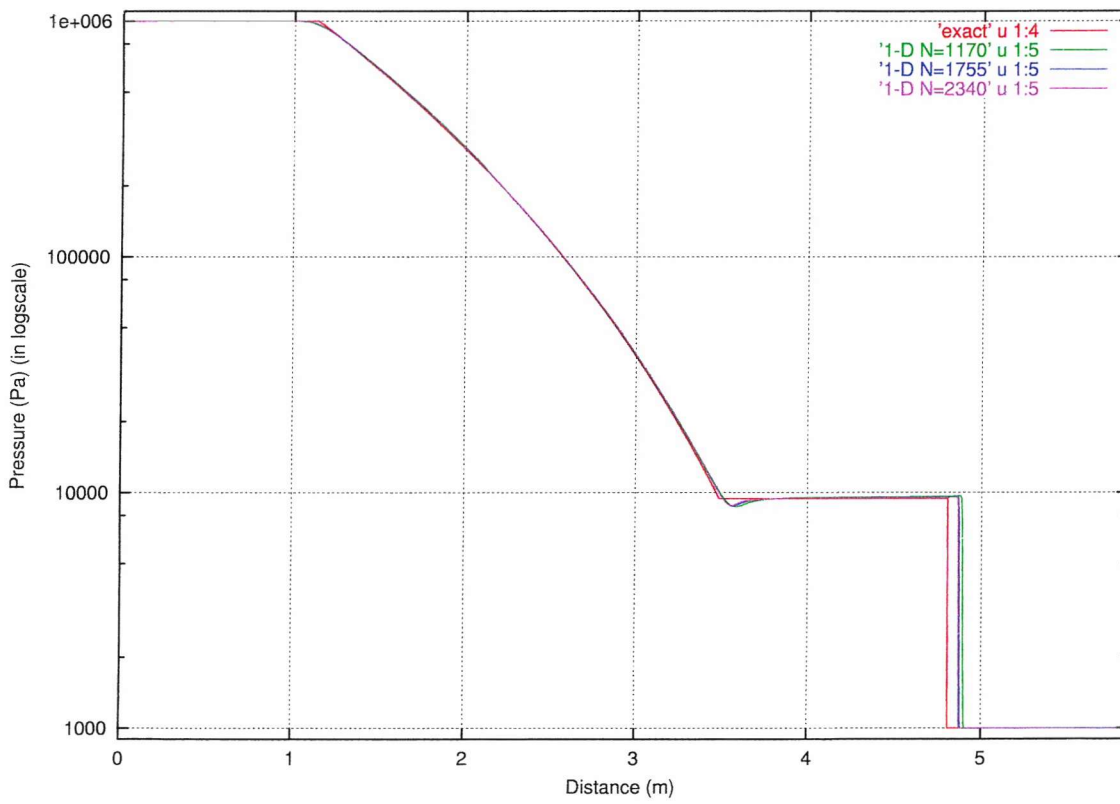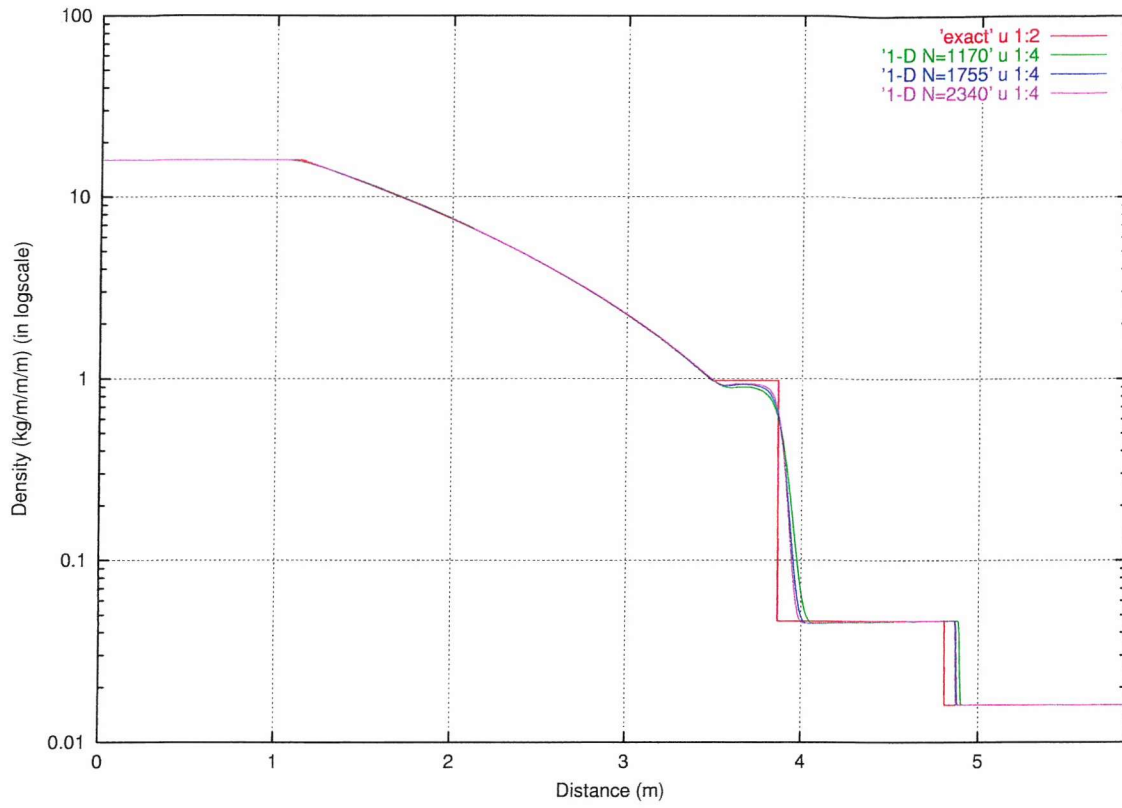
Fig. 4-9 (a) Density and pressure profiles of one-dimensional inviscid simulations
at 0.003 sec for grid independent solutions
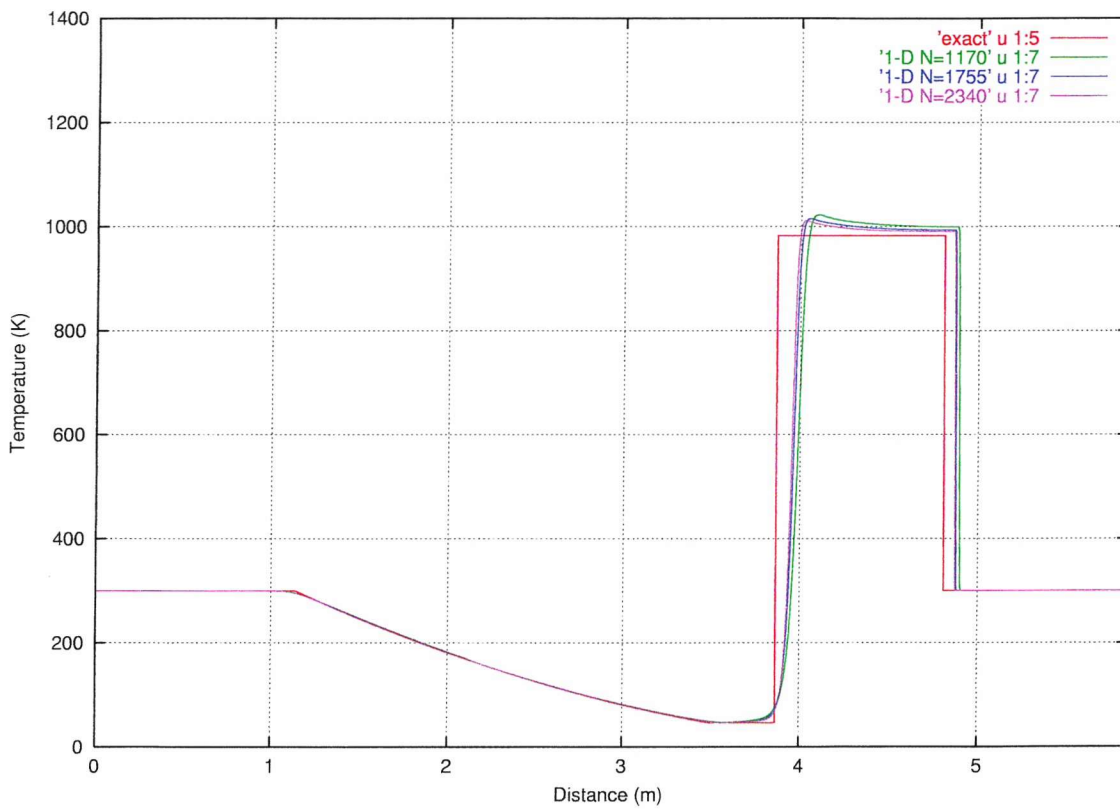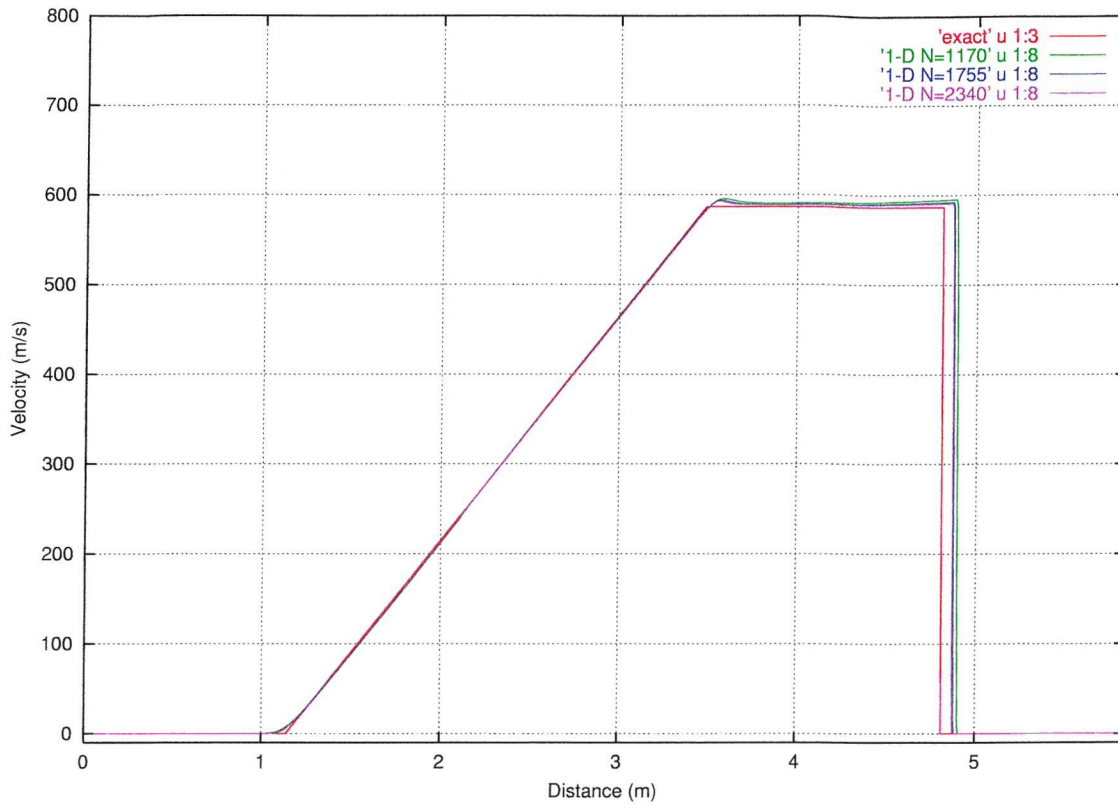
Fig. 4-9 (b) Velocity and temperature profiles of one-dimensional inviscid simulations
at 0.003 sec for grid independent solutions
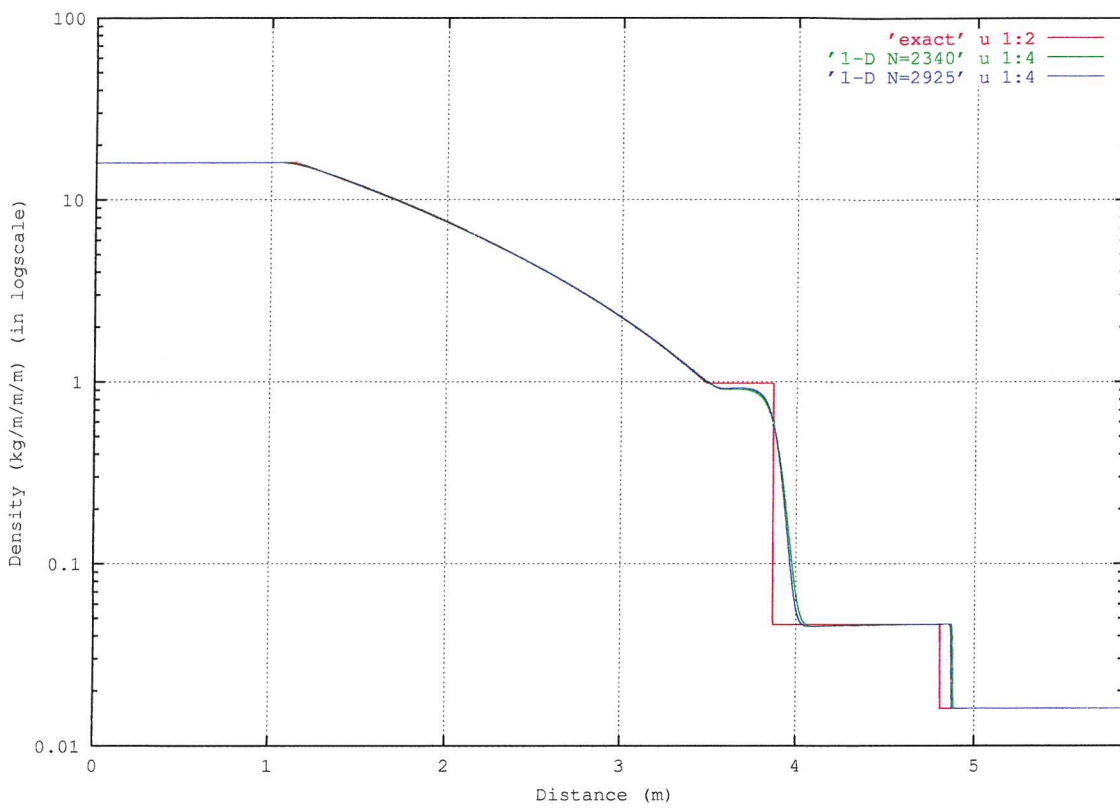
Fig. 4-10 Comparison of the density profiles for one-dimensional inviscid simulations at 0.003 sec when N=2340 and N=2925 are used
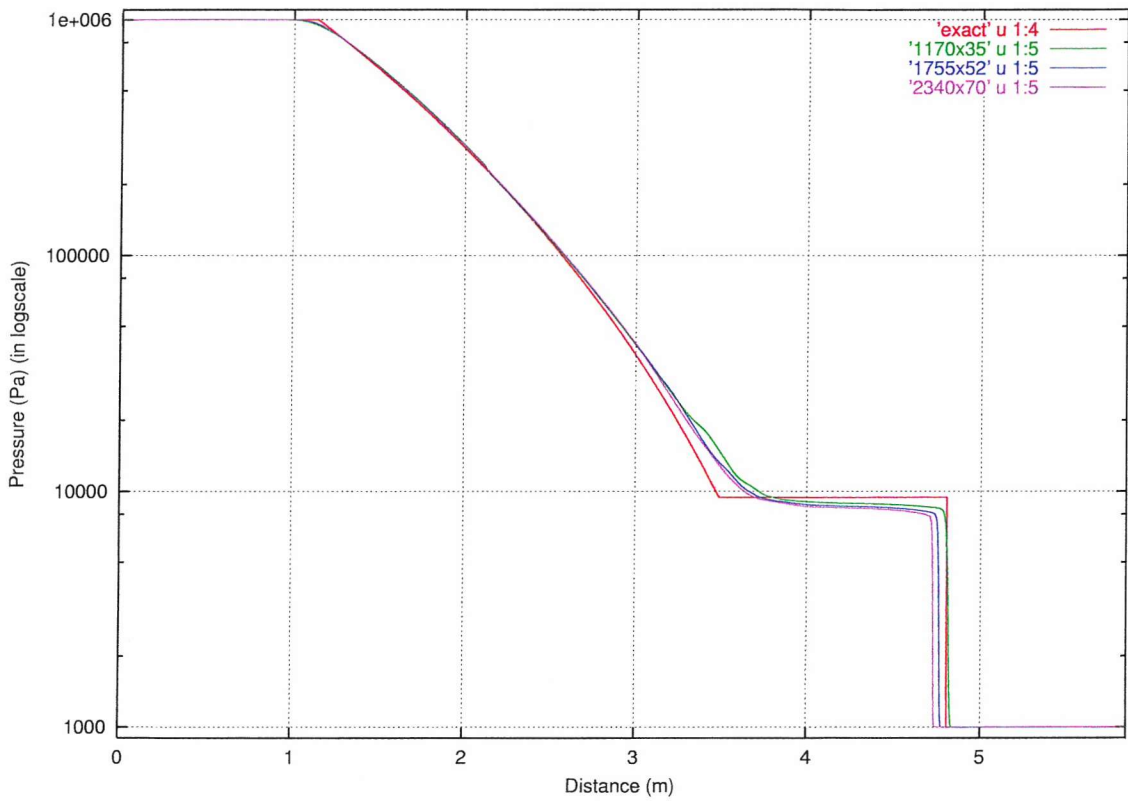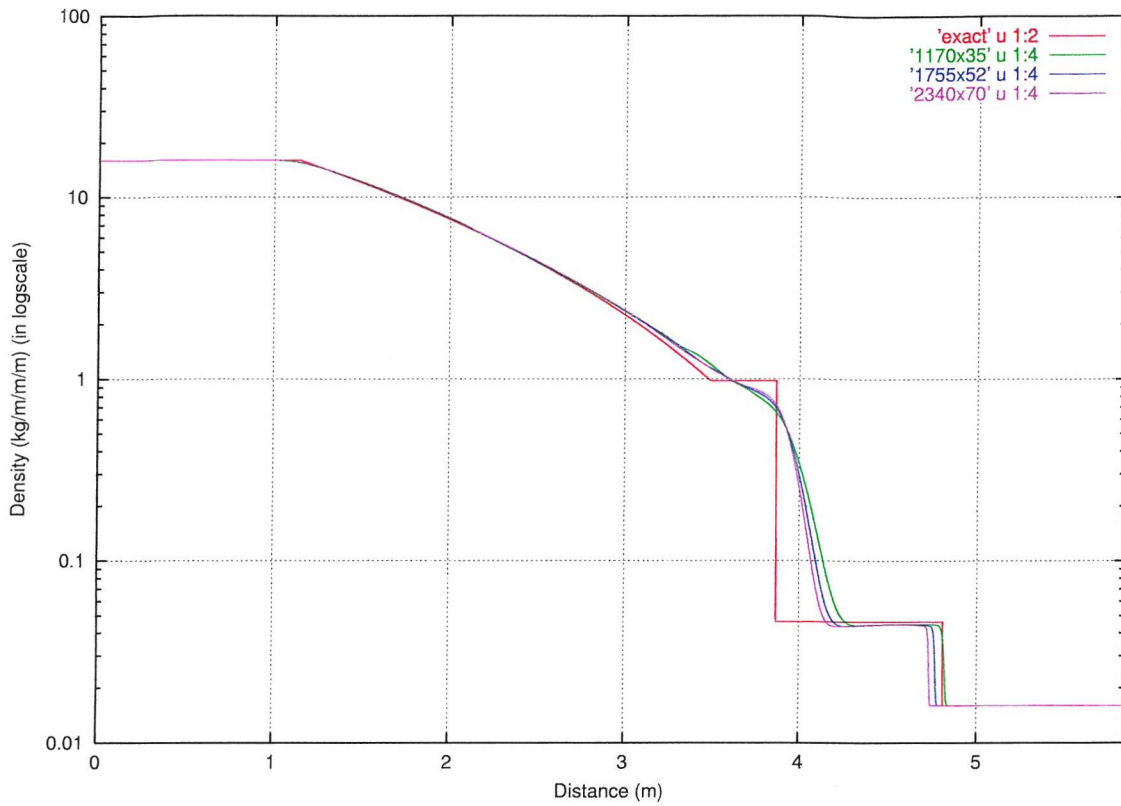
Fig. 4-11 (a) Density and pressure profiles of two-dimensional axisymmetric viscous simulations at 0.003 sec for grid independent solutions
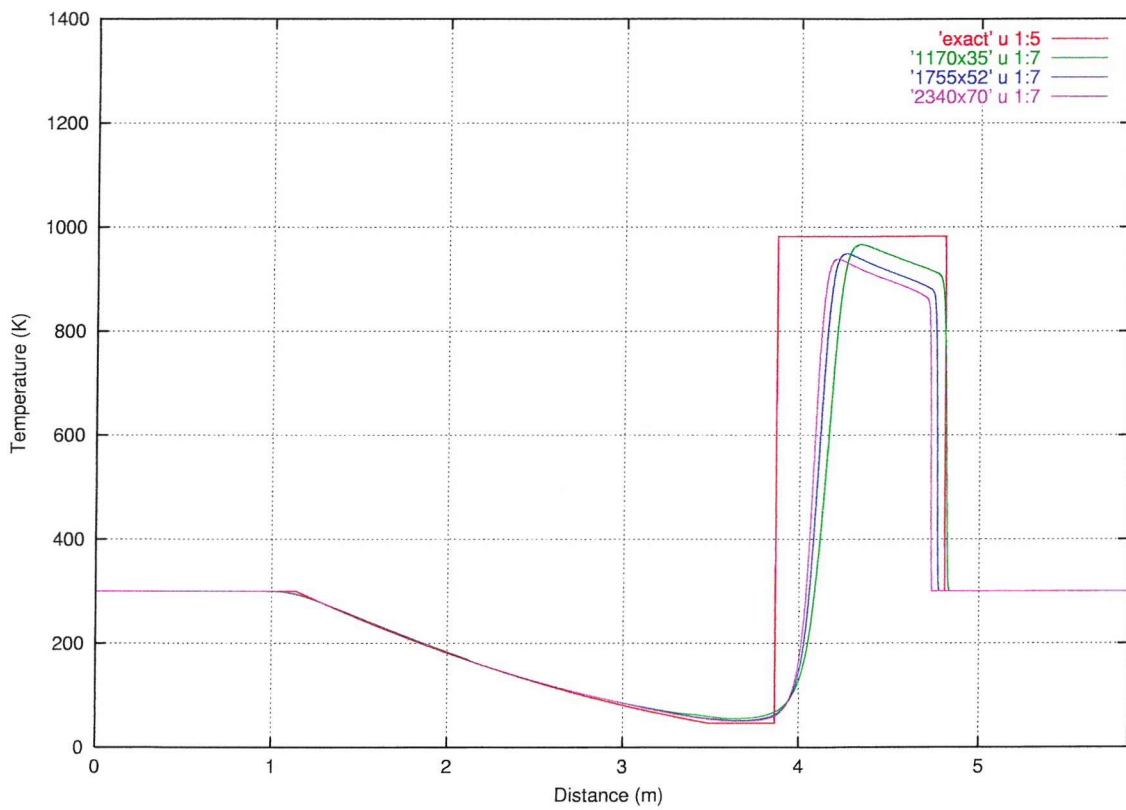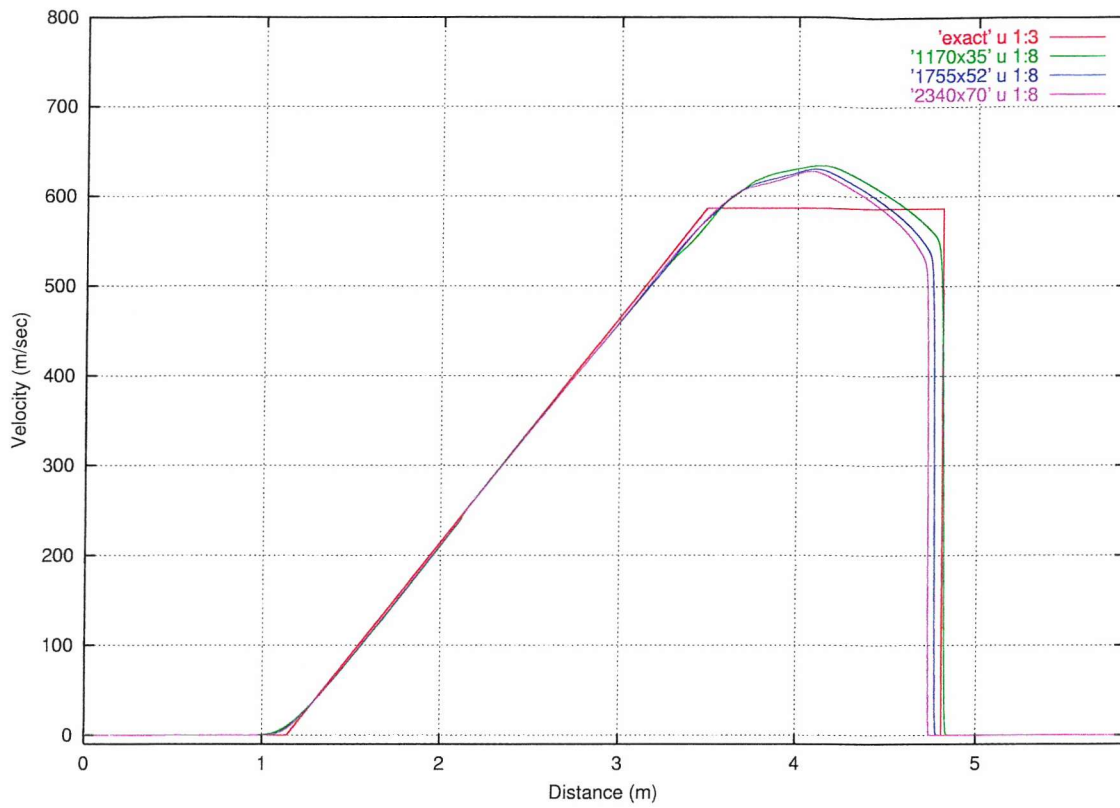
Fig. 4-11 (b) Velocity and temperature profiles of two-dimensional axisymmetric viscous simulations at 0.003 sec for grid independent solutions
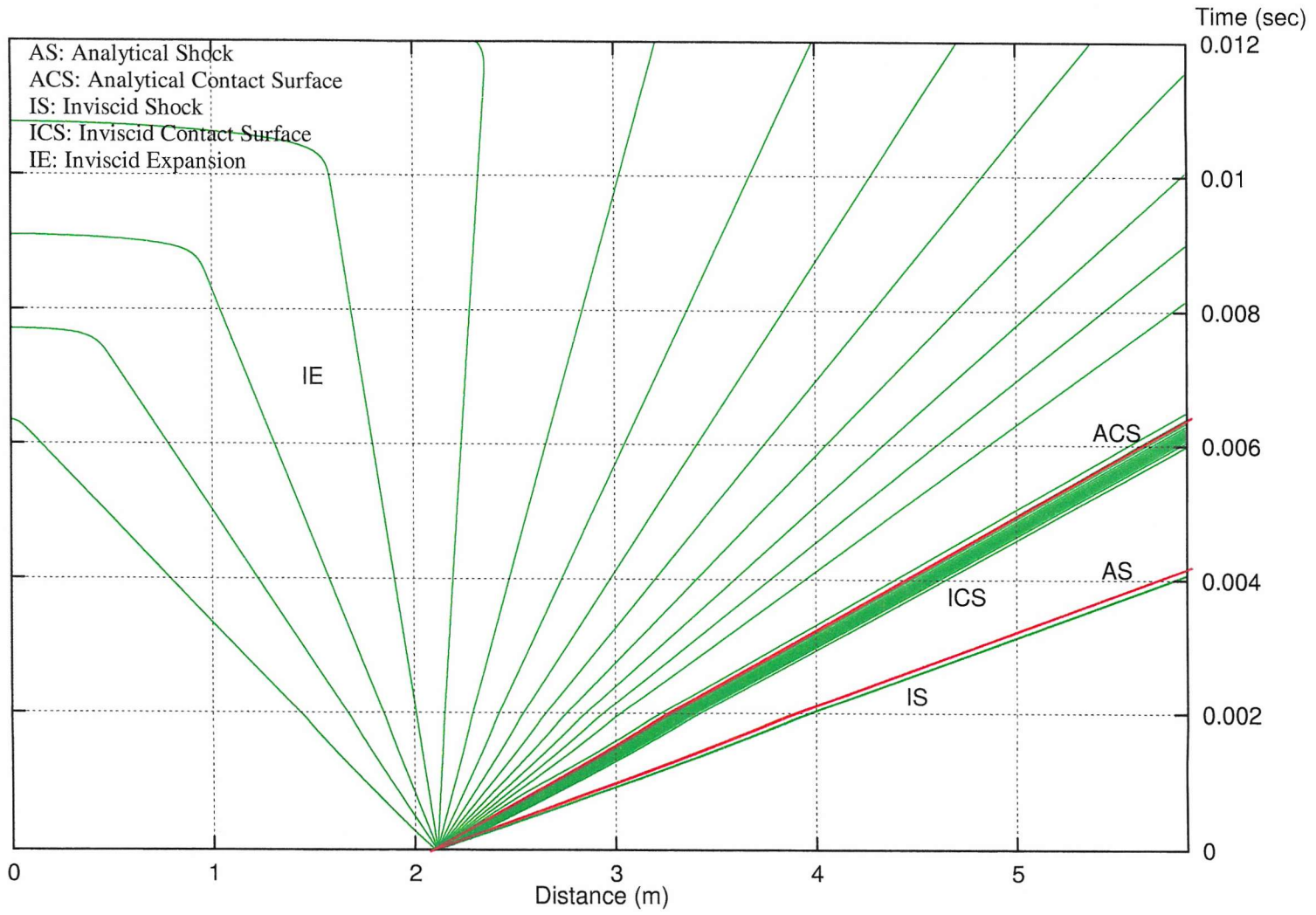
Fig. 4-12 Wave diagram of the density profile for 1-D inviscid simulation

AS: Analytical Shock
ACS: Analytical Contact Surface
VS: Viscous Shock
VCS: Viscous Contact Surface
VE: Viscous Expansion

VE

Time (sec)

VCS

ACS

VS

AS

Distance (m)
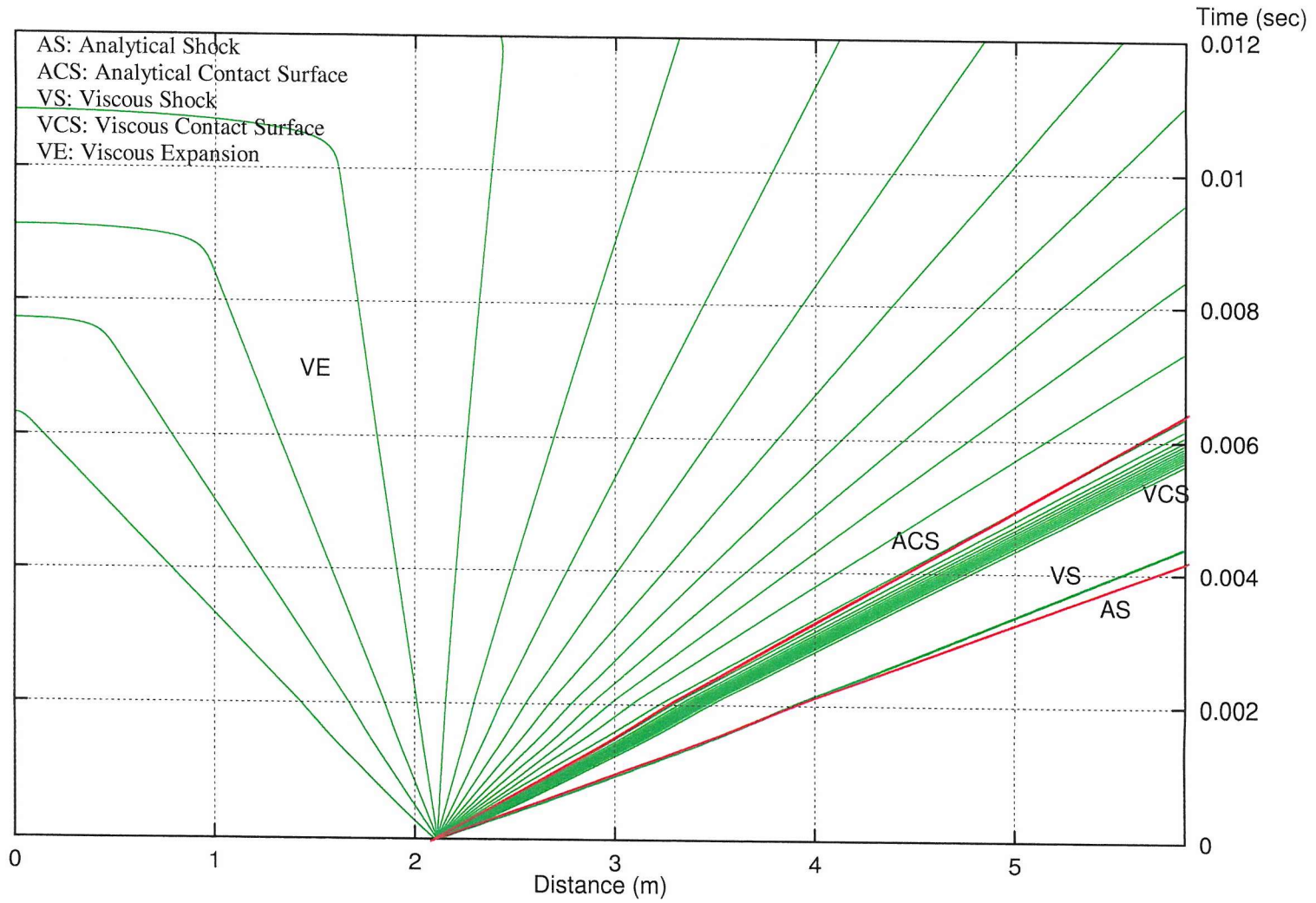
Fig. 4-13 Wave diagram of the density profile for 2-D axisymmetric viscous simulation

## 4.2.4 Boundary Layers

In an ideal inviscid shock tube flow, the primary shock wave and the contact surface propagate at contact speeds and the separation distance between them increases linearly with distance from the diaphragm as shown in Fig. 4-14 (a). However, in a real viscous shock tube flow shown in Fig. 4-14 (b), when the shock travels toward the end of the tube, the flow behind the shock and ahead of the expansion fan near the wall forms a region of velocity lag due to the viscous friction along the wall. The region of the velocity lag is the boundary layer. Fig. 4-15 shows that the boundary layer can be seen in the two-dimensional axisymmetric viscous simulation.

Hence, the wall boundary layer between the shock wave and the contact surface acts as an aerodynamic sink and absorbs mass from this region. This causes the contact surface to accelerate and the shock wave to decelerate and reduces the separation distance $l$ below the ideal value, as is also shown in Fig. 4-14 (a). The results of the numerical modeling appear to illustrate these phenomena, as described in the previous section.

### 4.2.4.1 Wall heat transfer

To test the accuracy of the numerical code, the wall heat transfer behind the shock at the end is evaluated as a function of time. Mirels' theory [30] for laminar boundary layer heat transfer rate is used to compare with the computed heat transfer rate. Mirels considered the laminar boundary layer development behind a moving shock front. In general, in the shock tube, the development is unsteady in a laboratory coordinate system, but is steady in a shock-fixed coordinate system. In Fig. 4-14 (b), assume $u_s$ is the shock speed. Therefore, the wall moves with a velocity $u_w$ equals to $-u_s$ in a shock-fixed coordinate system. Then the post-shock freestream velocity $u_2$ in a laboratory coordinate system can be defined to relate to $u_e$ in a shock-fixed coordinate system by:
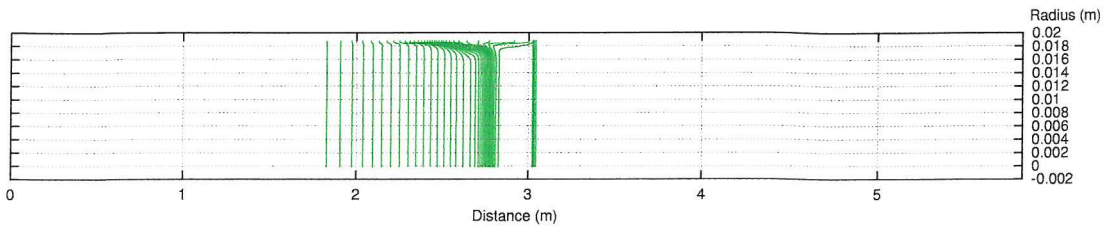
Expansion fan

Inviscid
Contact surface

Contact surface
with boundary layer

$t$

$lm$

$l$

Shock wave with
boundary layer

Inviscid shock wave

$x$

(a) *x-t* diagram

Expansion Fan

Boundary layer

Contact Surface
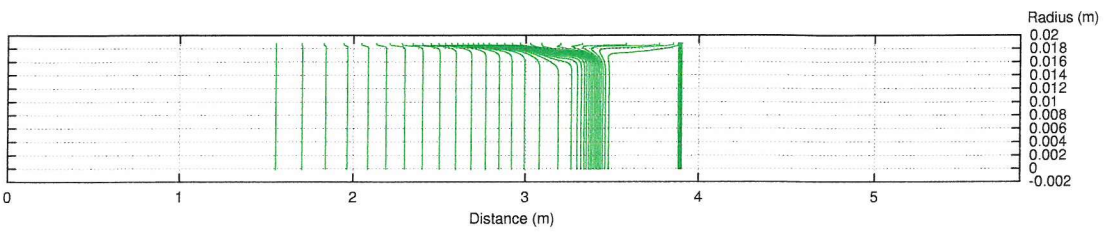
$u_c$  $u_2$  $U_s$

Shock wave
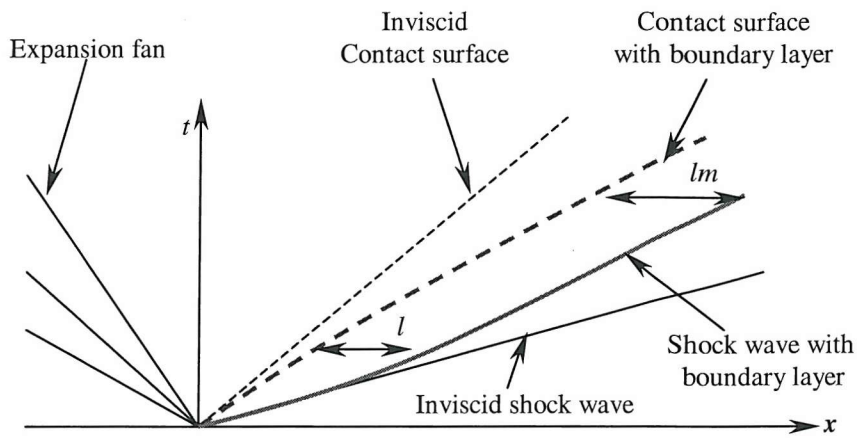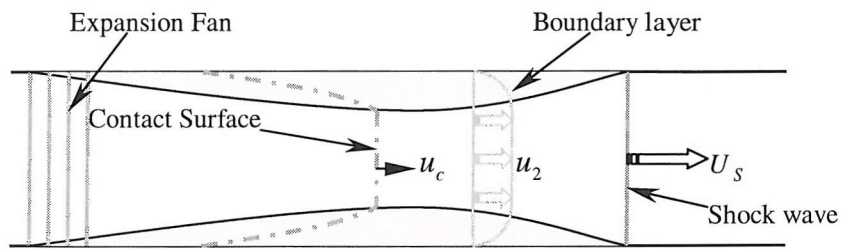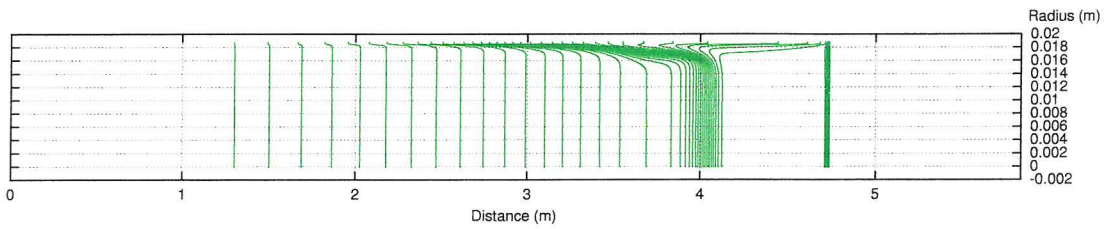
(b) Flow features in laboratory coordinates

Fig.4-14 Boundary layer effect on viscous flow in a shock tube

At 0.001 *sec*



At 0.002 *sec*



At 0.003 *sec*
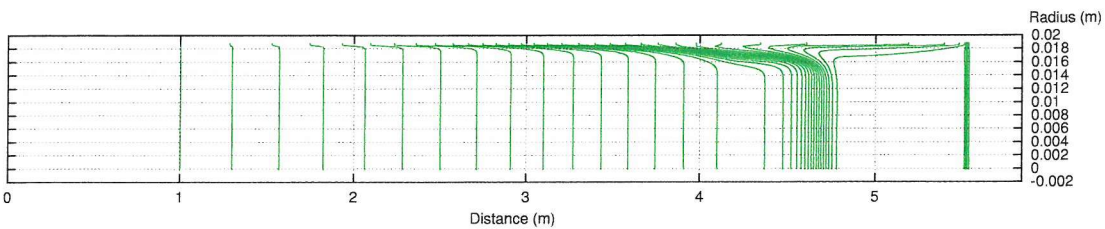


At 0.004 *sec*

Fig. 4-15 Density contours showing the separation distance and boundary layer
of the viscous shock tube flow

$$u_2 = u_w - u_e \qquad (4.3)$$

In laminar boundary layer flow the boundary conditions for $x > 0$ according to a shock-fixed coordinate system can be defined as:

$$u(x,0) = u_w, \qquad u(x,\infty) = u_e,$$
$$v(x,0) = 0, \qquad\qquad\qquad (4.4)$$
$$T(x,0) = T_w, \qquad T(x,\infty) = T_e = T_2,$$

In the problems considered here, the wall temperature $T_w$ is assumed to be constant. The magnitudes of $u_e$, $T_e$ and $u_s$ depending on the shock strength can be defined from the normal shock relations described in Appendix C. The velocity profile $u(x, y)$ can be defined to be in terms of a function $f(\eta)$, where $\eta$ is a similarity parameter and $u/u_e = f'$, where primes denote $\partial/\partial\eta$ [26]. Since $Pr$, $c_p$ and $\rho\mu$ are assumed constant, the energy equation may be linear and the general solution for the temperature profile may be expressed as the linear superposition of the solution for zero heat transfer plus the effect of heat transfer by

$$\frac{T}{T_e} = 1 + \left[\frac{u_w}{u_e} - 1\right]^2 \frac{u_e^2 r(\eta)}{2T_e c_p} + \left[\frac{T_w}{T_e} - \frac{T_r}{T_e}\right] s(\eta) \qquad (4.5)$$

with two functions $r(\eta)$ and $s(\eta)$ are expressed, respectively, as

$$\left.\begin{array}{c} r'' + Pr\, fr' = \dfrac{-2Pr}{(u_w/u_e - 1)^2}(f'')^2 \\[4mm] r(\infty) = r'(0) = 0 \end{array}\right\} \qquad (4.6)$$

and

$$s'' + Pr \, fs' = 0$$
$$s(0) = 1; \quad s(\infty) = 0$$

(4.7)

Here, the recovery temperature $T_r$ can be expressed as:

$$\frac{T_r}{T_e} = 1 + \left[ \frac{u_w}{u_e} - 1 \right]^2 \frac{u_e^2 r(0)}{2 T_e c_p}$$

(4.8)

Then Mirels [27] deduced interpolation formulae from a series of integrations, giving an explicit dependence for $\dot{q}_w$ on $u_w/u_e$ and $Pr$

$$\dot{q}_w(t) = s'(0)(T_r - T_w) \frac{c_p}{Pr} \left[ \frac{u_e \rho_w \mu_w}{2 x(t)} \right]^{\frac{1}{2}}$$

(4.9)

where

$$x(t) = u_w(t - t_0),$$

(4.10)

$$r(0) = (Pr)^{0.39 - 0.023 \left( \frac{u_w}{u_e} \right)}$$

(4.11)

and

$$s'(0) = 0.489 \sqrt{1 + 1.665 \frac{u_w}{u_e}} \, Pr^{0.48 + 0.02 \left( \frac{u_w}{u_e} \right)}$$

(4.12)

Here, $t_0$ is the time when the shock wave arrives at the measuring station.

Mirels also noted that the equations should be valid for test gases with $0.6 < Pr < 1.0$. Later, Mirels [30] presented correlation formulas for $1 \le u_w/u_e \le \infty$ and allowing real gases effects. In these improved correlation formulas, he defined the normalized velocity and static enthalpy profiles as:

$$\phi'(\eta) = \frac{W - u/u_e}{W - 1},$$ (4.13)

$$G(\eta) = \frac{\chi - h/h_e}{\chi - 1}$$ (4.14)

where $W = u_w/u_e$ and $\chi = h_w/h_e$. Then the heat transfer rate was revised as:

$$\dot{q}_w = \frac{\mu_w}{Pr} \frac{h_e - h_w}{\beta \, \rho_e/\rho_w} G'(0)$$ (4.15)

where

$$\beta = \frac{\rho_w}{\rho_e} \left[ \frac{2x\upsilon_w}{u_w - u_e} \right]^{\frac{1}{2}}.$$ (4.16)

And the improved interpolation formulae for constant $\rho\mu$ give:

$$G'(0) = Pr^{\frac{1}{2}} \phi''(0) \left[ 1 + \frac{W - 1}{W + 1} Pr^{0.54} \right]$$ (4.17)

and

$$\phi''(0) = \frac{0.7979}{\sqrt{(W - 1)}} \left[ 1 + 1.285(W - 1) + 0.3827(W - 1)^2 \right]^{\frac{1}{4}}$$ (4.18)

The correction formulas of Mirels were verified experimentally (with Argon as a test gas) by Roberts [34]. The improved wall heat transfer rate with prediction of Mirels' theory [30] compared to the computed heat transfer rate at x = 5.85 *m* is shown in Fig. 4-16. It shows that the time of arrival of the primary shock with the finest grid is approximately 0.004374 *sec*. The infinite heat flux predicted by Mirels' theory is not predicted by the numerical code. It also shows that the agreement between the numerical result with the finest grid and Mirels' theory is quite good until t = 0.0062 *sec*. From Fig. 4-13, the distance-time plot, t = 0.0062

*sec* corresponds to the arrival of the contact surface in this viscous calculation (labelled VCS in Fig. 4-16), and it is evidently responsible for the reduction in heat flux. The arrival of the contact surface in the inviscid case (labelled ICS in Fig. 4-16) is shown for comparison purpose only.
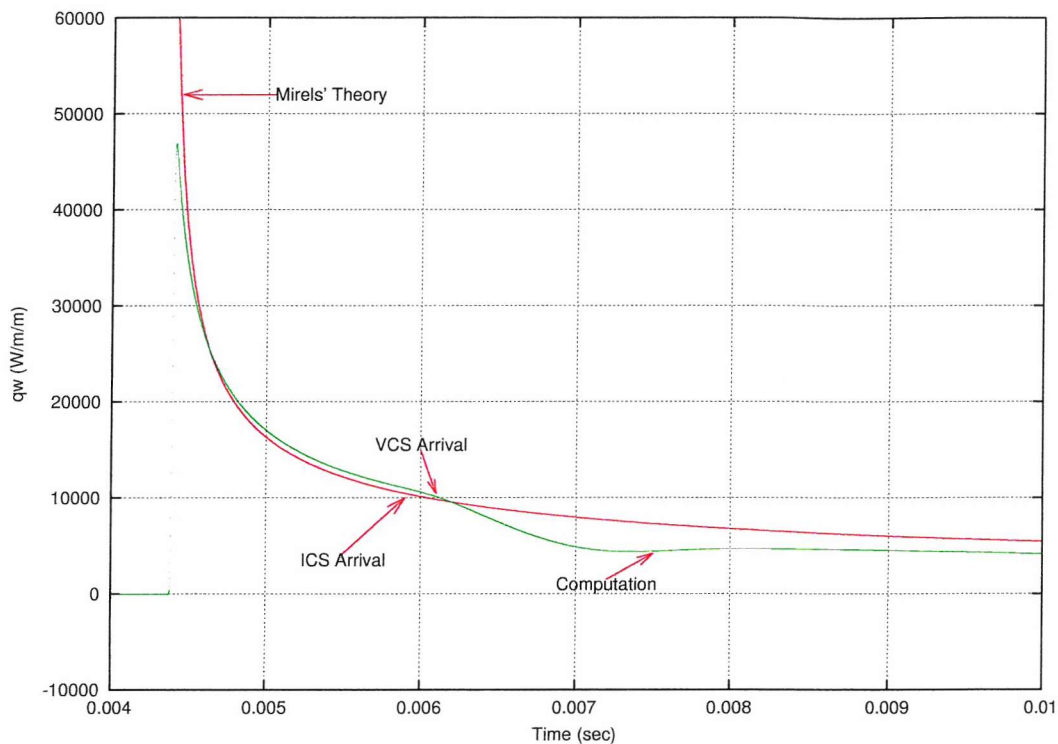


Fig. 4-16 Comparison of the heat transfer rate with prediction of Mirels' theory
and the computed heat transfer rate at x = 5.85 *m*

## 4.2.4.2 Test time

In the previous section, the separation distance between the shock and the contact surface appears to be shorter than the ideal separation distance ($l_{max}$). Hence, the test time, which is the difference in time between the arrival of the shock and the arrival of the contact surface at a fixed location, is reduced. Many researchers [8, 9, 19, 29, 30, 38, 39] have investigated this phenomenon. This quantity will be discussed here.

For an ideal 'straight-through' shock tube, the analytical solution gives a way to calculate the test time of the flow. Assuming the post-shock flow is uniform, the test time $t_S$ of the uniform flow at the end location of the tube can be given by

$$t_S = \frac{l}{u_3}$$ (4.19)

where

$$l = L\left(1 - \frac{u_3}{U_S}\right)$$ (4.20)

and $L$ is the tube length between the primary diaphragm and the end of the tube. Computed test times of the simulations are shown in Table 3. This shows that the computed test time of the viscous flow appears to be shorter than the others and is only half of the analytical test time. The reasons causing the shorter test time are deceleration of the shock and acceleration of the contact surface due to viscous effects. This is consistent with the description of viscous effects provided by Mirels [26, 28]. The 1-D inviscid results are also shorter than the analytical solution due to numerical diffusion associated with the contact surface.

Table 3. Comparison of the computed test time and the analytical test time

| | Analytical solution | 1-D inviscid simulation | 2-D viscous simulation |
|---|---|---|---|
| Coarse grid (N=1170 for 1-D) | 2.21 *ms* | 1.78 *ms* | 1.01 *ms* |
| Middle gird (N=1755 for 1-D) | 2.21 *ms* | 1.86 *ms* | 1.07 *ms* |
| Fine grid (N=2340 for 1-D) | 2.21 *ms* | 1.90 *ms* | 1.10 *ms* |

## 4.3 Shock Tube with End Wall

This section will discuss the tailored interface technique used widely in shock tube research because of the possibility to achieve longer test time. Some researchers [7, 16, 19, 23, 49] have carried out some important studies of the tailored interface technique.

In Fig. 4-17 an ideal procedure scheme of the reflected shock tube is shown. Davies [7] has given a clear description of the tailored interface technique. The region 5 behind the reflected shock is used for studying high temperature chemical reaction phenomena [12, 13] or providing a hot test gas reservoir for expansion to hypervelocity in a nozzle of a reflected shock tunnel. The test time is usually limited by disturbances originating from the interaction of the reflected shock with the contact surface. When the reflected shock travels back to interact with the contact surface, the shock passing through the contact surface gives rise to either an expansion wave or a shock wave as the reflected disturbance that travels from the point of interaction towards the end wall as shown in Fig. 4-18 (a) and Fig. 4-18 (b). They are known as "under-tailored" and "over-tailored", respectively. With tailored condition, the contact surface is ideally brought to rest and only an infinitely weak disturbance (a Mach wave) is propagated toward the end wall shown in Fig. 4-18 (c). As will be demonstrated later, this condition corresponds to a situation where the same speed in the shock-heated test gas matches that in the expanded driver gas, i.e. the same speed ratio across the contact surface ($a_2/a_3$) is unity. This condition is achieved by appropriate adjustments of the driver/driven gas temperatures and pressures. Even though these ideal conditions are rarely achieved in practice, operation at near tailored-interface condition can greatly extend the useful run time of reflected shock facilities.

### 4.3.1 Analysis of Tailoring Conditions

For achieving the performance of the tailored condition, the analysis suggests that the first reflected disturbance (Mach wave) propagated from the contact surface is weak enough to be tailored in a specific range of Mach number of the primary
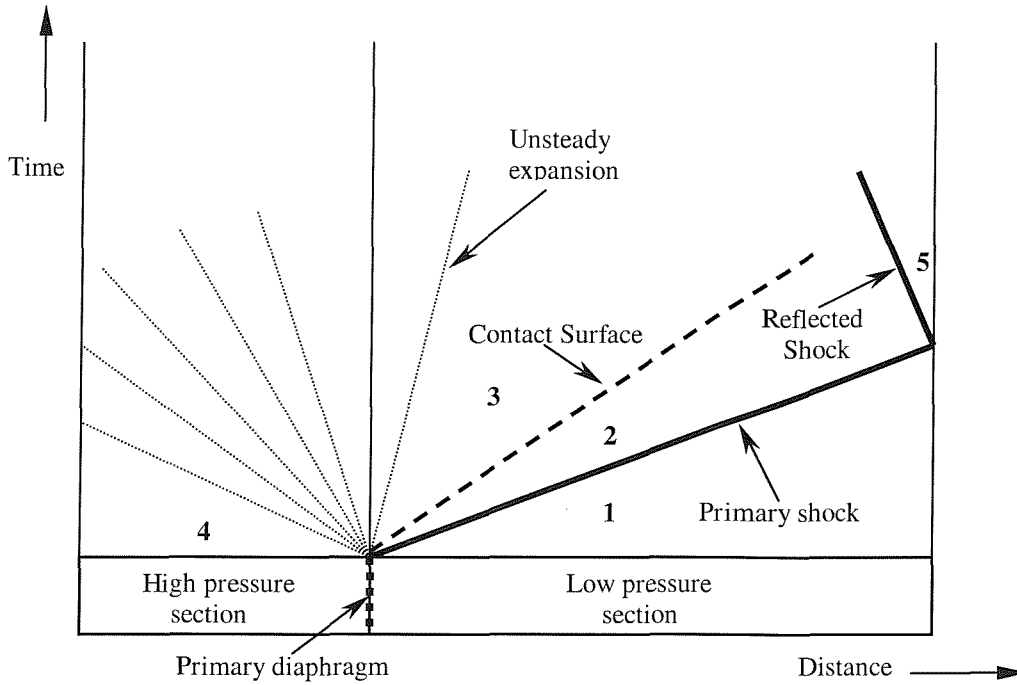
Fig. 4-17 The ideal scheme of shock tube (Davies, 1965)
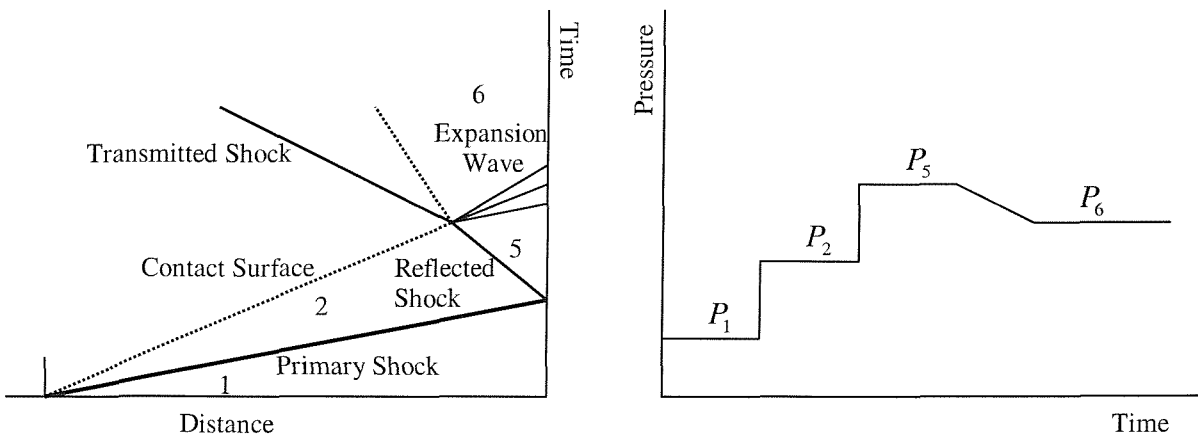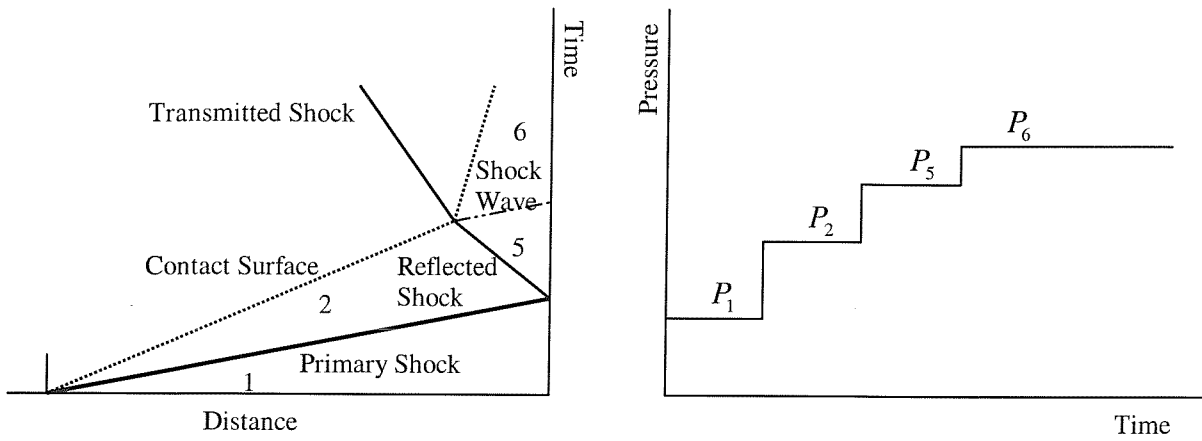
(a) Under-tailored condition



Fig. 4-18 (a) Wave diagrams and pressure profiles for under-tailored conditions

(b) Over-tailored condition
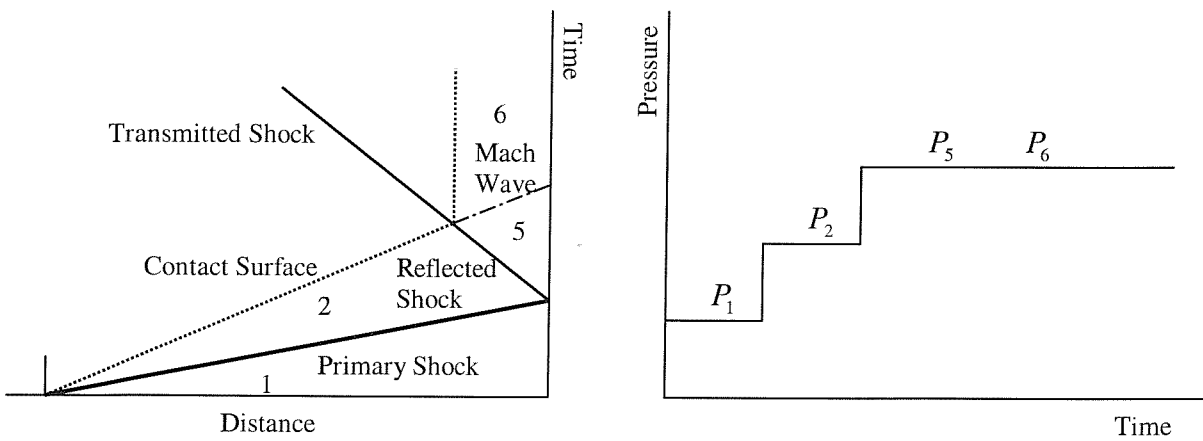


(c) Tailored condition



Fig. 4-18 (b) and (c) Wave diagrams and pressure profiles for over-tailored and tailored conditions

shock. Therefore, the strength of the reflected shock is equal to the strength of the transmitted shock, so that the Mach number behind the primary shock is equal to the Mach number behind the contact surface.

Since the velocities on the two sides of the contact surface are equal, then the speeds of sound on the two sides of the contact surface must also be equal for this condition to be satisfied. A theoretical analysis of tailoring conditions is given by Holder and Schultz [19] below.

Assume $\gamma_4 = \gamma_1$, the relationship between the pressure ratio $P_{21}$ across the primary shock and the initial pressure ratio $P_{41}$ across the diaphragm can be expressed as:

$$P_{41} = P_{21}\left[1 - (P_{21} - 1)a_{14}\left(\frac{\beta}{\alpha P_{21} + 1}\right)^{\frac{1}{2}}\right]^{-\frac{1}{\beta}} \qquad (4.19)$$

where $\alpha = \dfrac{\gamma + 1}{\gamma - 1}$, $\beta = \dfrac{\gamma - 1}{2\gamma}$ and $a_{14} = \dfrac{a_q}{a_4}$.

The Mach number $M_S(=U_S/a_1)$ of the primary shock related to $P_{21}$ can be expressed as:

$$M_S = \sqrt{\beta(\alpha P_{21} + 1)} \qquad (4.20)$$

The speed of sound $a_2$ in the region of the gas behind the shock can be given by

$$a_2 = a_1\left[\frac{P_{21}(P_{21} + \alpha)}{\alpha P_{21} + 1}\right]^{\frac{1}{2}} \qquad (4.21)$$

The speed of sound $a_3$ behind the contact surface can be given by

$$a_3 = a_4 \left( P_{14} P_{21} \right)^\beta \qquad\qquad . \qquad\qquad (4.22)$$

Finally, the speed of sound ratio $a_{32}$ across the contact surface can be given by combining equations (4.21) and (4.22) as

$$a_{32} = a_{41} \left( P_{14} P_{21} \right)^\beta \left| \frac{\alpha P_{21} + 1}{P_{21} \left( P_{21} + \alpha \right)} \right|^{\frac{1}{2}} \qquad\qquad (4.23)$$

The values of $a_{32}$ calculated from equation (4.23) by varying the value of $T_{41}$ are shown in Fig. 4-19 in terms of $M_S$, calculated by equations (4.19) and (4.20). The pressure ratio $P_{41}$ in terms of $M_S$ is also shown in Fig. 4-20. The results suggest that it is necessary to increase the temperature of driver gas $T_4$ for achieving the under-tailored and tailored conditions, and that it is not possible to achieve tailored conditions when $T_4 = T_1$ except for the trivial case when $M_S = 1$.
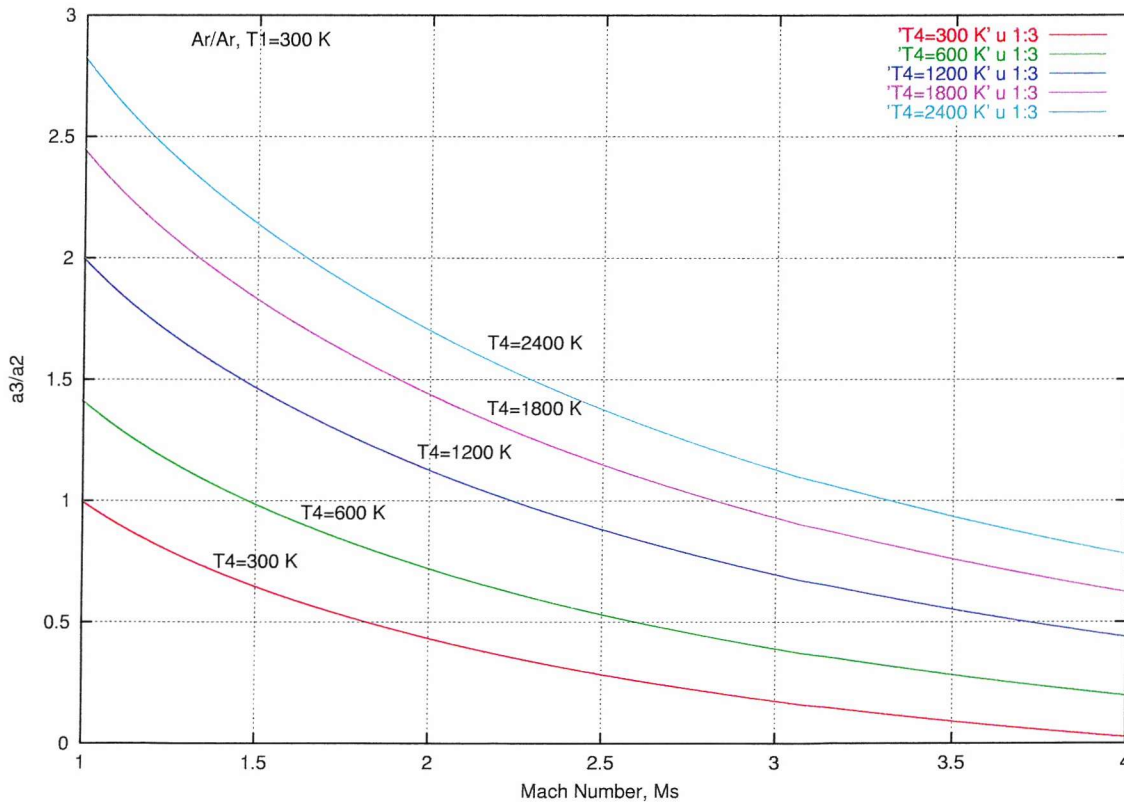


Fig. 4-19 Values of $a_{32}$ in terms of $M_S$
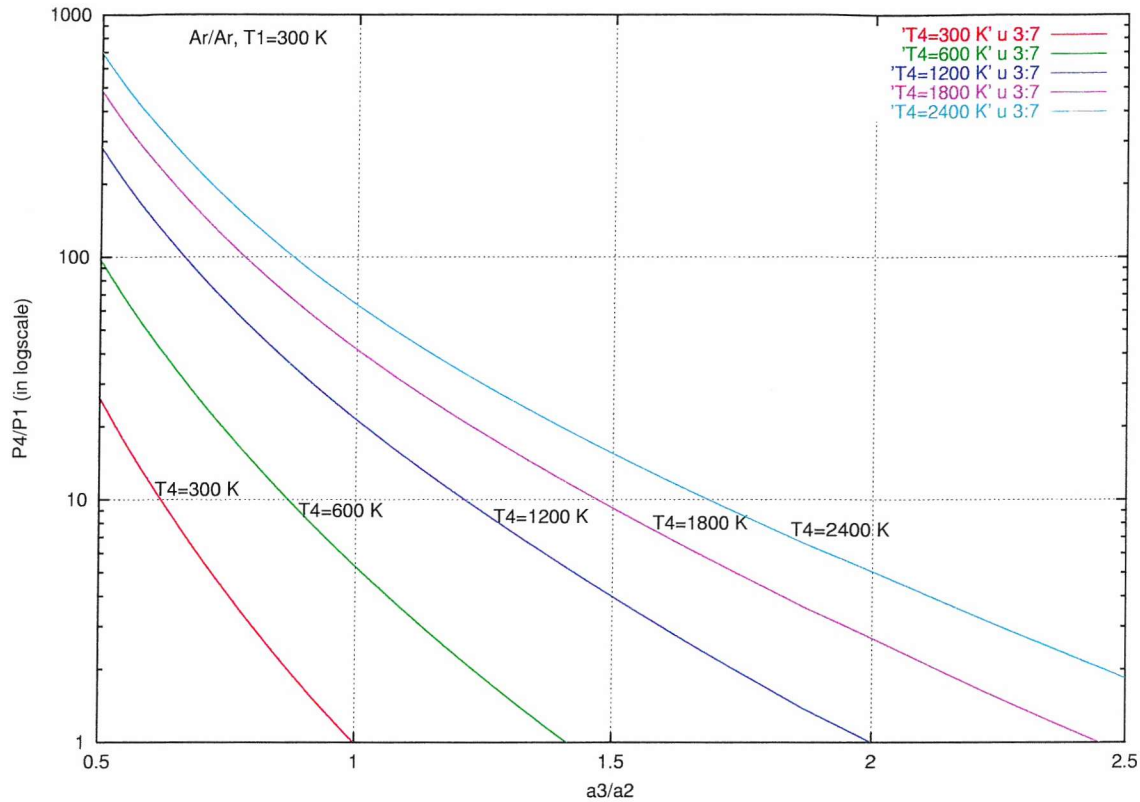
Fig. 4-20 The pressure ratio $P_{41}$ in terms of $a_{32}$

## 4.3.2 Numerical Simulations

From the analysis above, the values of $T_{41}$ and $P_{41}$ in terms of $M_S$ for $a_{32} = 1$ can be found in Table 4. For simplicity, the value of $T_{41}$ is considered to be 4 ($a_{41} = 2 = \sqrt{T_{41}}$) and $P_{41} = 21.4$ is chosen to run the tailored inviscid simulations for $M_S = 2.24$ shown in Fig. 4-21 and Fig. 4-22. And $P_{41} = 10$ and 50 are chosen to be the conditions of the under-tailored and over-tailored cases for $M_S < 2.24$ and $M_S > 2.24$, respectively. For comparison with the tailored inviscid simulations, a tailored viscous simulation is suggested to run with the same tailored condition shown in Fig. 4-27. The computations were performed by the HLLC Riemann solver without MUSCL slope limiter. The number of uniformly

spaced grid points used in all the simulations is N = 2340 on $x$-axis and N = 70 on $r$-axis.

Table 4. The values of $T_{41}$ and $P_{41}$ in terms of $M_S$ for $a_{32} = 1$

| | $T_4 = 300K$ | $T_4 = 600K$ | $T_4 = 1200K$ | $T_4 = 1800K$ | $T_4 = 2400K$ |
|---|---|---|---|---|---|
| $M_S$ | 1.00 | 1.48 | 2.24 | 2.83 | 3.32 |
| $P_{41}$ | 1.00 | 5.29 | 21.4 | 41.77 | 63.68 |

## 4.3.2.1 Inviscid Flow Cases

Fig. 4-21 shows that reflected shock (RS) passes through inviscid contact surface (ICS) to become a transmitted shock (TS) without any significant change in speed when $M_S$ = 2.24. The transmitted shock is later accelerated by arrival of reflected expansion (RE) from the end wall of driver chamber. It also shows that reflected disturbance (RD) is weak although it appears to be finite. In Fig. 4-22, the computed pressure at three different locations appears to be equal after the reflected shock passes through the contact surface and reflected disturbance is very weak. It also shows that the available constant pressure test time is approximately 4 *ms* at the end wall. There are no equivalent experimental data for this condition. However, it is fairly typical for reflected shock tunnels when operating close to tailored-interface conditions, to have run durations of the order of a few milliseconds (see Roberts' Ph. D. Thesis [34]).

In Fig. 4-23, it is seen that the expansion wave is reflected from the contact surface (ICS) after the reflected shock (RS) passes through when $M_S$ < 2.24, but the contact surface is reversed as described in Fig. 4-18 (a) by Davies [7]. After the first reflected expansion (RE), the reflected disturbance (RD) can be weak, so that the pressure may be close to the equilibrium pressure. In Fig. 4-24, the computed pressure at x = 5.25 *m* appears to be constant for approximately 1 *ms* after the reflected shock arrives. It is because the speed of sound increase at the contact surface, $a_2 < a_3$, the Mach number of the shock reduces when it passes

the contact surface, hence, the reflected expansion wave is brought to restore the pressure equality.

In Fig. 4-25, for $M_S > 2.24$, the contact surface (ICS) appears to continue to travel slowly toward the end-wall, as described in Fig. 4-18 (b) by Davies [7] when the secondary reflected shock (SRS) wave is reflected from the contact surface. The first transmitted shock (FTS) wave shown in Fig. 4-25 is slower than the reflected shock (RS). In Fig. 4-26, the computed pressure at x = 5.25 $m$ shows that after the reflected shock wave, the reflected disturbances (RD) are also shocks and will be reflected from the contact surface at a later stage. Later, the third reflected shock (TRS) wave is reflected from the end wall and is strong enough to passes through the contact surface, then secondary transmitted shock (STS) is formed. At later stages, the further reflected shocks are not strong enough to pass through the contact surface and the pressure may be brought to be close to the equilibrium pressure.
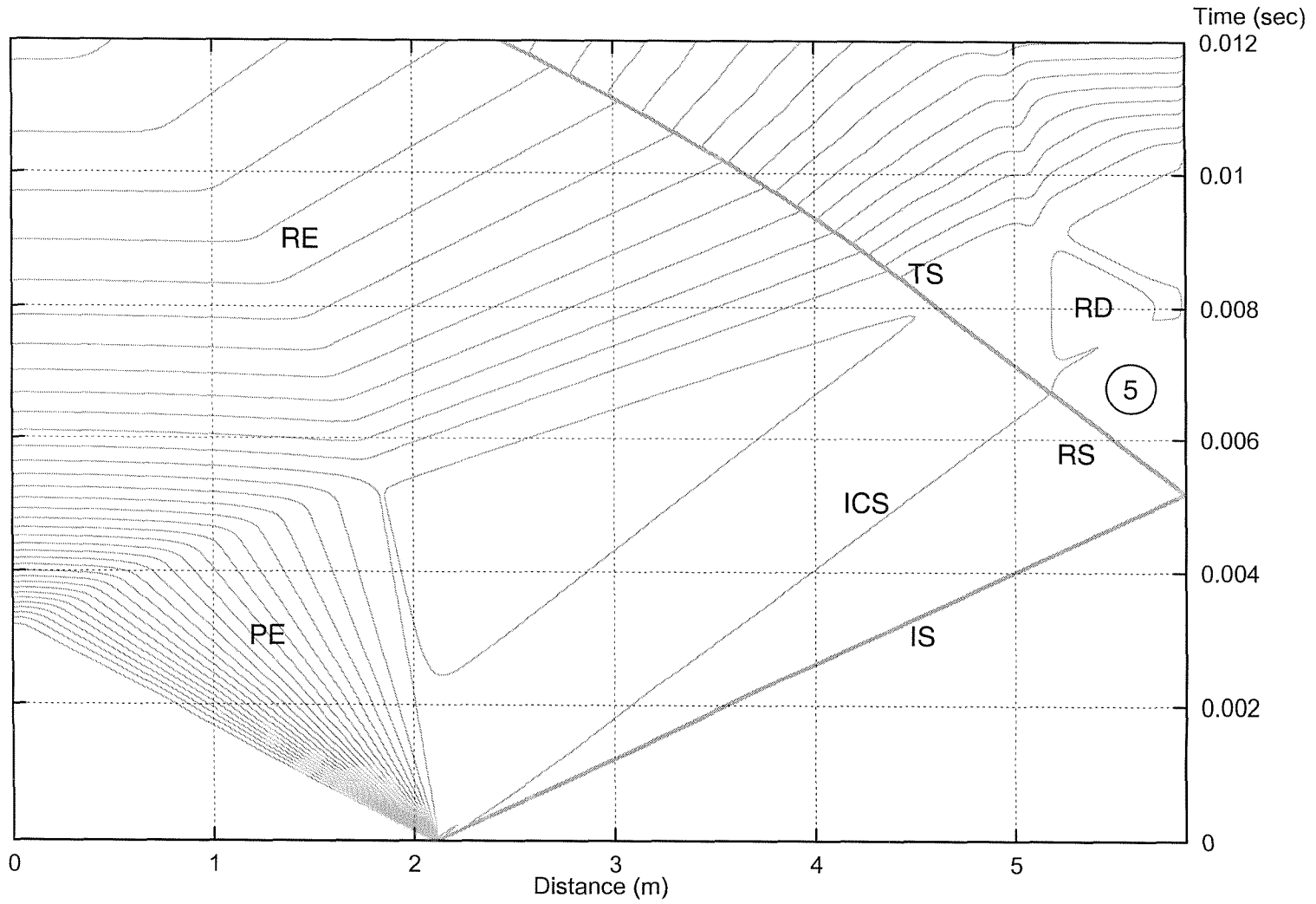
Fig. 4-21 Wave diagram of the density profile for the tailored condition
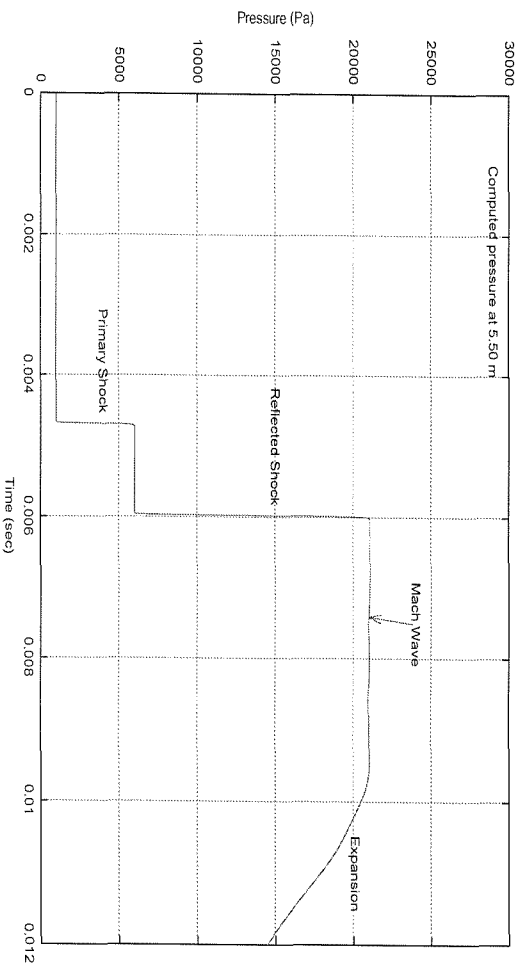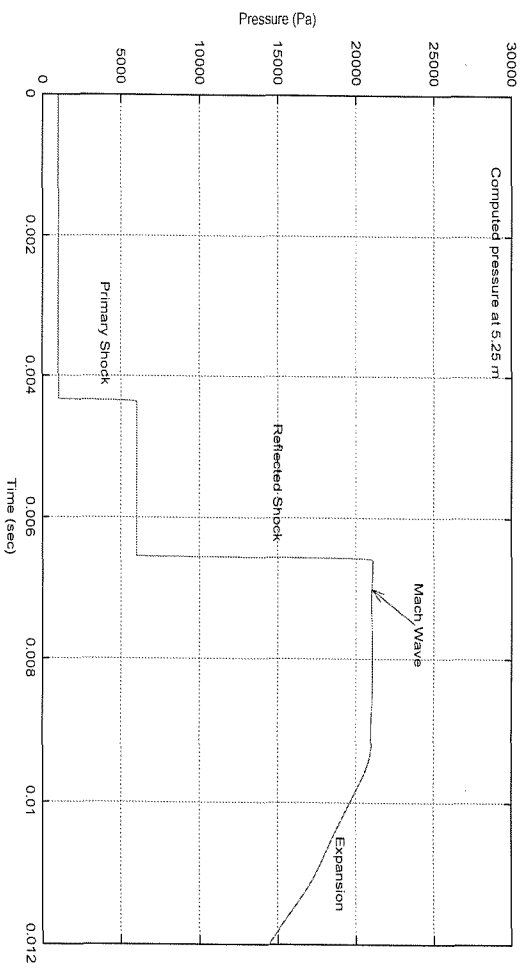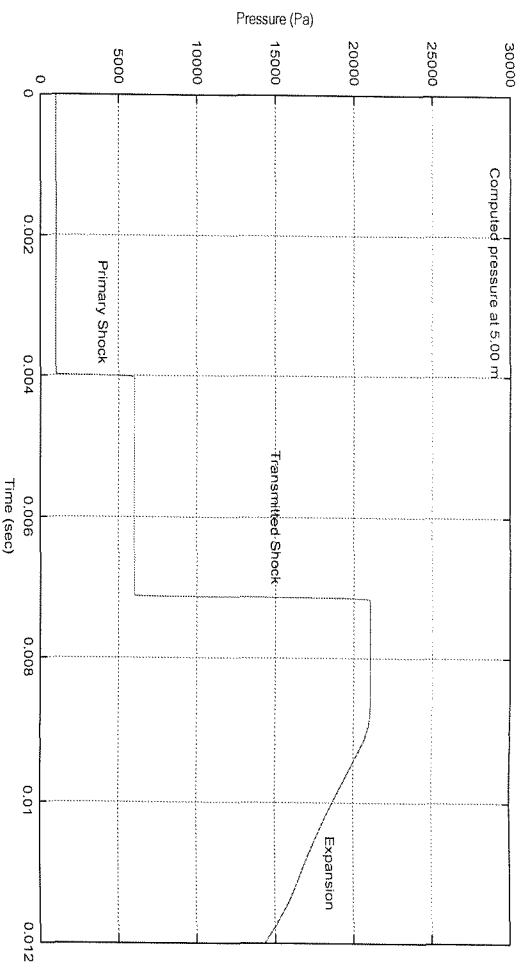
Fig. 4-22 Computed pressure at three positions for the tailored condition
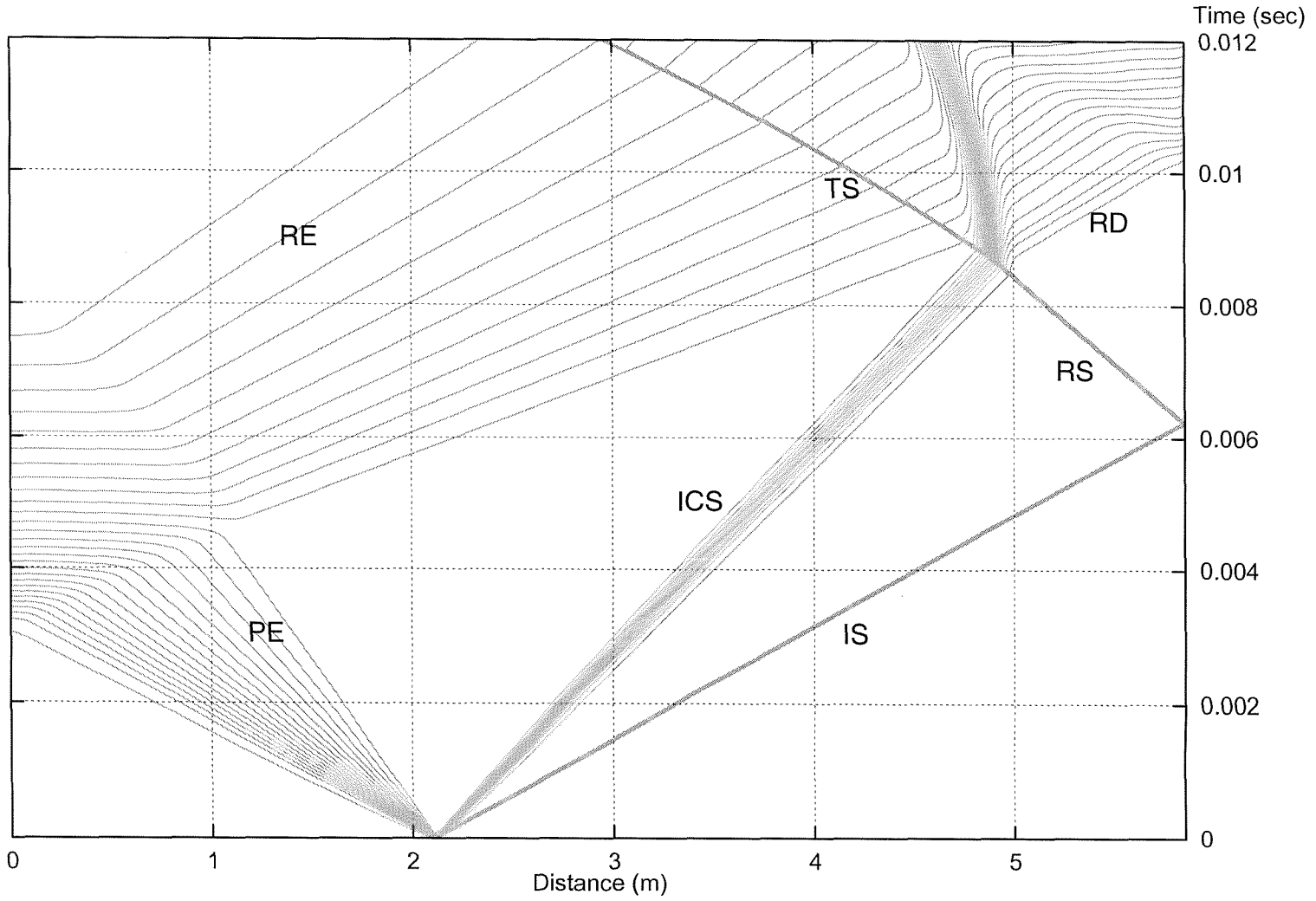
Fig. 4-23 Wave diagram of the density profile for the under-tailored condition
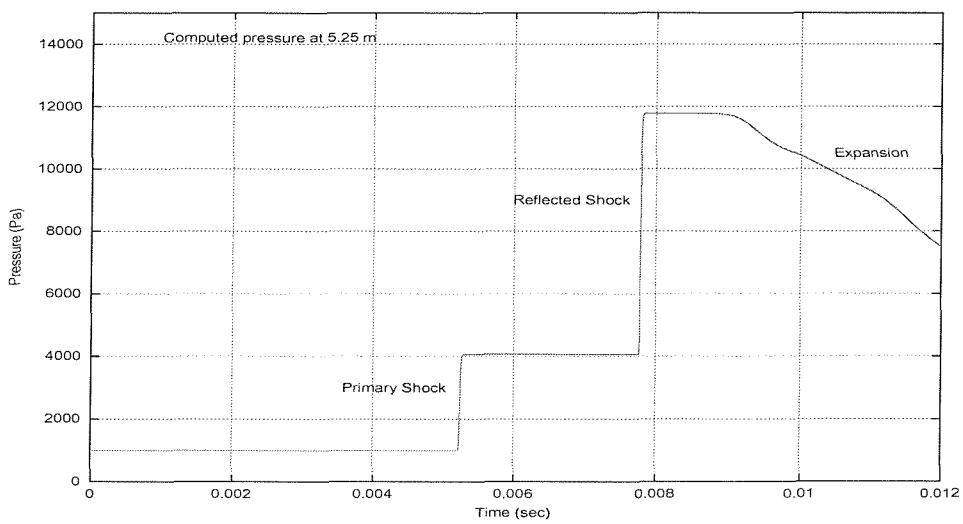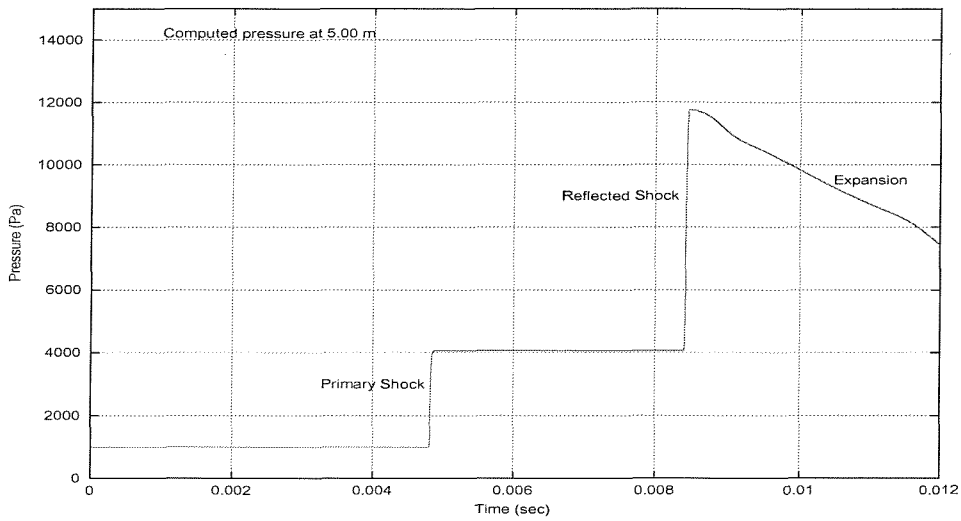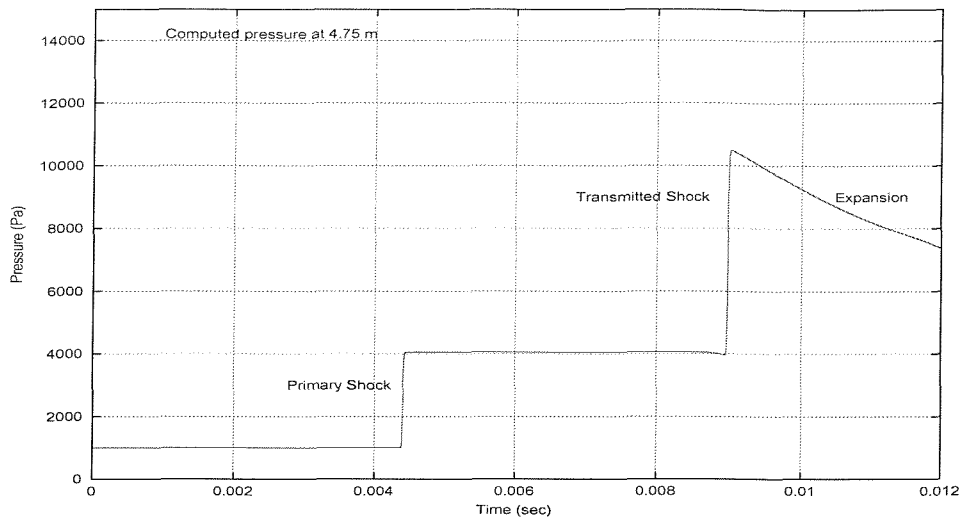
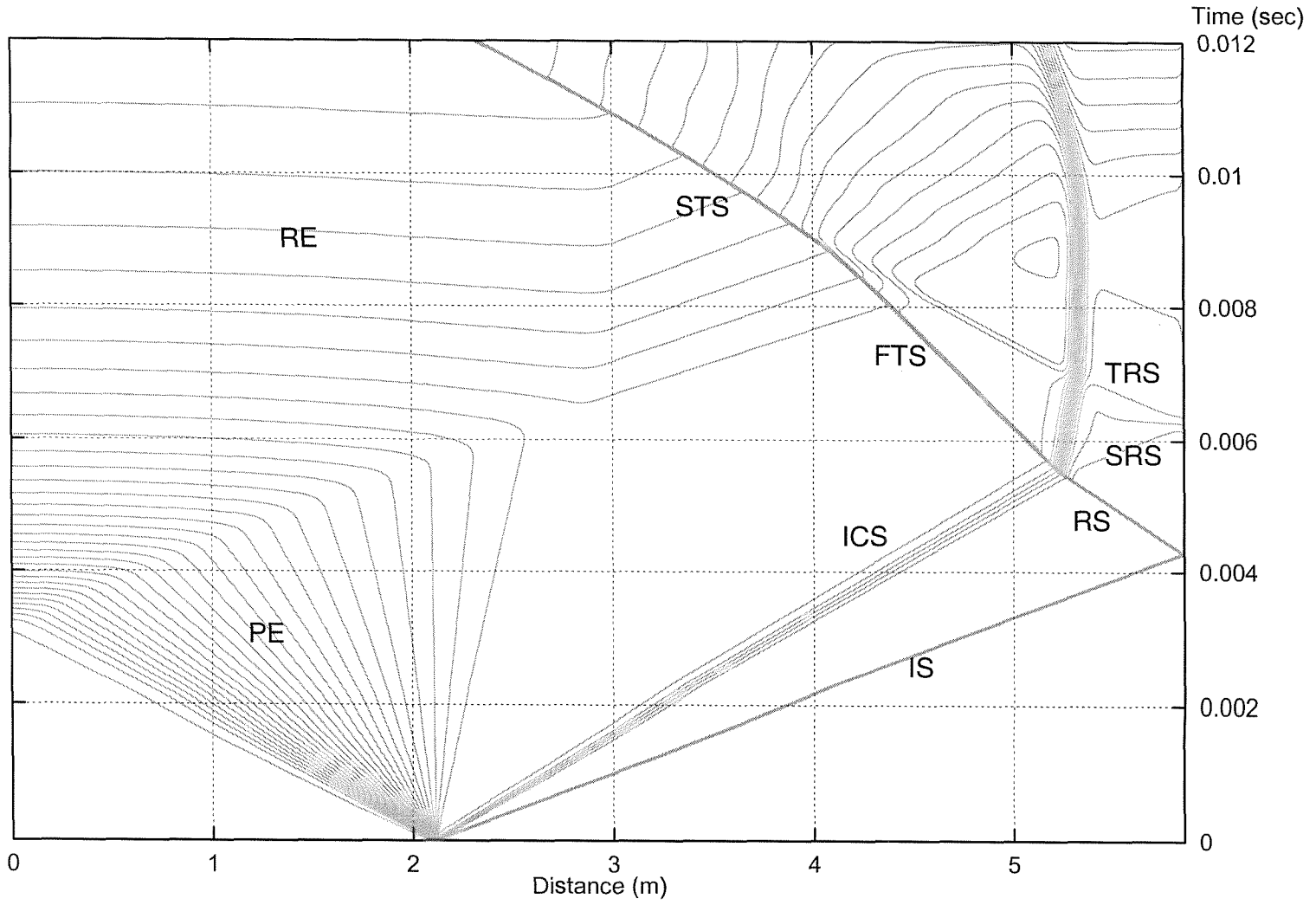Fig. 4-24 Computed pressure at three positions for the under-tailored condition

Fig. 4-25 Wave diagram of the density profile for the over-tailored condition
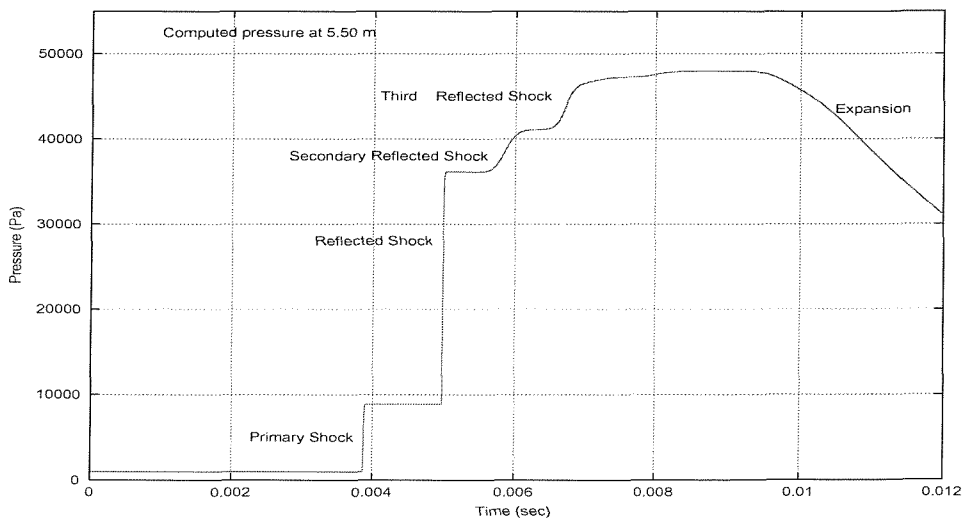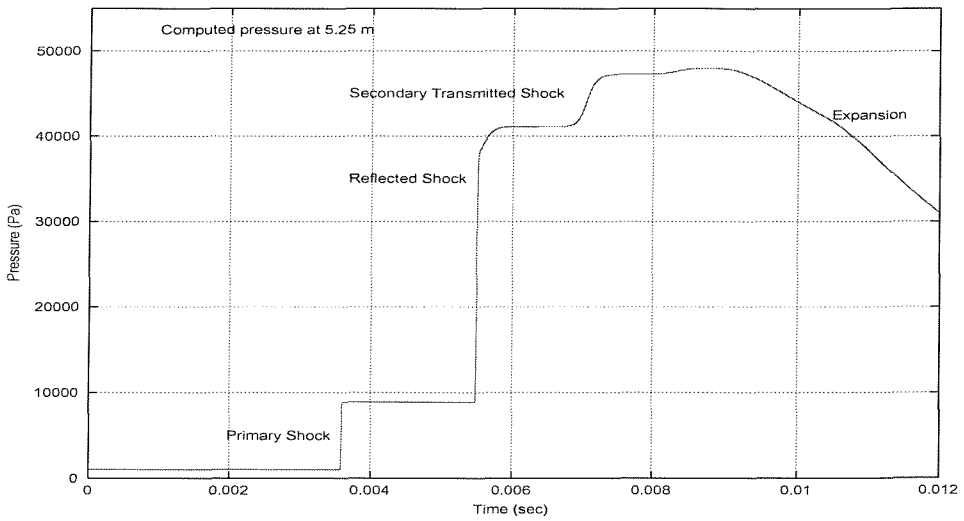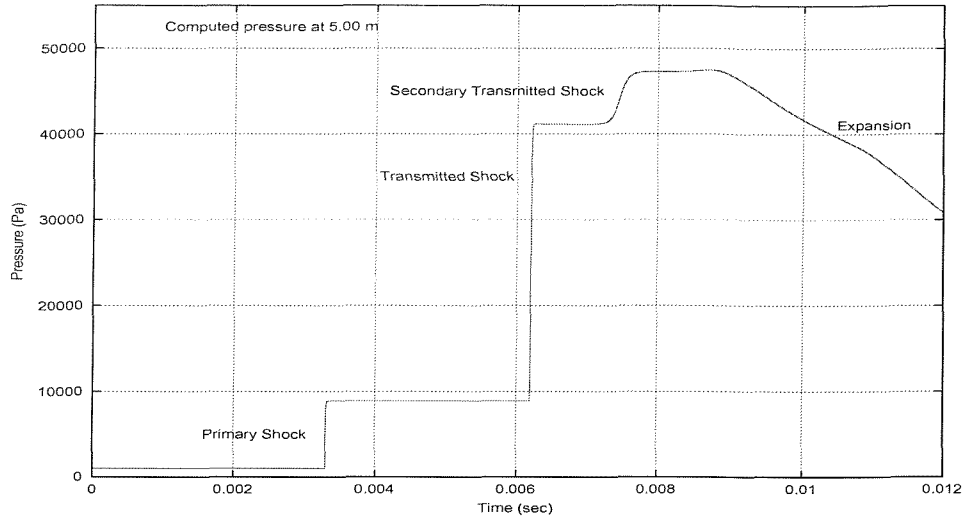
Fig. 4-26 Computed pressure at three positions for the over-tailored condition

### 4.3.2.2 Viscous Flow Cases

A viscous simulation has also been carried out for comparing to the inviscid simulation for the tailored condition. The wall temperatures of both chambers are at 300 K and are isothermal. The results of distance-time wave diagram and computed pressure at three different positions along central line are shown in Fig. 4-27 (a) and Fig. 4-27 (b), respectively. Fig. 4-27 (a) shows that the viscous shock (VS) propagates toward the end wall of the tube at the initial shock speed of 710.88 m/s, and the shock speed later decays to 552.40 m/s at the end. It also appears to be slower 23.5% than the shock speed of the inviscid flow. Then, the reflected shock (RS) is reflected from the end wall to pass through the viscous contact surface (VCS) to become a transmitted shock (TS) without any significant change in speed. Compared with the inviscid case (Fig. 4-21), the reflected disturbance (RD) is smeared out. This is also apparent in the pressure variation with time illustrated in Fig. 4-27 (b). Fig. 4-27 (a) shows that the available constant pressure test time is approximately 1.60 *ms* at x = 5.50 *m*. This compares with 4 *ms* of test time in the inviscid case. However, Fig. 4-27 (a) shows that there is an odd feature in the expansion pattern. It is suspected that there may be transverse waves occurring in the driver chamber due to the large temperature difference between the hot driver gas and the cold wall. This phenomenon is investigated further below.

### 4.3.3   The Acoustic Wave Propagation Phenomenon

Fig. 4-28 shows that a large pressure loss and some oscillation behaviours occur ahead of the arrival of the expansion wave in the driver chamber. Hence, another simulation using Helium as driver and driven gas is also carried out with the same pressure ratio and the result is shown in Fig. 4-29. In comparison with the previous results, the result appears to have larger pressure loss and oscillation behaviours due to the higher specific gas constant $c_p$ of Helium. It implies that transverse waves may exist when the temperature difference between the gas and

the wall is large. Hence, it is necessary to clarify the influence of the temperature difference in the driver chamber.
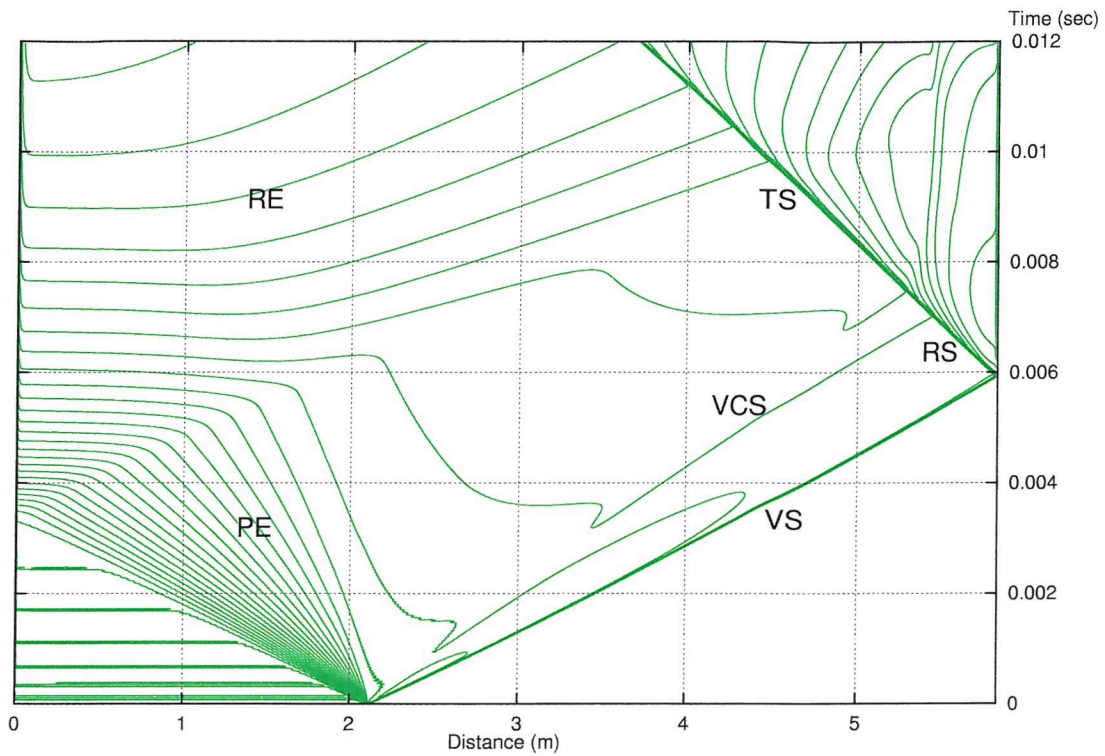


Fig. 4-27(a) Wave diagram of the viscous density profile for the tailored condition
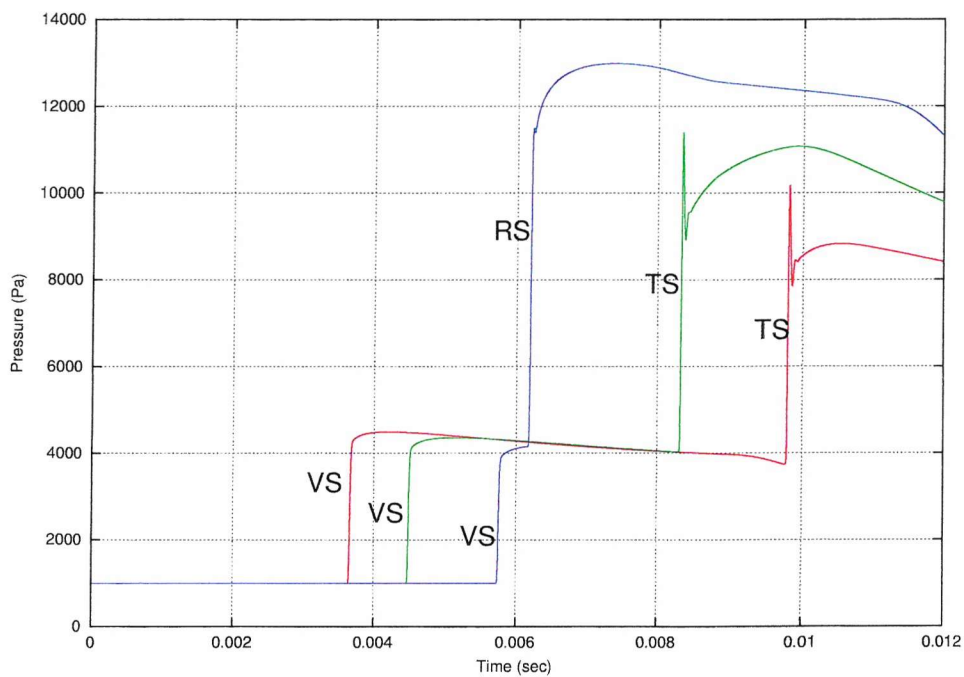


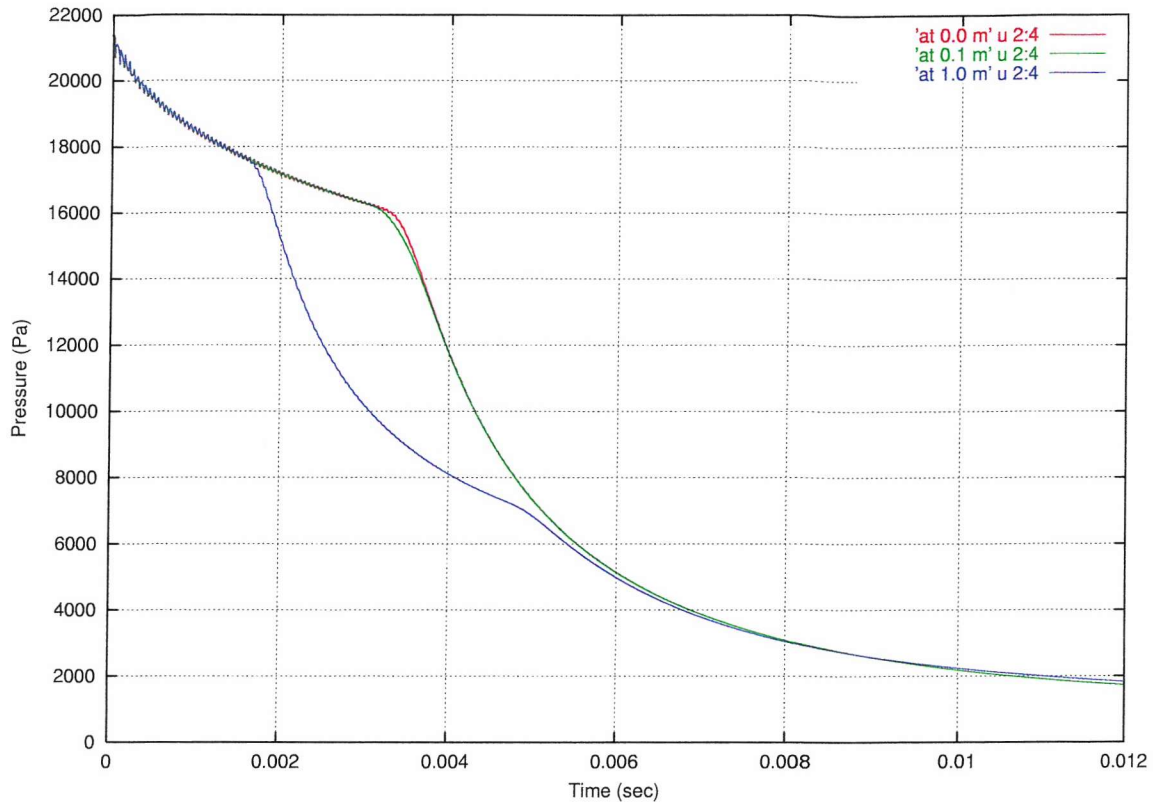Fig. 4-27 (b) Computed pressure at three positions for the tailored condition

Fig. 4-28 Computed pressure versus time for Argon using the tailored condition
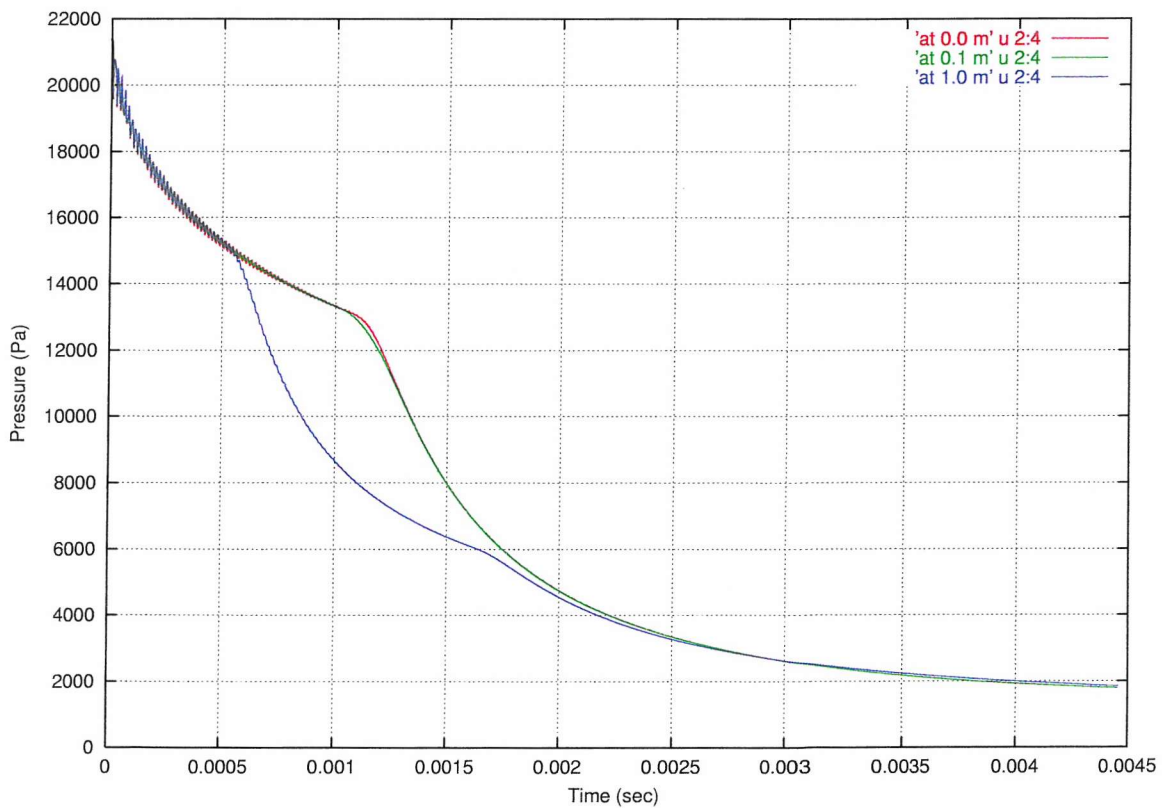at 0.0 *m*, 0.1 *m* and 1.0 *m*



Fig. 4-29 Computed pressure versus time for Helium using the same tailored condition
at 0.0 *m*, 0.1 *m* and 1.0 *m*

From the previous simulations, it may be explained that in the driver chamber some heat of the hot gas transferred into the cold wall causes the pressure near the wall to decrease. The interaction between heat transfer and pressure loss causes transverse waves to propagate from the side of the wall to the centre, even propagate across to the other side of the wall, then reflect to the side of the wall shown schematically in Fig. 4-30.
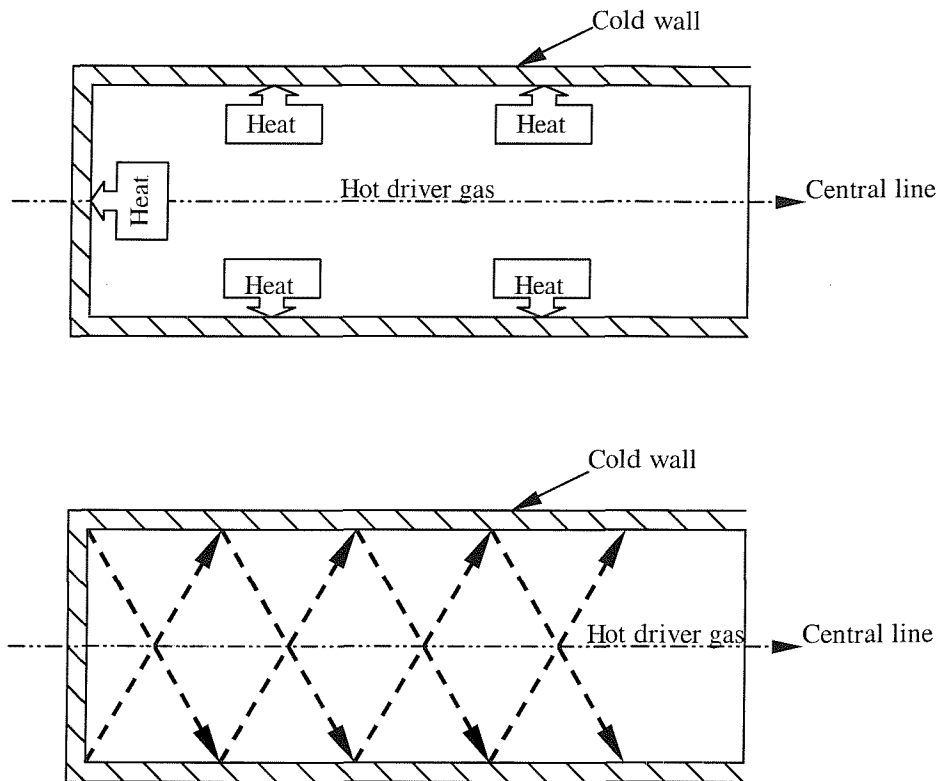


Fig. 4-30 Schematic diagram of heat transfer and transverse wave in the driver chamber

A simulation with double the diameter (D = 0.076 *m*) using the same tailored condition was carried out and the result are shown in Fig. 4-31. These indicate a smaller pressure loss and lower frequency of transverse wave propagation there compared with these shown in Fig. 4-28.

A closer look of the results obtained in Fig. 4-28 was carried out, for $0 \leq t \leq 0.0002$ *sec*, shown in Fig. 4-32. This indicates that the pressure at the centre line remains constant for approximately 24 $\mu sec$ before decreasing and becoming oscillatory in nature. The period of the subsequent oscillation is

approximately 55 $\mu sec$. This may be compared with the time taken for an acoustic wave to propagate in the gas across the tube, given by:

$$t = \frac{\Gamma}{a_g} = \frac{\Gamma}{\sqrt{\gamma RT_g}} \qquad (4.23)$$

where $\Gamma$ is the internal diameter and $a_g$ is the speed of sound of the gas. Using equation (4.23) a period of 58.8 $\mu sec$ for $\Gamma = 0.038$ $m$ and argon driver gas at $T_g$ = 1200 K is estimated. This very close to the period observed.

In Fig. 4-33 (a), the results show that the computed pressure is measured at the radius of 0.0063 $m$ ($r_1 = 1/3r$, $r = 0.019$ $m$) i.e. close to central line. The computed pressure appears to keep constant for only 16 $\mu sec$. In the meanwhile, the computed pressure measured at the radius of 0.0126 $m$ ($r_2 = 2/3r$, $r = 0.019$ $m$) i.e. close to the wall shown in Fig. 4-33 (b) appears to keep constant for 8 $\mu sec$. Since the period of initial constant pressure is shorted near the wall, this supports the view that the disturbance originates at the wall and propagates transversely at approximately this acoustic speed.

In the last analysis shown in Fig. 4-34, it shows that the contours of the velocity of $V$ vector are plotted from 0 $\mu sec$ to 48 $\mu sec$. It shows that there are transverse waves propagating from the side of the wall to central line. It also shows that there is a velocity peak at x = 2.11 $m$ due to the large temperature difference between the driver and driven gases. Hence, it may prove that the transverse waves do exist when there is the temperature difference between the gas and the wall in the driver chamber.

Since the previous analysis shows that the transverse waves exist due to the temperature difference, it is necessary to have a look at the influence of the temperature difference on the quality of the driver gas. So that two further analysis which the driver gas is at the temperature of 600 K and 2400 K are also carried

out with the same pressure ratio $P_{41}$ = 21.4 shown in Table 4. The results are shown in Fig. 4-35 and Fig. 4-36.

In Fig. 4-35 (a), it shows that the computed pressure at 600 K appears to have some larger oscillation behaviors and loss approximate 9.4% of the initial pressure at x = 1.0 *m*. In Fig. 4-35 (b), it also shows that the computed pressure at 2400 K appears to have some small oscillation behaviors and loss approximate 31% of its initial pressure at x = 1.0 *m*. In contrast, the computed pressure at 1200 K appears to have some middle level of oscillation behaviors and loss approximate 17.5% of the initial pressure at x = 1.0 *m* ( $P_4$ = 21400 Pa at 1200 K).

Fig. 4-36 shows that the computed pressure at central line with a time range of 200 $\mu sec$ keep constant for approximate 33 $\mu sec$ at 600 K and 17 $\mu sec$ at 2400 K, respectively, suggesting that the disturbance wave speed is higher at the higher temperature. The calculations for the period of transverse wave propagation are 83.3 $\mu sec$ at 600 K and 41.7 $\mu sec$ at 2400 K. However, the results indicate that the period is 76 $\mu sec$ at 600 K and 38 $\mu sec$ at 2400 K.

Fig. 4-36 shows that the period of oscillation is approximately proportional to $1/\sqrt{T_g}$ and further supports the hypothesis that a transverse wave propagates at approximate acoustic speed.

Fig. 4-37 also shows the computed pressure versus time with three temperatures at two locations of x = 0.0 *m* and x = 1.0 *m* for comparison. It appears that the duration for pressure loss decreases as the temperature of driver gas increases.

In short, all the evidence obtained suggests that the transverse wave propagation exists in the driver chamber due to heat transfer effect. The influence of the temperature difference may be necessary to consider taking into account for avoiding larger pressure loss and oscillation behaviors.

Although the hot driver gas/cool wall situation has been created artificially to investigate tailored interface operation, the results obtained (showing the

propagation of transverse waves) may be applicable and important in experiments facilities where the driver gas is heated impulsively (e.g. detonation-driven shock tubes) [52].
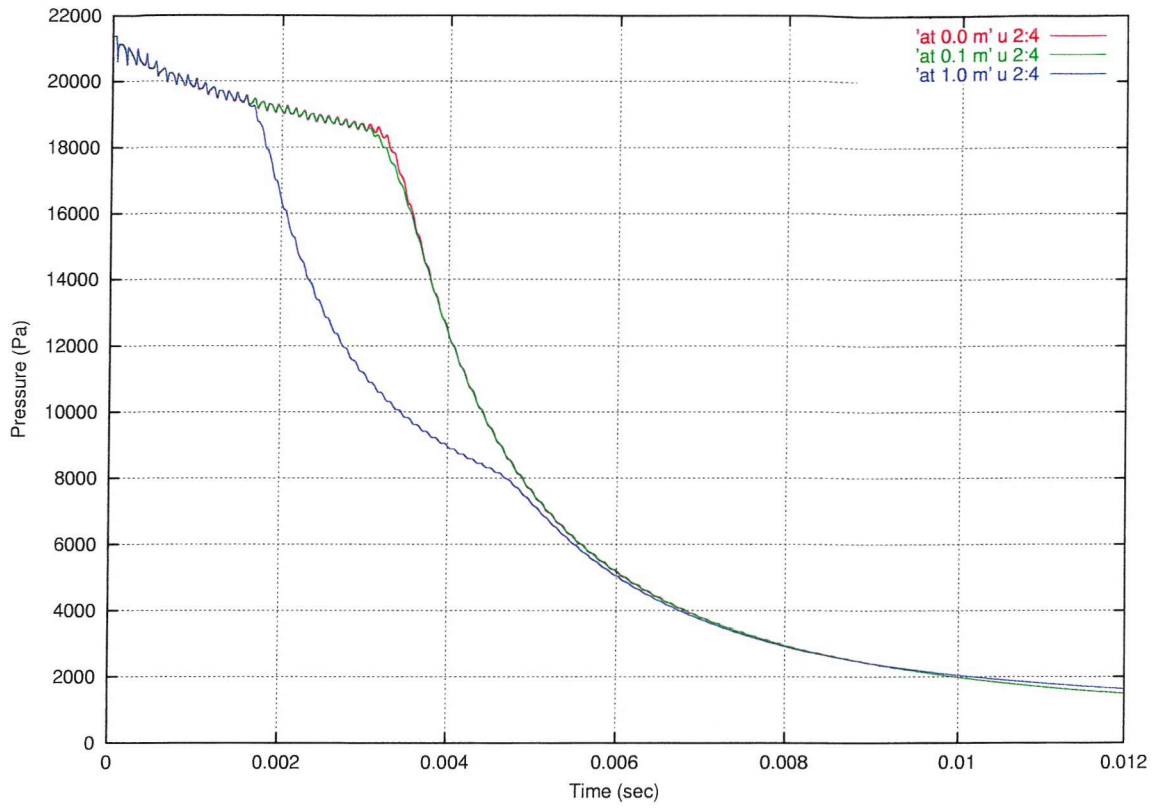
Fig. 4-31 Computed pressure versus time for Argon with double diameter
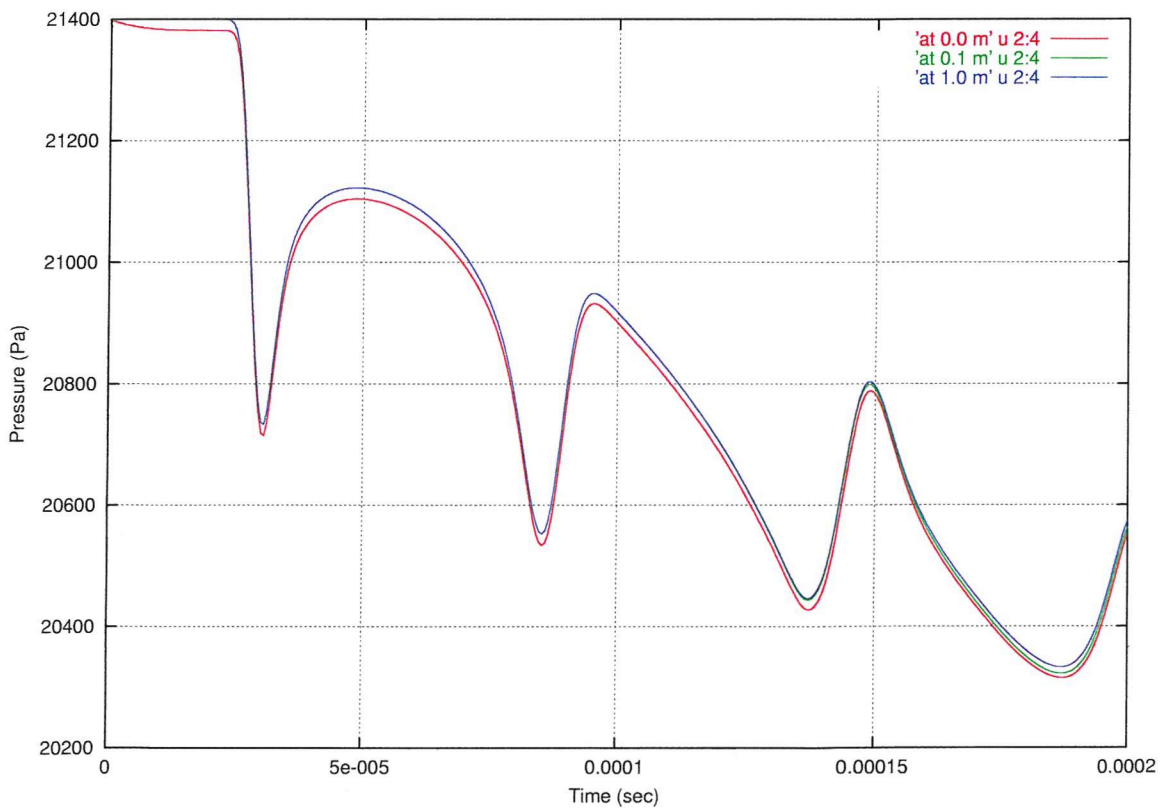using the same tailored condition at x = 0.0 *m*, x = 0.1 *m* and x = 1.0 *m*



Fig. 4-32 Computed pressure versus time for Argon at 1200 K along central line
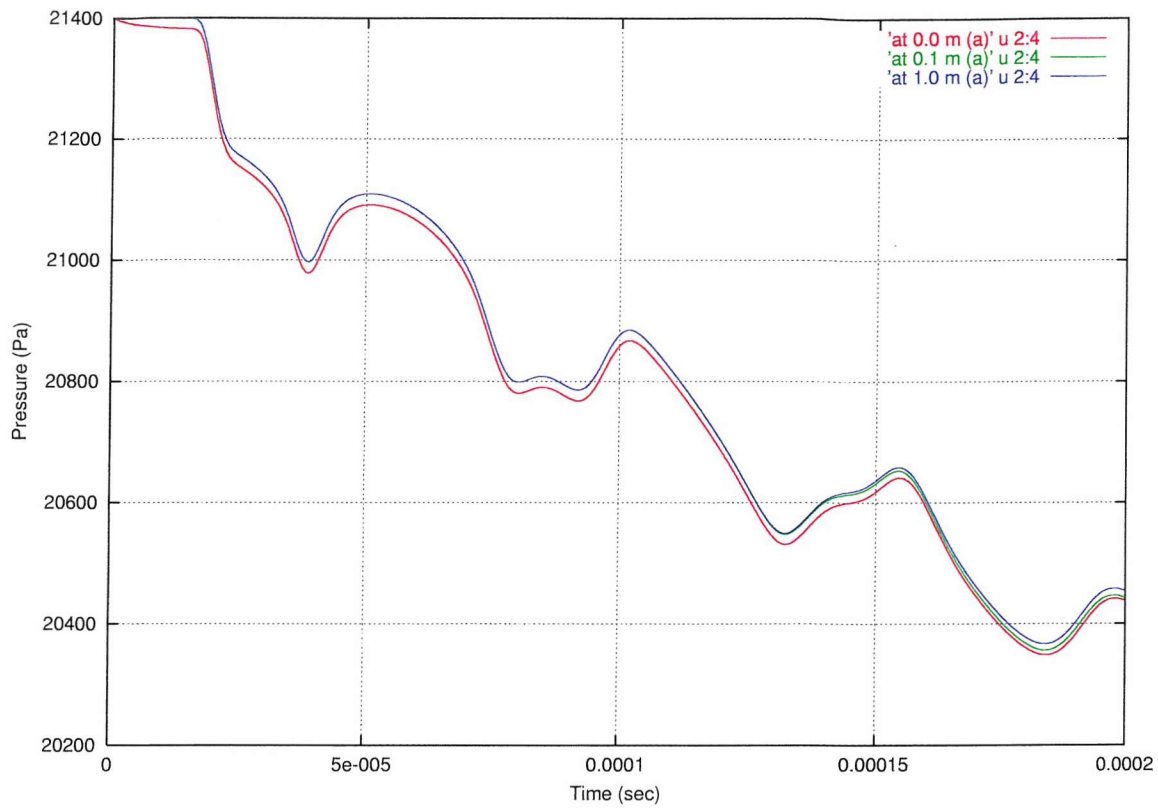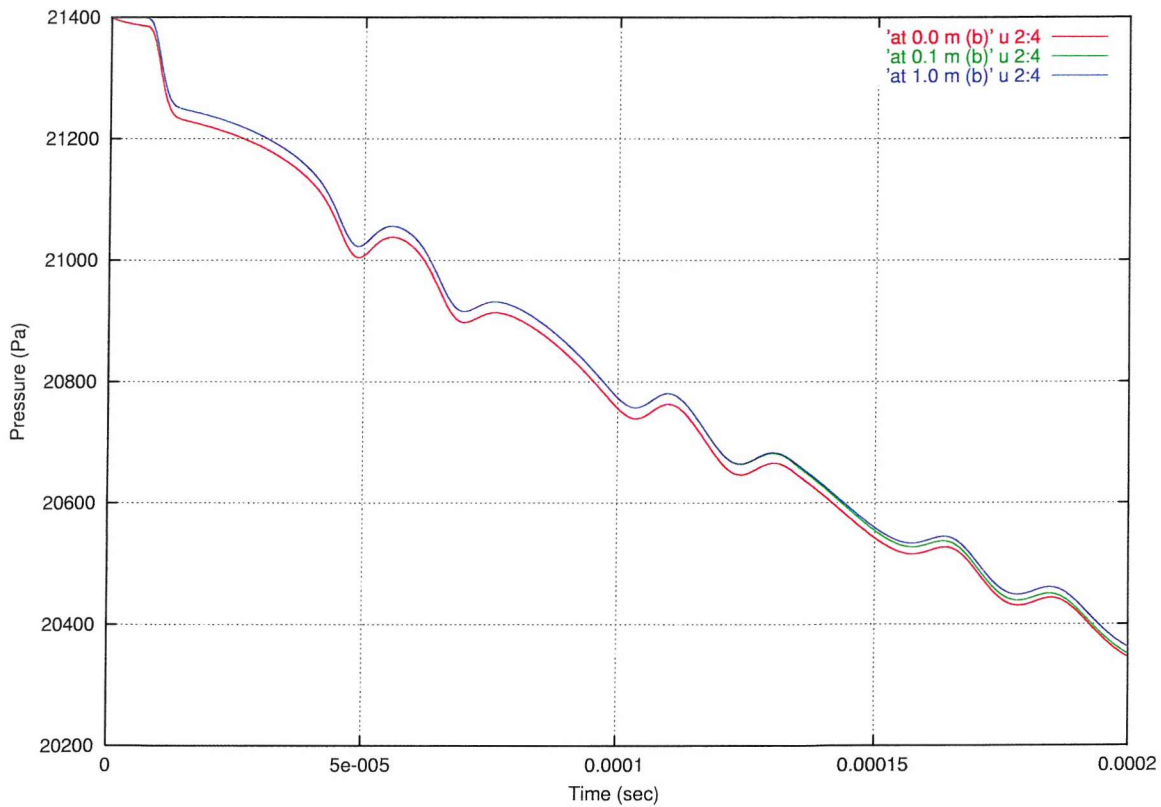at x = 0.0 *m*, x = 0.1 *m* and x = 1.0 *m*

Fig. 4-33 (a) Computed pressure versus time for Argon at 1200 K at the radius of 0.0063 *m*
at x = 0.0 *m*, x = 0.1 *m* and x = 1.0 *m*
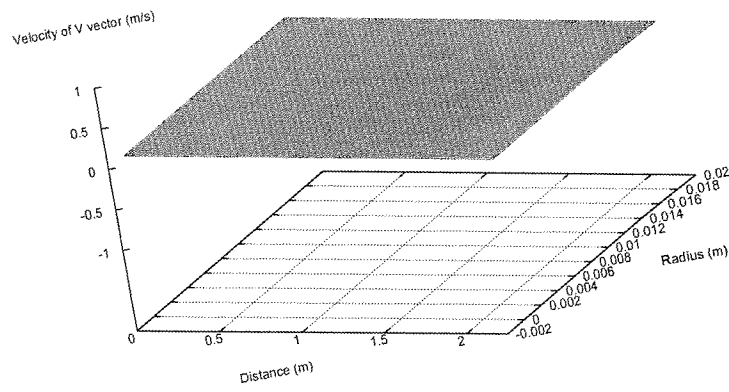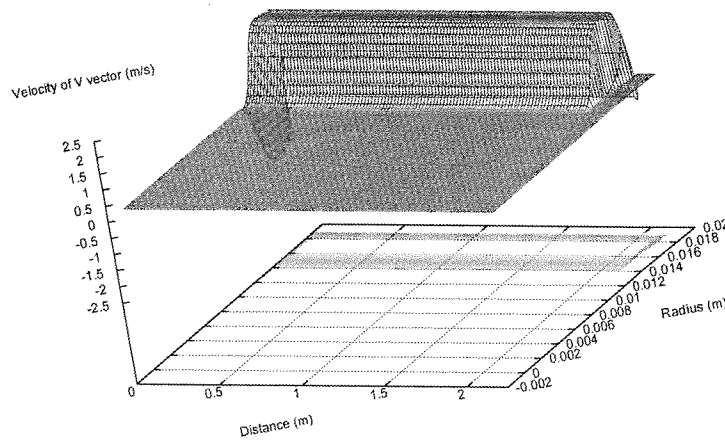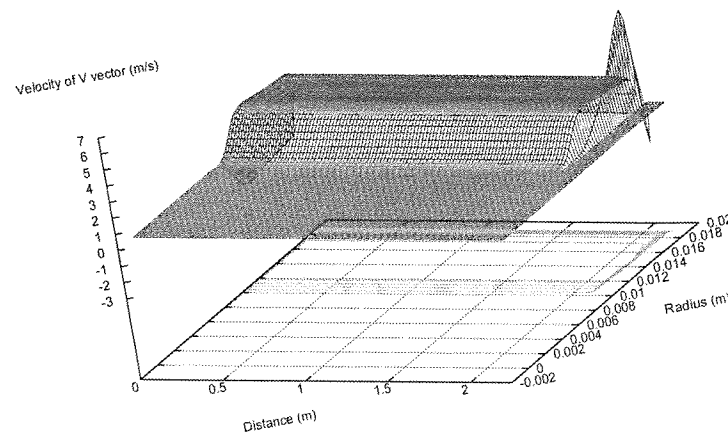


Fig. 4-33 (b) Computed pressure versus time for Argon at 1200 K at the radius of 0.00126 *m*
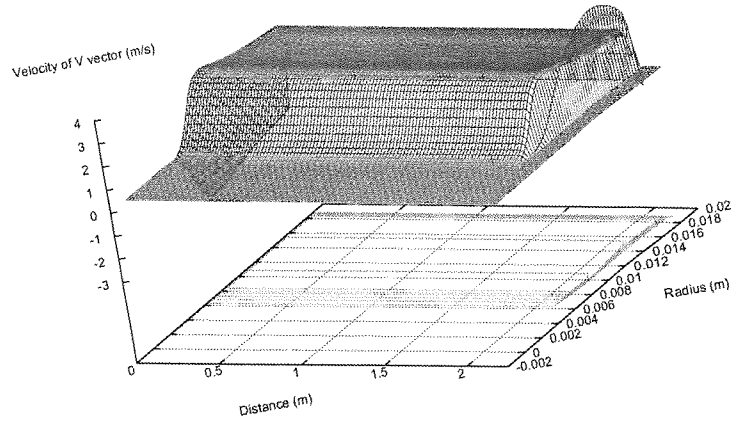at x = 0.0 *m*, x = 0.1 *m* and x = 1.0 *m*

At 0 $\mu\,sec$



At 6 $\mu\,sec$



At 12 $\mu\,sec$

Fig. 4-34 (a) The contour of the velocity of V vector from 0 $\mu\,sec$ to 12 $\mu\,sec$

89

At 18 $\mu sec$
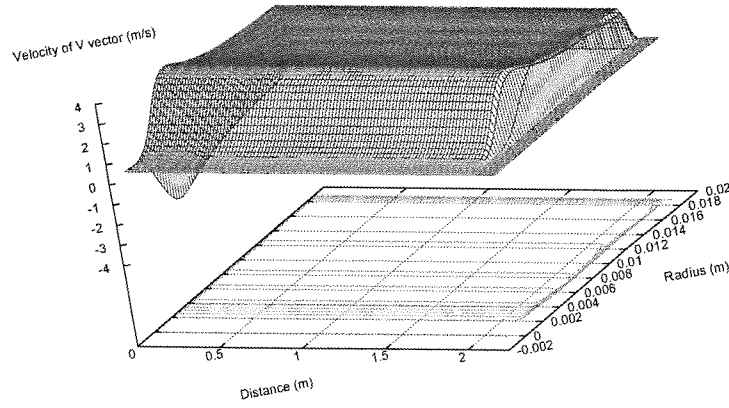


At 24 $\mu sec$
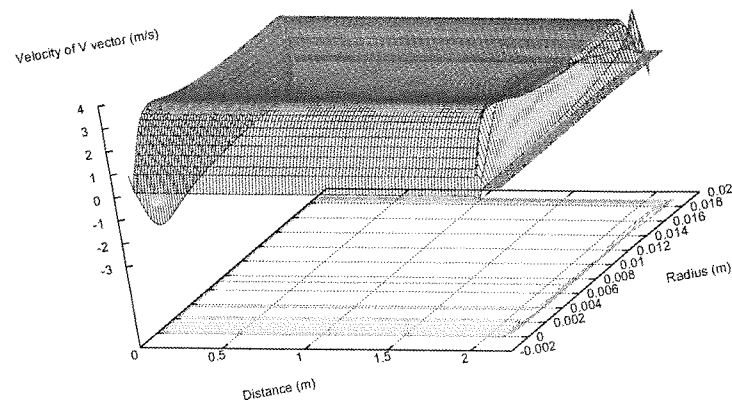


At 30 $\mu sec$

Fig. 4-34 (b) The contour of the velocity of $V$ vector from 18 $\mu sec$ to 30 $\mu sec$

90
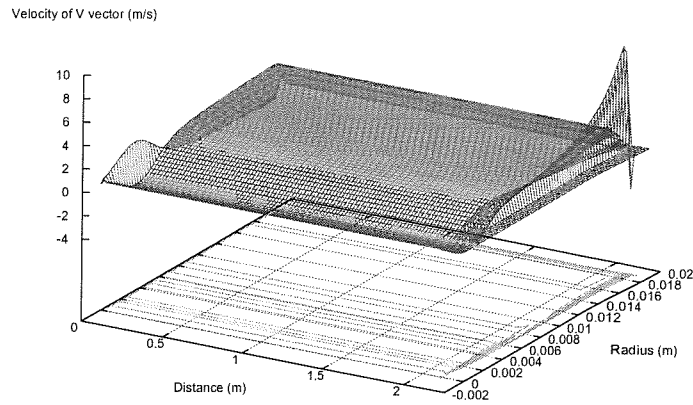
At 36 $\mu\,sec$
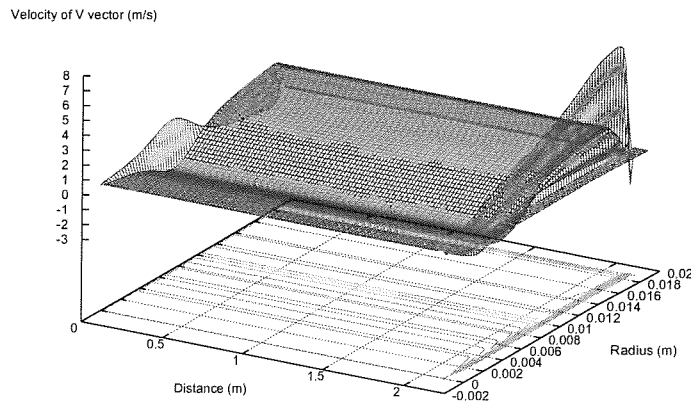


At 42 $\mu\,sec$
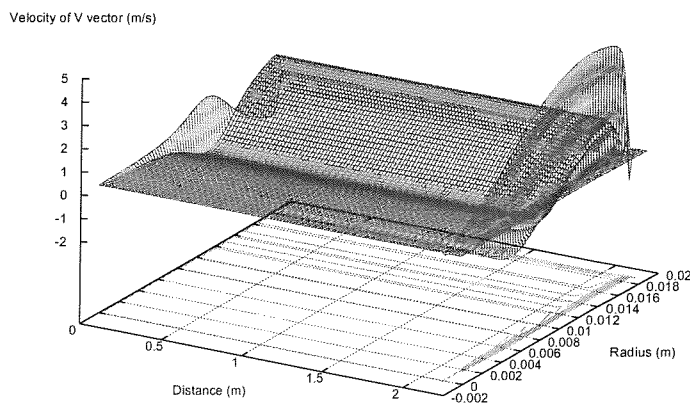


At 48 $\mu\,sec$

Fig. 4-34 (c) The contour of the velocity of $V$ vector from 36 $\mu\,sec$ to 48 $\mu\,sec$
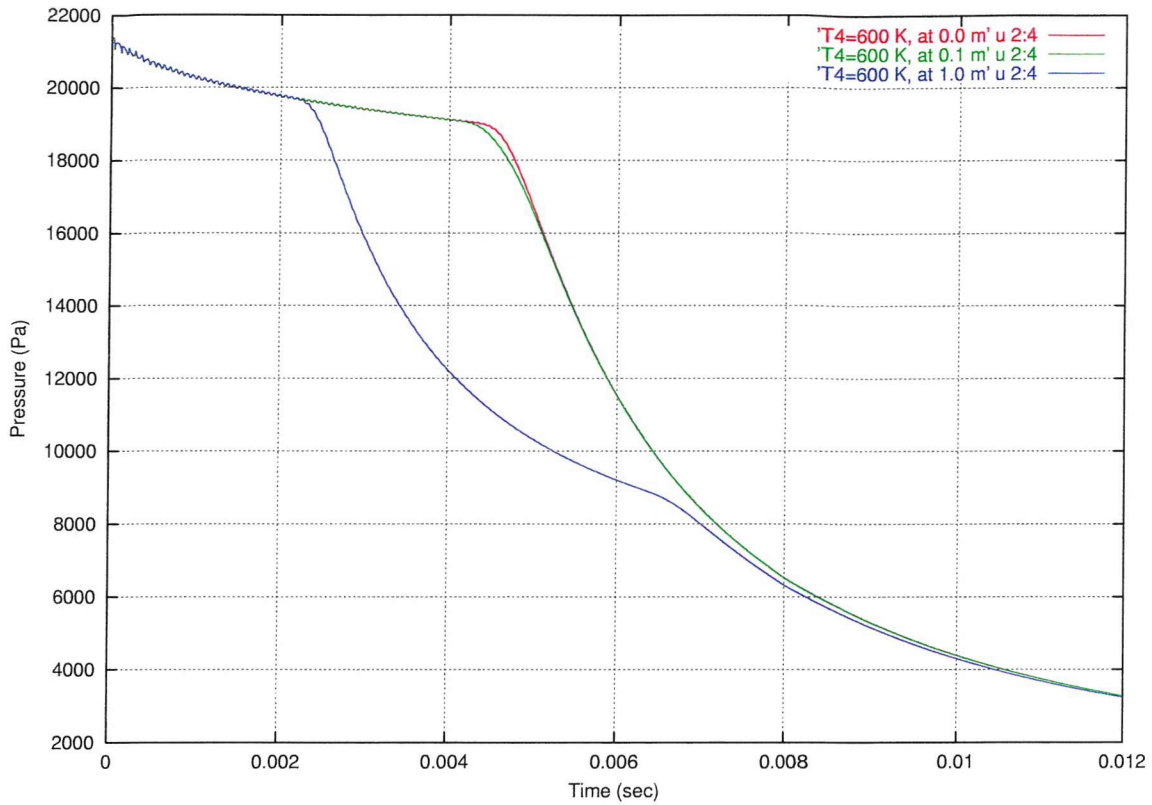
Fig. 4-35 (a) Computed pressure versus time for Argon using $P_{41} = 21.4$ at 600 K
at x = 0.0 $m$, x = 0.1 $m$ and x = 1.0 $m$
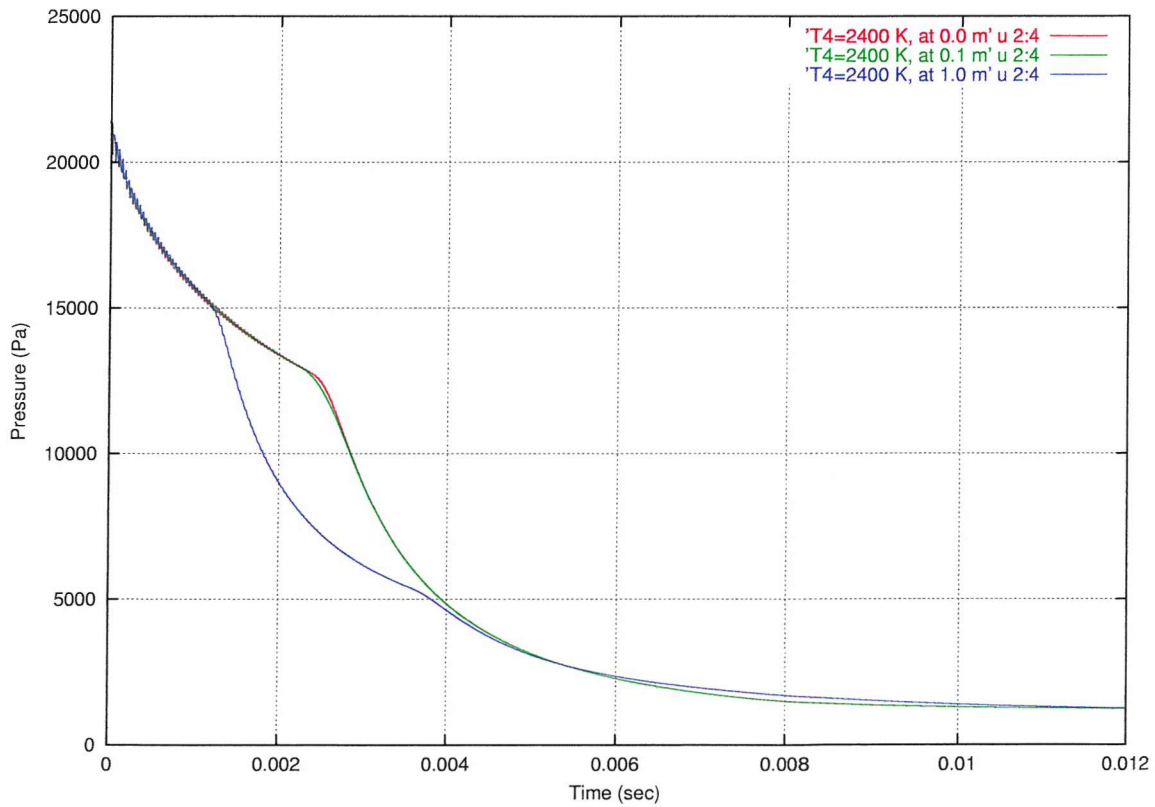


Fig. 4-35 (b) Computed pressure versus time for Argon using $P_{41} = 21.4$ at 2400 K
at x = 0.0 $m$, x = 0.1 $m$ and x = 1.0 $m$

Fig. 4-36 (a) Computed pressure versus time for Argon at 600 K along central line
at x = 0.0 *m*, x = 0.1 *m* and x = 1.0 *m*



Fig. 4-36 (b) Computed pressure versus time for Argon at 2400 K along central line
at x = 0.0 *m*, x = 0.1 *m* and x = 1.0 *m*
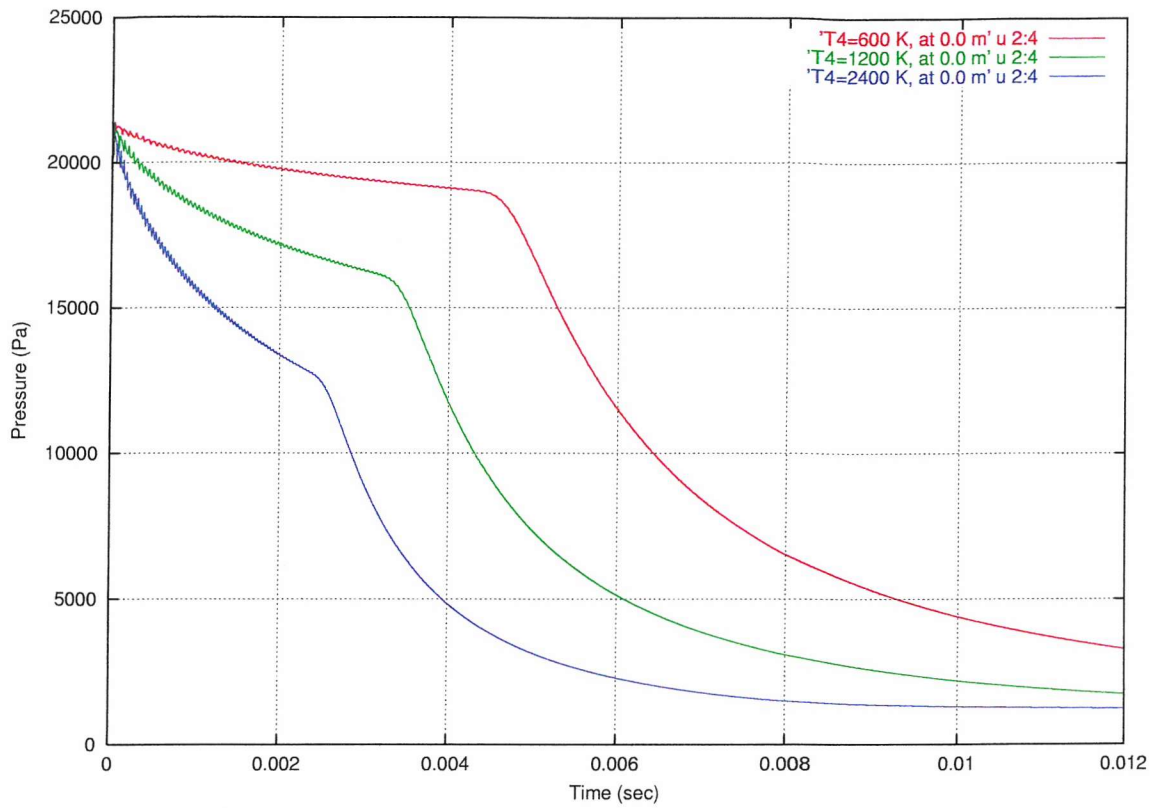
Fig. 4-37 (a) Computed pressure versus time for Argon at x = 0.0 m with three variable temperatures



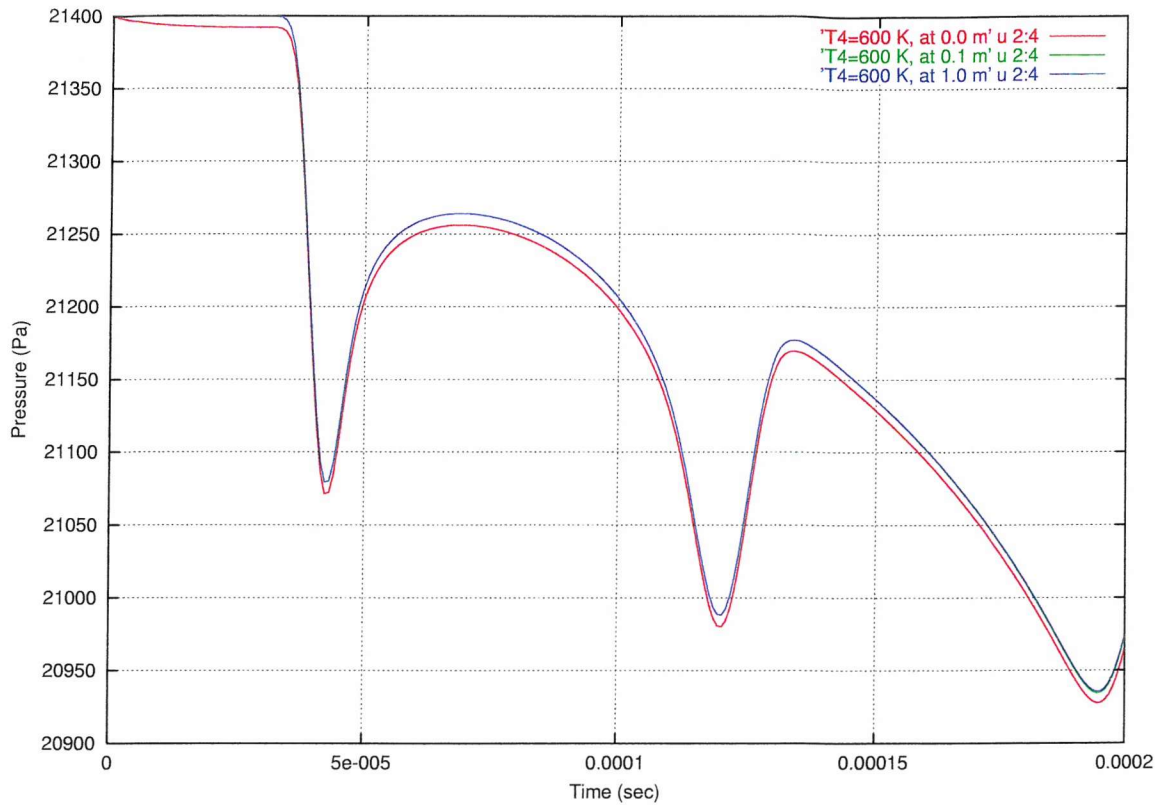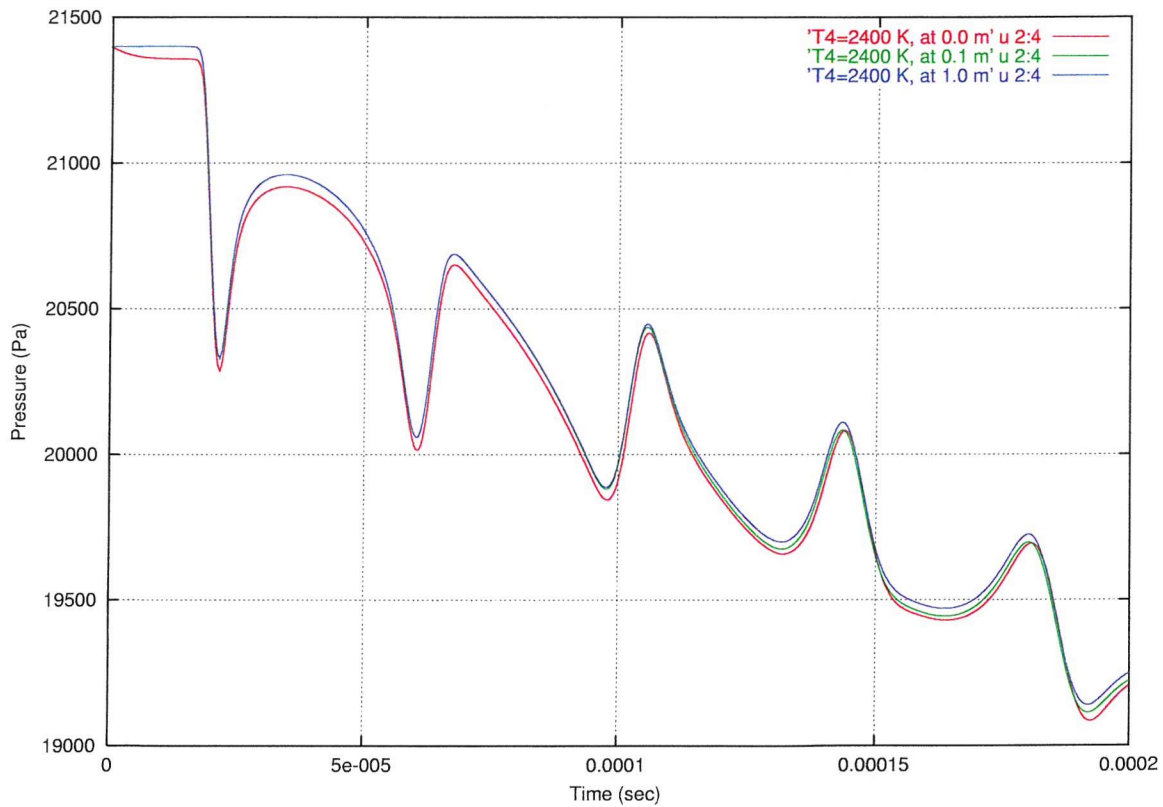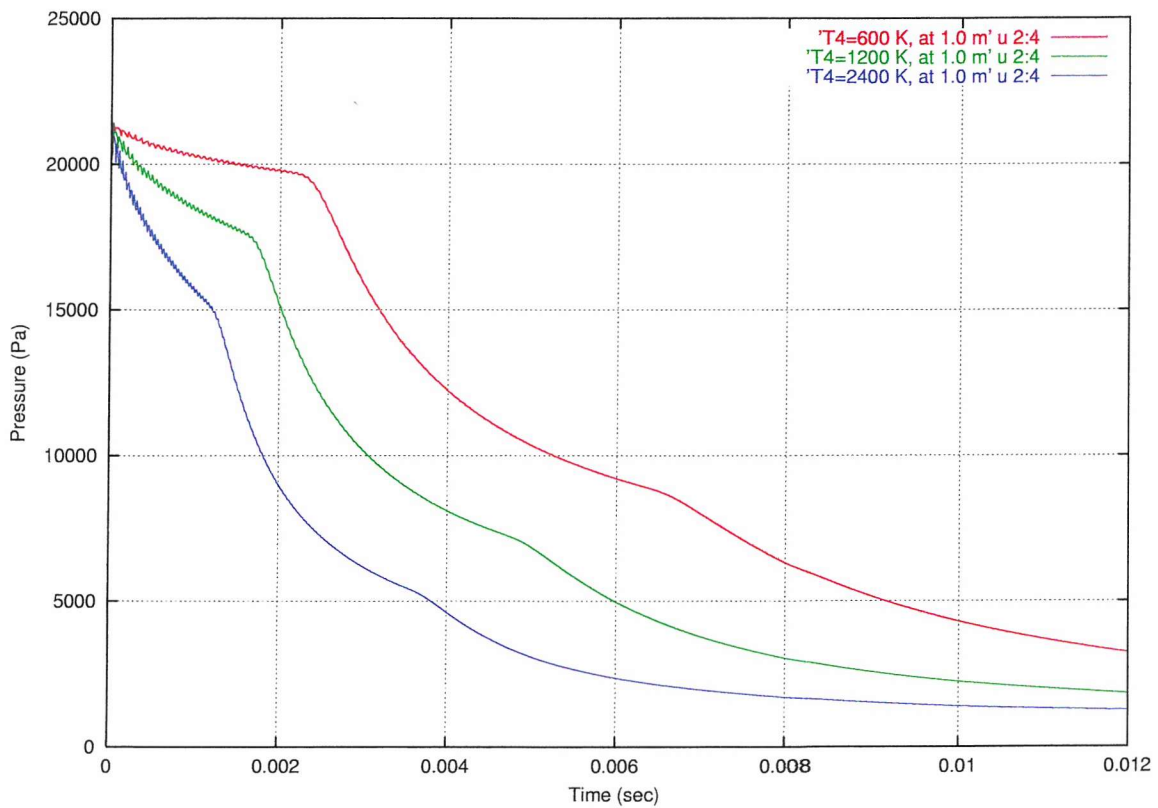Fig. 4-37 (b) Computed pressure versus time for Argon at x = 1.0 m with three variable temperatures

## 4.4 Expansion Tube Simulation

### 4.4.1 Introduction

A unique feature of the expansion tube which was proposed by Trimpi [45] among different types of pulse facilities including the HYPULSE expansion tube [48, 50] is that it theoretically avoids stagnating the flow within the facility and avoids any excitation and dissociation of the test gas. Hence, in principle, a better simulation of the free stream condition can be achieved using the experiment facilities, e.g. a reflected shock tunnel [31].

As in the previous facilities, it is also a useful device for achieving higher total pressure, and enthalpy test conditions than can be provided using other types of ground testing facilities, and for investigating hypersonic flow phenomena. It consists essentially of a single tube divided into three sections by diaphragms as follows: a driver, a driven section (containing the test gas), and an acceleration section. Fig. 4-38, which is a schematic diagram of the classic expansion tube described by Trimpi [45], shows the components and ideal operating sequence represented by the distance-time (x-t) diagram.



Fig. 4-38: Schematic diagram of expansion tube cycle. Numbers identify flow regions as defined by Trimpi [45]. (Not to scale)

## 4.4.2 Principle of Operation

In order to clarify the assumptions made in the numerical simulations, a brief explanation of the operation of the expansion tube is given here. As in the previous facilities, the operation begins by rupturing the primary diaphragm at time $t = 0$, a primary shock wave travels into t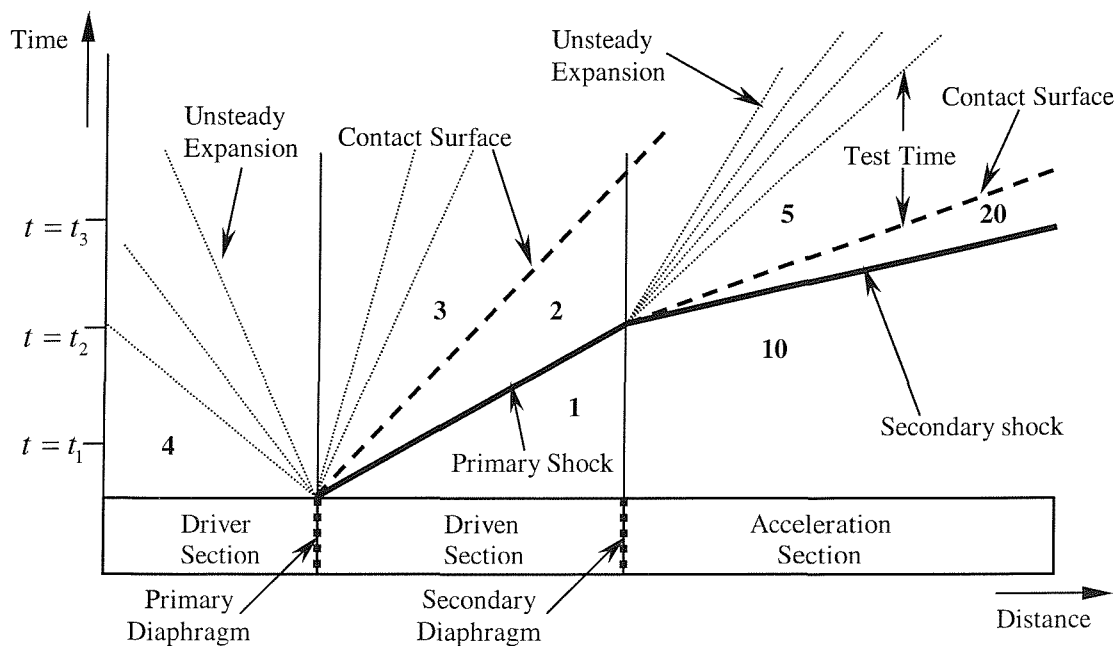he test gas, compressing it, and an expansion wave propagates into the driver gas at the same time, as illustrated in Fig. 4-38. The numbering of the flow states in the figure corresponds to the defined by Trimpi [45] as follows:

1: Quiescent test gas.

2: Test gas behind incident shock in driven section.

3: Driver gas following unsteady expansion.

4: Initial driver gas.

5: Test gas in acceleration section (free stream).

10: Quiescent acceleration gas.

20: Acceleration gas behind incident shock in acceleration section.

On reaching the end of the driven tube, the primary shock ruptures the secondary diaphragm. This creates a secondary incident shock and a second expansion both of which travel down the acceleration tube, while an another expansion wave moves into the test gas. This expansion wave is washed downstream, since the gas in region 2 is moving at higher speeds. Test time can start with the arrival of the test gas/accelerating gas contact discontinuity at the model and ends with the arrival of the expansion wave. The state of the gas in region 5 determines the test conditions. The velocities obtained in the test gas of region 5 can be very high ($\geq 10 km/s$) [31]. Test times in expansion tubes are typically tens to hundreds of microseconds long [11, 20]. In this ideal operating sequence, no stagnation regions are created and there are no high temperatures to dissociate the test gas.

## 4.4.3 Previous Research

Some researchers [20, 48, 50] have previously carried out computational simulations of expansion tube flow fields. Their goal was to investigate the flow

without explosive mixtures inside the expansion tube facility. Their calculations were restricted to the time interval $0 \leq t \leq t_2$ (See Fig. 4-38). Similarly, the focus of the present work is to have a look at the flow field and interaction among expansion wave, shock wave, interface and the boundary layer. Hence, the simulations were carried out for the same duration. These previous investigations, which were carried out by Sod [41] and Yee [51], were generally for relatively low pressure ratios across the diaphragm (ratios less than 10). Initial pressure ratios in a hypersonic pulse facility may be over 10000 in which case it has been found that special condition must be used [50].

### 4.4.4 Numerical Simulations

In this present work, the expansion tube facility used to carry out some simulations is a double-diaphragm shock tube which has an overall length of x = 7.11 *m* and an internal diameter of 0.038 *m*, with the primary diaphragm located at $x = 2.11$ *m* and the secondary diaphragm located at $x = 5.85$ *m* shown in Fig. 4-39. The dimensions were chosen to match the X1 expansion tube facility of the University of Queensland [35]. The numerical simulations of the expansion tube were carried out by using the HLLC Riemann solver without MUSCL slope limiter. Illustrated is a distance-time plotting of the one-dimensional inviscid simulation for a primary diaphragm pressure ratio ($P_4/P_1$) of 1000 and a secondary diaphragm pressure ratio ($P_1/P_{10}$) of 1, with all driver, driven and test gases initially at room temperature ($T_4 = T_1 = T_{10}$ =300 K). An overall 2844 uniformly spaced grid (N = $2844 \times 70$ for two-dimensional axisymmetric viscous simulations) was utilized in the simulations. Both two diaphragms are assumed to be removed instantaneously. The results of a simulation carried out for $P_1/P_{10}$ = 10 will also be given here for comparison with the results when $P_1/P_{10}$ = 1 is used.

The simulations for two-dimensional axisymmetric viscous flows are also carried out for $P_1/P_{10}$ = 1 and $P_1/P_{10}$ = 10. And the results will be discussed later. The

density contour figures are plotted within a specific range excluding the expansion region to illustrate more clearly the wave propagation phenomena in the test gas.

### 4.4.4.1 One-dimensional Simulations

In Fig. 4-39, the simulation with $P_1/P_{10} = 1$ was performed for non-dimensional secondary diaphragm rupture time $(t_d) = 0.0658$ corresponding to burst delay time of approximately 25 $\mu s$. The plotting shows that the interaction of the primary shock (PS) and the secondary diaphragm causes a reflected shock (RS) to form then propagate back to the driven chamber. As the secondary diaphragm has been burst, the secondary shock (SS) is propagated into the test gas, and a secondary expansion (SE) is also formed followed. A secondary contact surface (SCS), which separates the shock heated test gas from the expanded test gas, is also formed. These features shown in Fig. 4-39 are similar to those shown in some investigations [20, 21, 48]. Later, the reflected shock upstream interacts with the primary contact surface (PCS) to cause the reflected shock to be propagated downstream. In the meanwhile, due to the over-tailored conditions which exist, the interaction of the reflected shock with the contact surface causes another shock wave- termed the disturbance shock (DS) to be propagated into the test gas. Fig. 4-40 shows that the disturbance shock is very weak. The disturbance shock passes through the secondary expansion and travels into the test gas at a higher speed $(U_{DS} = 1175.52$ *m/s*) as it follows behind the secondary shock $(U_{SS} = 924.43$ *m/s*). Then, the secondary expansion interacts with the primary contact surface to cause the reflected expansion (RE) to propagate closely behind the disturbance shock. The test time starts from the arrival of the secondary contact surface till the arrival of the disturbance shock. It is only 0.55 *ms* long for the test gas with good quality.

Fig. 4-41 shows that the simulation is carried out for $P_1/P_{10} = 10$ with the same burst delay time of approximately 25 $\mu s$. After the secondary diaphragm is burst, a secondary shock (SS) propagates into the test gas at a higher shock speed of 1452.81 *m/s* and a secondary contact surface (SCS) is formed to propagate at a speed of 1033.14 *m/s* behind the secondary shock. A secondary expansion (SE) is also formed to propagate into the test gas behind the secondary contact surface.

The reflected shock (RS) interacts with the primary contact surface (PCS) to cause the reflected shock to be propagated downstream into the test gas and a reflected expansion (RE) is formed to propagate behind the secondary expansion. However, a feature of disturbance shock shown in Fig. 4-39 is not seen in Fig. 4-41 because the region between the secondary expansion and the reflected expansion is smeared out and the resulting disturbances are very weak. Because of this, the test time starts from the arrival of the secondary contact surface and lasts until the arrival of the secondary expansion. It is 0.9 *ms* for the test gas with good quality. It is longer than the test time calculated for $P_1/P_{10} = 1$. Fig. 4-42 shows that the disturbance shock (DS) becomes stronger as the secondary expansion (SE) travels into the test gas.

### 4.4.4.2 Two-dimensional Axisymmetric Viscous Simulations

In comparison with the results of one-dimensional inviscid flow, the simulations of two-dimensional axisymmetric viscous flow have been carried for $P_1/P_{10} = 1$ and $P_1/P_{10} = 10$. Fig. 4-43 shows that the details of the boundary layer can be observed in the simulations of the expansion tube for $P_1/P_{10} = 1$ and 10 at 0.005 *sec*.

First, Fig. 4-44 shows a distance-time plotting of the viscous flow carried out with $P_1/P_{10} = 1$, and it shows that a disturbance shock (DS) shown in Fig.4-39 are not shown in Fig. 4-44 because it is very weak and smeared out. And the detail of a secondary contact surface (SCS) is not very clear that can be observed in Fig. 4-43 (a). After the secondary diaphragm has been burst, the secondary shock (SS) propagates into the test gas at the speed of 820.4 *m/s*, which is slower than its primary shock speed. Fig. 4-45 shows a computed pressure-time plotting and it shows that the reflected shock (RS) downstream of the secondary diaphragm is very weak and it appears to be smeared out with the primary expansion (PE). However, the available test time is only approximately 0.1 *ms* for the test gas with good quality.

Finally, a distance-time plotting performed for $P_1/P_{10} = 10$ and its computed pressure-time plotting are shown in Fig. 4-46 and Fig. 4-47, respectively. Fig. 4-46 shows that the secondary shock (SS) propagates into the test gas at the speed of 1400.1 *m/s* initially as the secondary diaphragm has been burst, then the shock speed decays to 1195.22 *m/s* later due to the viscous effects. It also shows that the secondary contact surface (SCS) propagates into the test gas at the constant speed of 1221.72 *m/s* behind the secondary shock (SS). The disturbance shock (DS) shown in Fig.4-47 appears to smear out with the reflected shock (RS) that can be seen in Fig. 4-43 (b) and the reflected shock travels into the test gas slower than that shown in Fig. 4-41. However, the test time for the test gas with good quality is approximately 0.3 *ms*.

## 4.4.5  Discussions

The simulations have been carried out to investigate the details of wave propagation of the primary shock interaction with the secondary diaphragm and the interaction between the reflected shock and the secondary expansion on the quality and duration of the test gas. It also shows that the pressure ratio of the secondary diaphragm $P_1/P_{10}$ may have an influence on the duration of the test gas with good quality [35, 36]. It appears that the test times obtained from the viscous simulations are much shorter than those of the inviscid simulations due to the viscous effects and numerical diffusions.

However, the situation where $P_1/P_{10} = 1$ is not valid for a real expansion tube flow (since the shock would not accelerate). It was used by Roberts et al [35, 36] to investigate shock-diaphragm interaction phenomena under specific conditions.

Fig. 4-39 Wave diagram of the density profile for 1-D inviscid simulation with $P_1/P_{10} = 1$

Fig. 4-40 Computed pressure versus time for 1-D inviscid simulation with $P_1/P_{10} = 1$
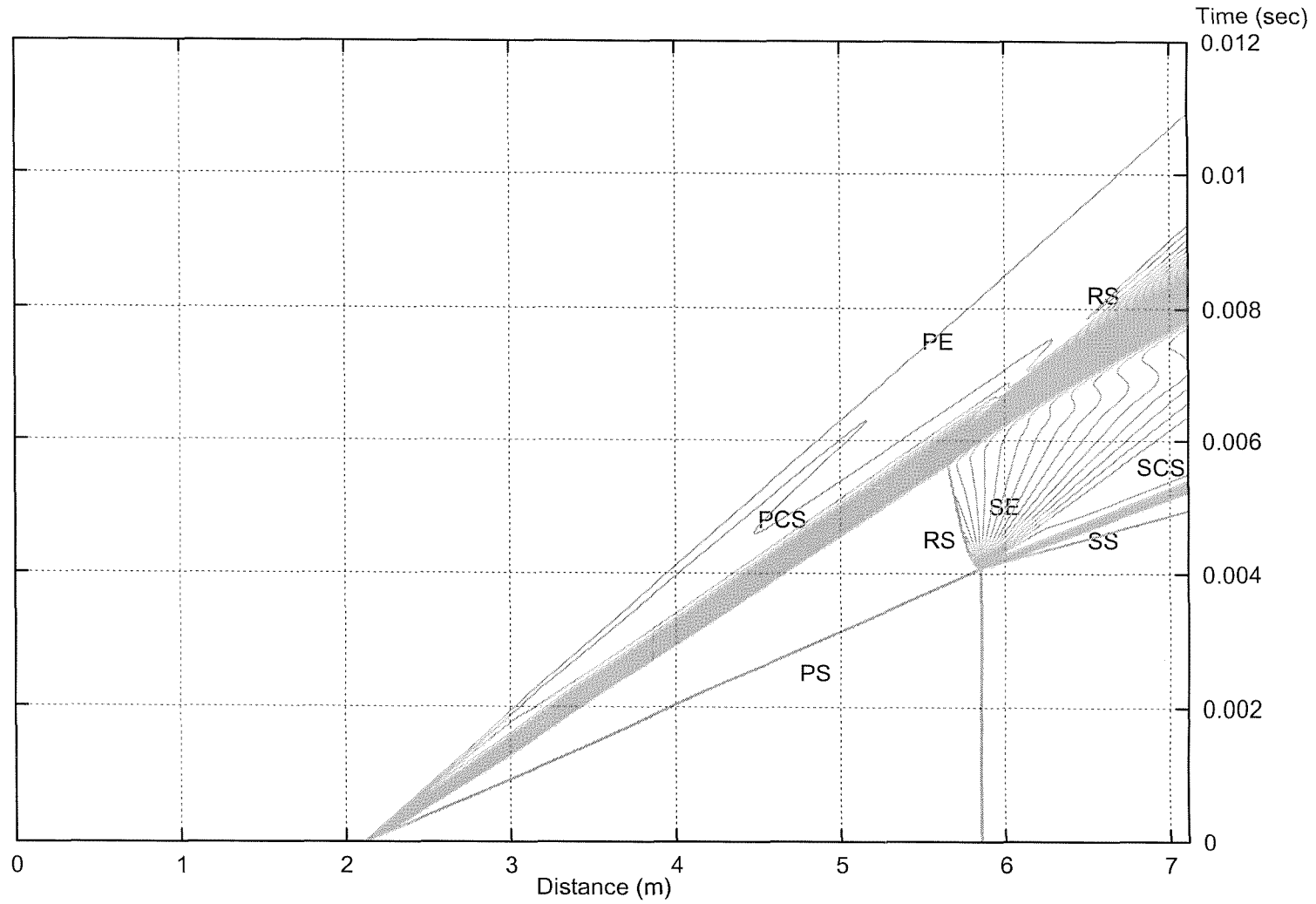
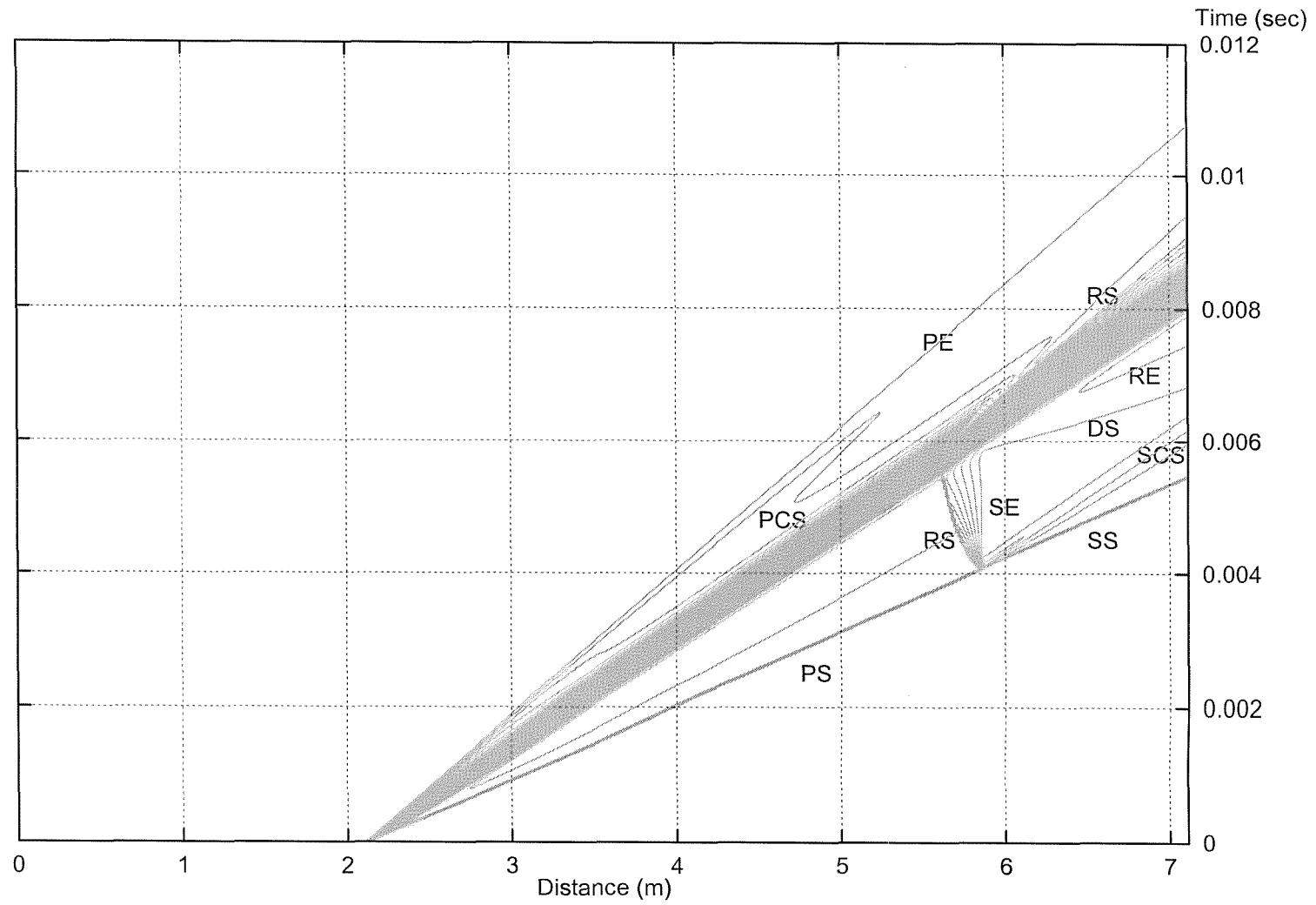Fig. 4-41 Wave diagram of the density profile for 1-D inviscid simulation with $P_1/P_{10} = 10$

Fig. 4-42 Computed pressure versus time for 1-D inviscid simulation with $P_1/P_{10} = 10$

(a) The density contour for $P_1/P_{10} = 1$
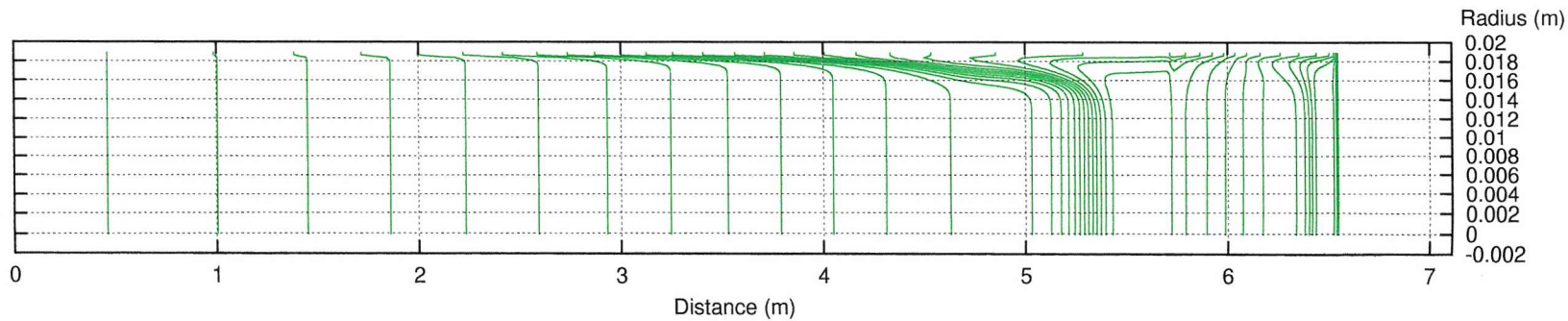
(b) The density contour for $P_1/P_{10} = 10$

Fig. 4-43 Density contours of 2-D axisymmetric viscous simulations with $P_1/P_{10} = 1$ and $P_1/P_{10} = 10$ at 0.005 sec

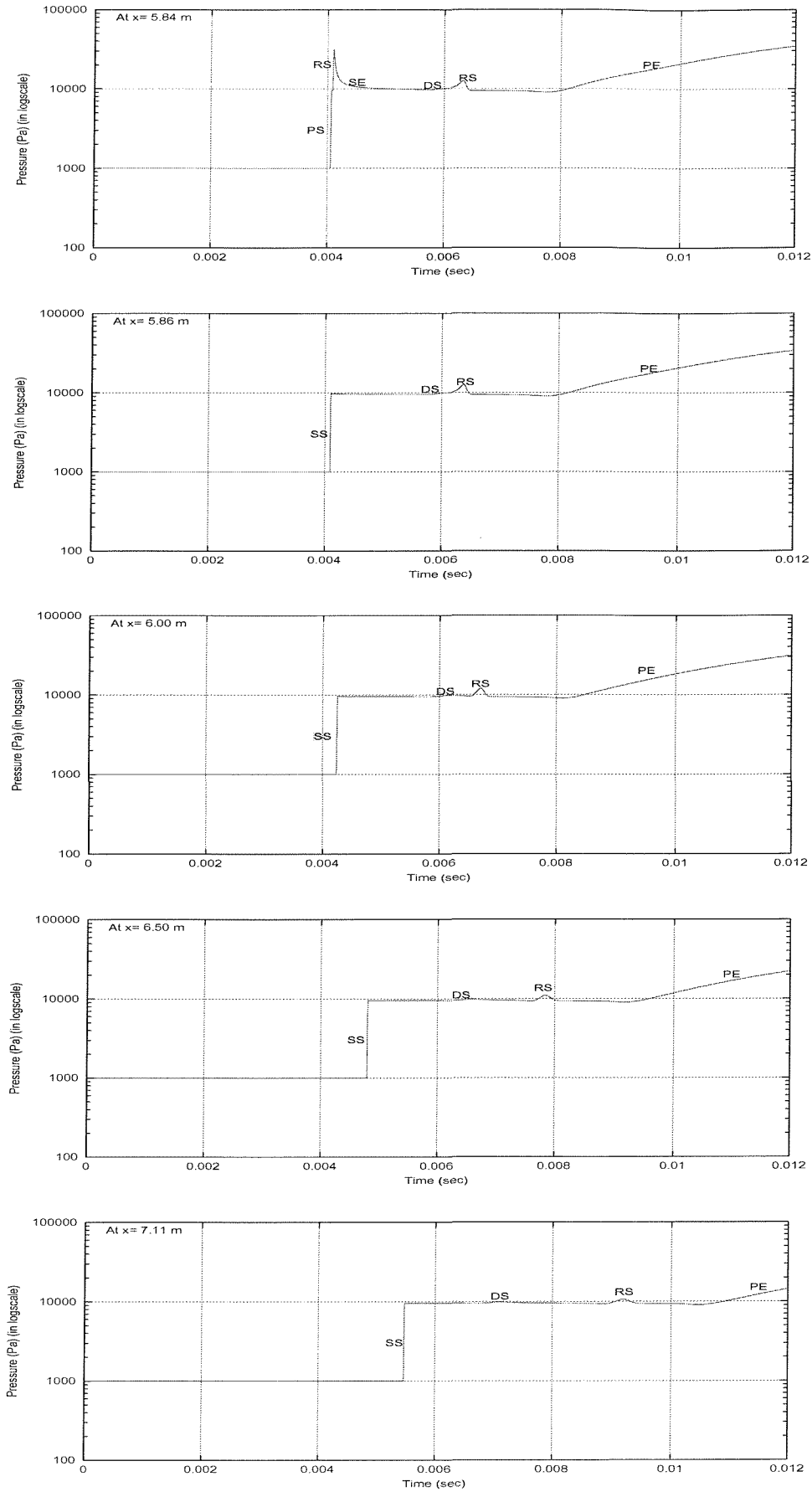Fig. 4-43 Wave diagram of the density profile for 2-D axisymmetric viscous simulation with $P_1/P_{10} = 1$

Fig. 4-45 Computed pressure versus time for 2-D axisymmetric viscous simulation with $P_1/P_{10} = 1$

Fig. 4-45 Wave diagram of the density profile for 2-D axisymmetric viscous simulation with $P_1/P_{10} = 10$

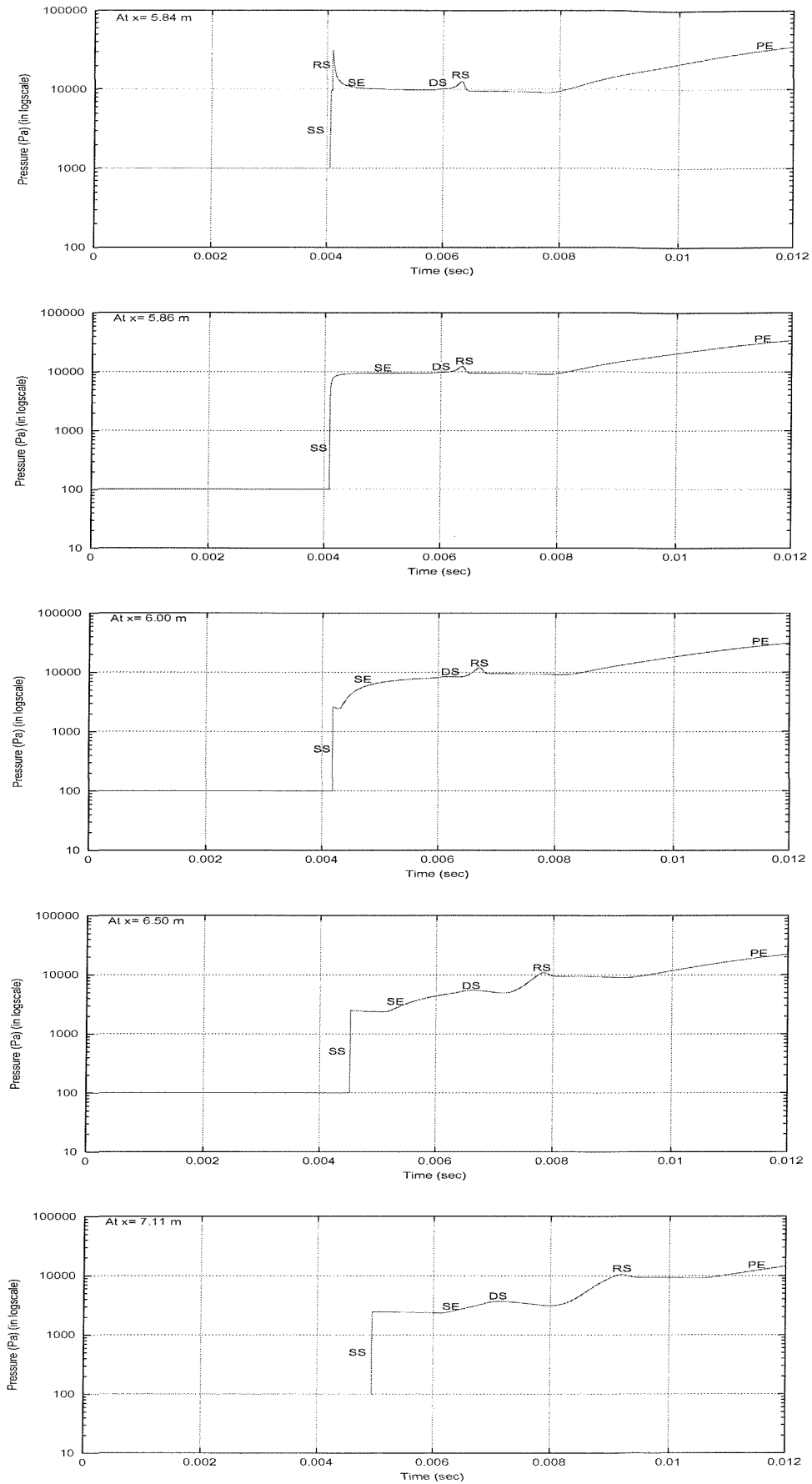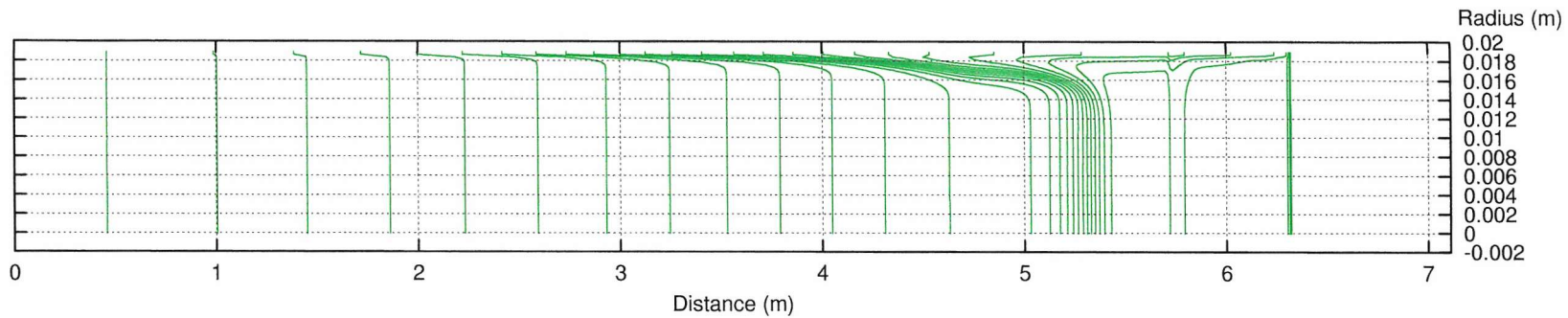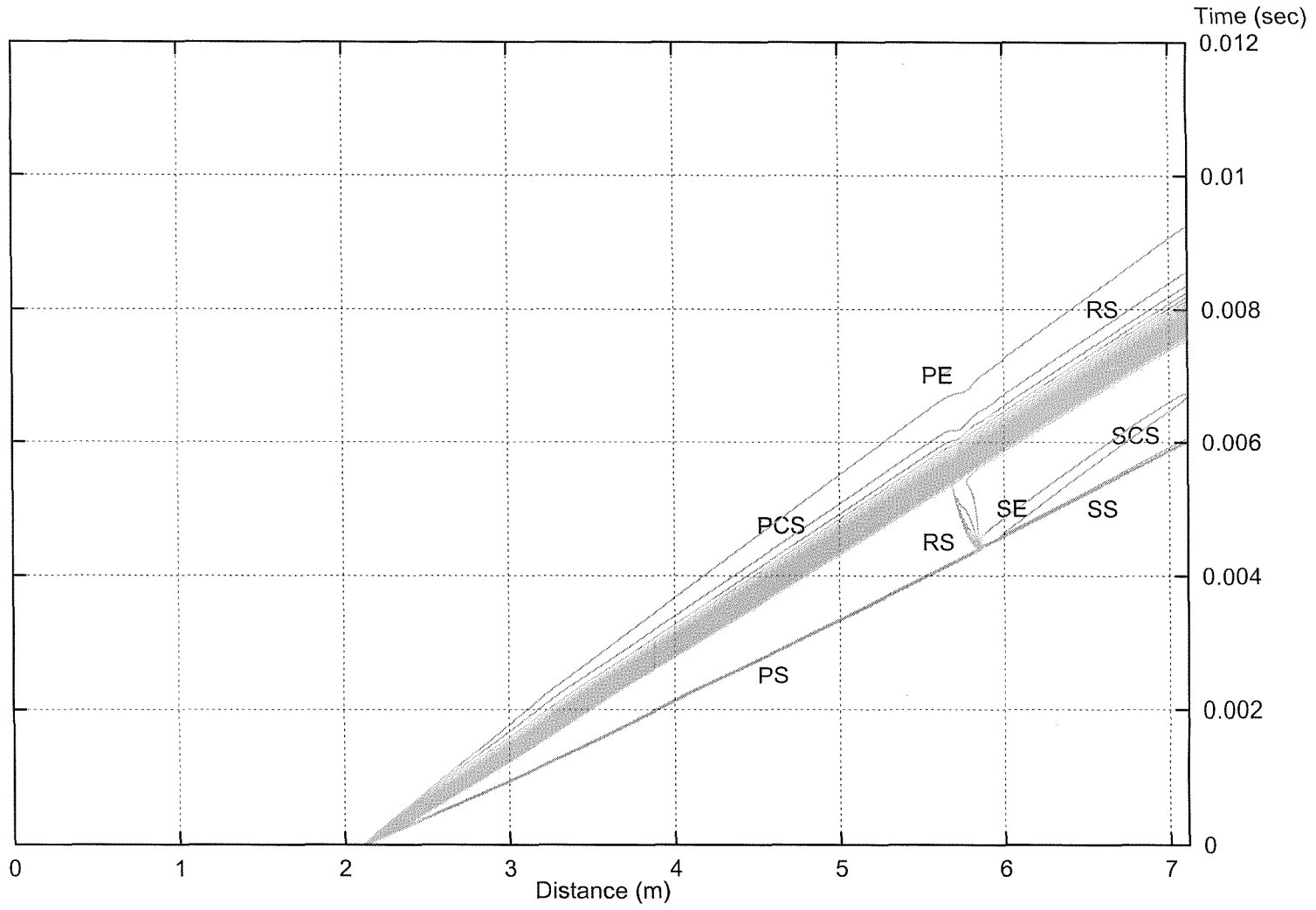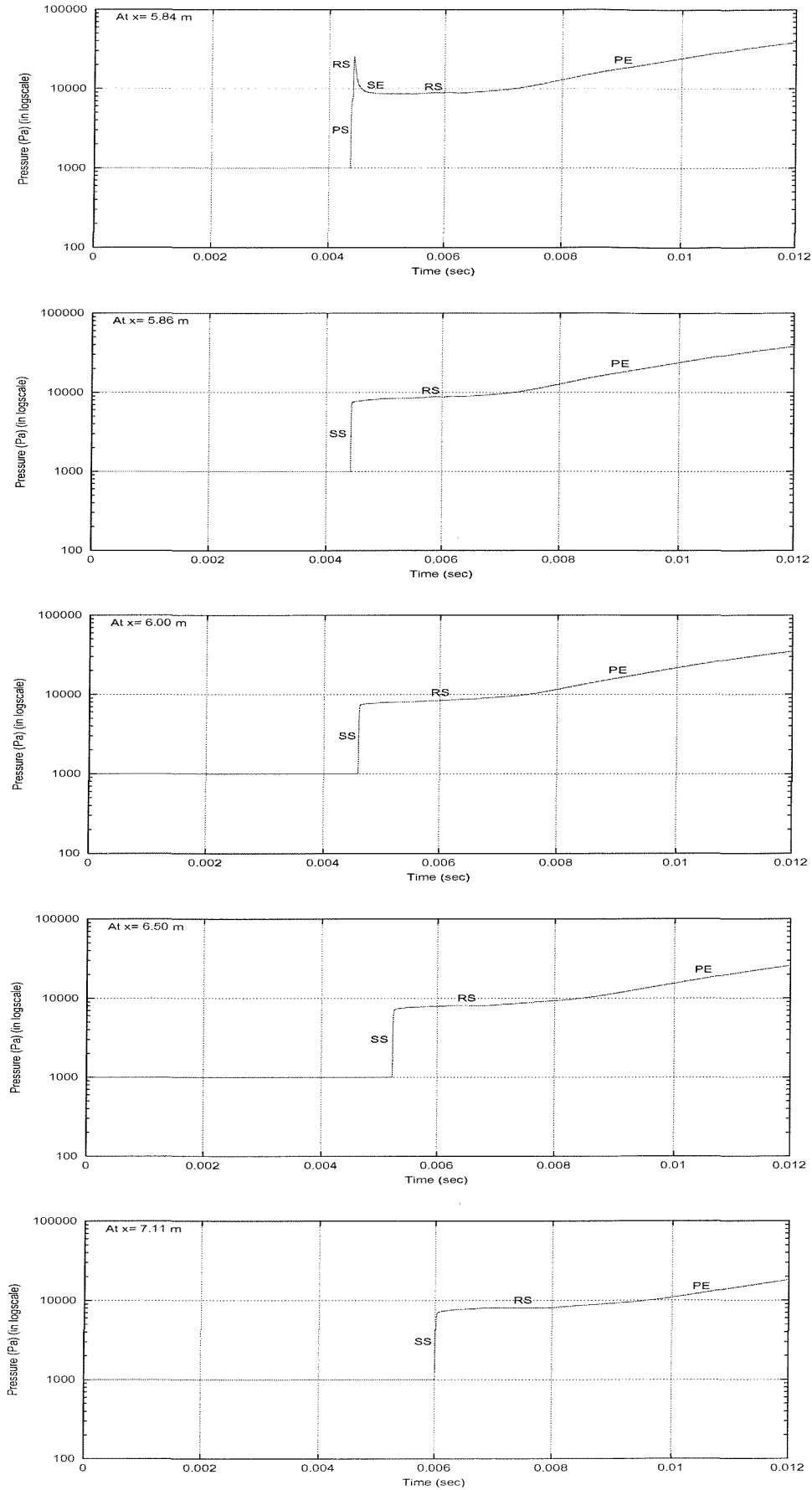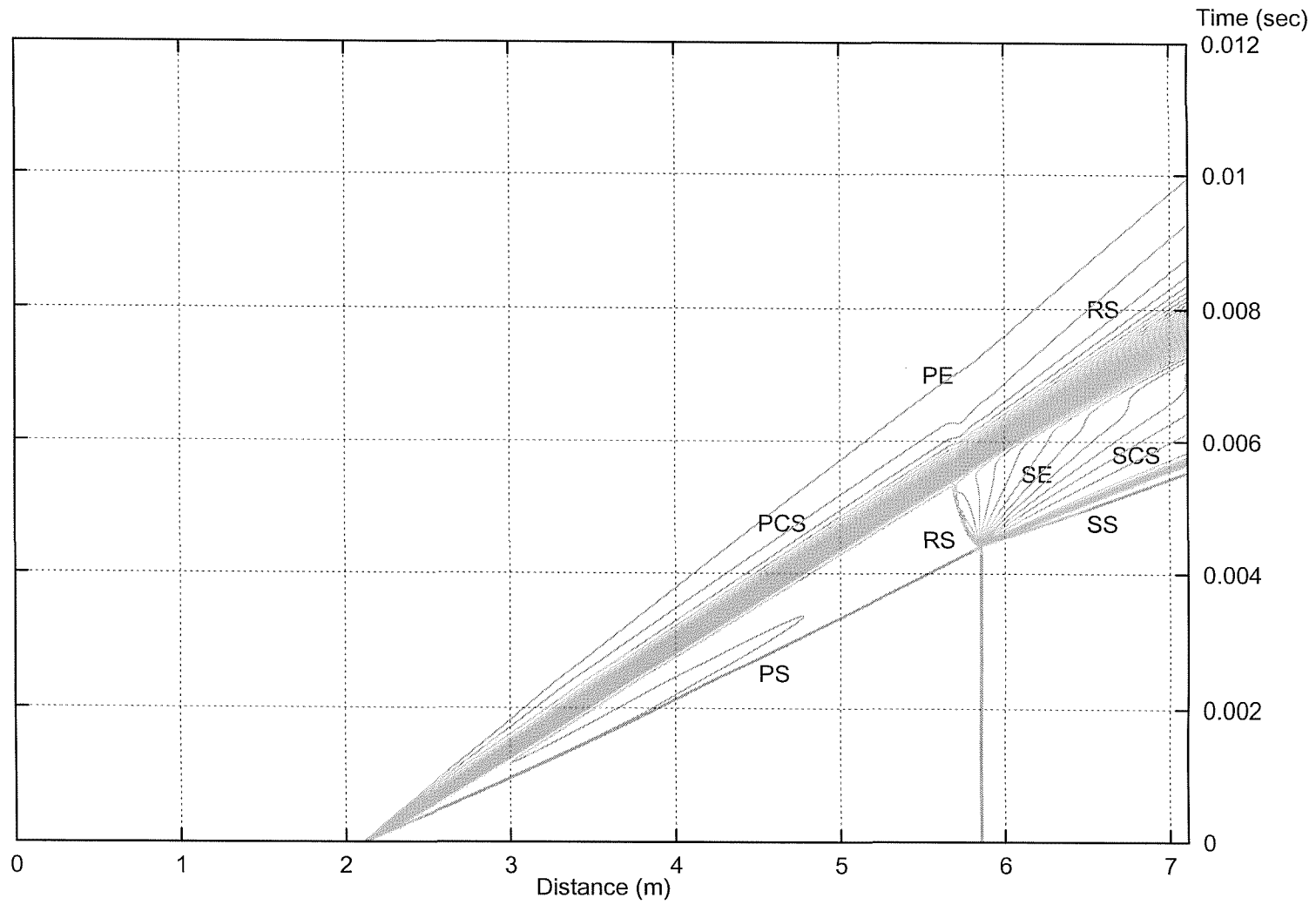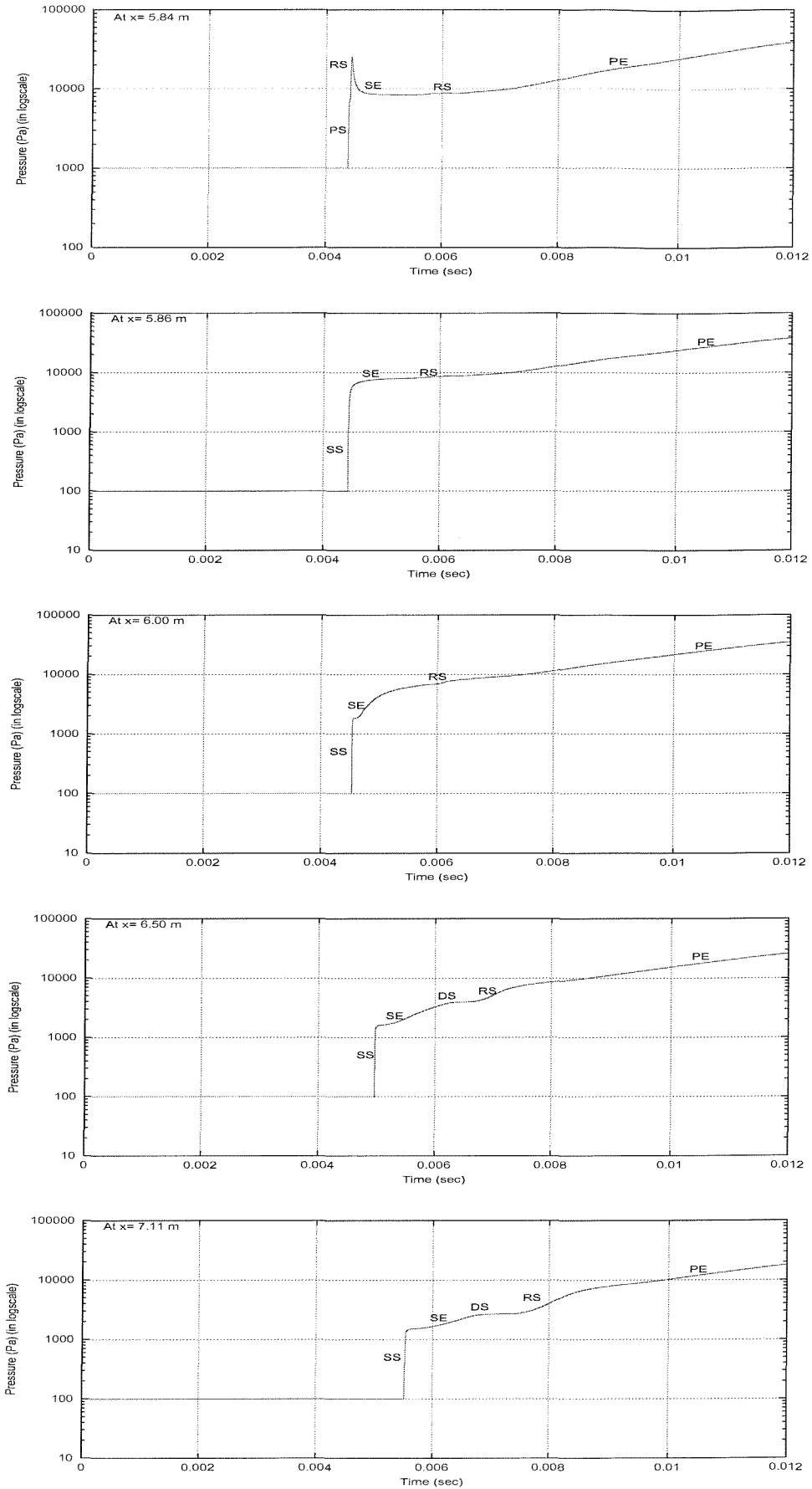Fig. 4-47 Computed pressure versus time for 2-D axisymmetric viscous simulation with $P_1/P_{10} = 10$

# Chapter 5

# Conclusions and Further Work

The work presented in this thesis concerns the numerical simulations of one-dimensional inviscid and two-dimensional axisymmetric viscous shock and expansion flow problems with perfect gas considered. The prediction of wall heat transfer rate and the wave phenomena of shock tube with variable tailoring conditions have been given.

The numerical scheme using HLLC Riemann solver has been investigated to determine their suitability for the variable pressure ratios across the primary and secondary diaphragms. In this respect, the HLLC solver showed that it may be the most appropriate approximate Riemann solver for low pressure ratio (e.g.: $P_4/P_1$=10) with a reasonable number of grid points. However, the solver suffers quite severe numerical diffusions and inaccuracy when the pressure ratio $P_4/P_1$ is larger, in particular in higher speed and higher temperature gas. It was also found that it is possible to reduce numerical diffusions when more grid points are given. However, it may cost more in the computing time.

From the simulations, simple shock tube flows show good agreements with analytical theory, although indicate that numerical diffusion may be severe particularly near the contact surface. Viscous phenomena in simple shock tube flows show the expected trends of reduced test times due to primary shock deceleration and contact surface acceleration. Good agreement with the heat

transfer theory of Mirels was obtained. Examples of tailored-interface conditions, under-tailored and over-tailored conditions, were computed for reflected shock tube flows. The phenomena observed were consistent to those expected from analytical theory. Again, viscous flow effects were observed to reduce the total test time available. During the investigation, the influence of loss of energy from a heated driver gas appeared to produce a set of transverse pressure waves in the driver chamber propagating at the local acoustic speed. A study of expansion tube flows was conducted, in which the rupture of the secondary diaphragm was delayed. This resulted in complex wave interaction phenomena, the net result of which was to reduce the test time.

Further work may be addressed to obtain appropriate solutions with higher number of grid points and high order schemes for increasing accuracy. Contact surface tracking and moving grid may be considered to be used when it is necessary. The gradual opening diaphragm process may be an important key to mimic the real conditions. The computational requirements of the shock and expansion tube problem will cost more, the approximate Riemann solver technique should be adapted in order to improve in computing speed and accuracy.

Also, it is necessary to achieve more appropriate solutions and more accurate results for the shock and expansion tube problems involving higher pressure ratio across diaphragm, higher shock speed and higher temperature flow.

# Appendix A

# Non-dimensionalisation

To achieve the flow behaviors with minimum computational (or experimental) effort, it is necessary to transform all the parameters into non-dimensional variables, for example, density and free stream velocity. It is known that two flows are dynamically similar when the non-dimensional variables have the same value. Hence, the best way to identity the certain non-dimensional variables is to non-dimensionalise the quantities used for the governing equation as following:

Density: $\qquad \rho^* = \dfrac{\rho}{\rho_\infty}$

Pressure: $\qquad P^* = \dfrac{P}{\rho_\infty U_\infty^2}$

Velocity: $\qquad u^* = \dfrac{u}{U_\infty}, \quad v^* = \dfrac{v}{U_\infty}$

Temperature: $\qquad T^* = \dfrac{T}{T_\infty}$

Energy: $\qquad E^* = \dfrac{E}{\rho_\infty U_\infty^2}$

Special heats: $\qquad C_p{}^* = \dfrac{C_p}{U_\infty^2/T_\infty}, \quad C_v{}^* = \dfrac{C_v}{U_\infty^2/T_\infty}$

Time: $\qquad t^* = \dfrac{t}{L/U_\infty}$

Length: $\qquad x^* = \dfrac{x}{L}, \quad r^* = \dfrac{r}{L}$

Viscosity: $\qquad \mu^* = \dfrac{\mu}{\mu_\infty}$

Where $\rho_\infty$, $U_\infty$, $T_\infty$ and $\mu_\infty$ are free-stream reference values, and $L$ is a characteristic length such as the hydraulic diameter for 2-D axisymmetric flow simulations.

# Appendix B

# Analytical Solution of

# the Riemann Problem

To find the analytical solution of the Riemann Problem, consider three states: the shock, the contact surface and the expansion fan. Consider the Hugoniot relation [2, 22], the state of the shock can be given by

$$\frac{a_2^{\,2}}{a_1^{\,2}} = \frac{P_2}{P_1} \frac{\frac{\gamma+1}{\gamma-1} + \frac{P_2}{P_1}}{1 + \frac{\gamma+1}{\gamma-1} \frac{P_2}{P_1}}, \tag{B-1}$$

$$u_2 = u_1 + \frac{a_1}{\gamma} \frac{\frac{P_2}{P_1} - 1}{\sqrt{\frac{\gamma+1}{2\gamma}\left(\frac{P_2}{P_1} - 1\right) + 1}}, \tag{B-2}$$

$$S = u_1 + a_1 \sqrt{\frac{\gamma+1}{2\gamma}\left(\frac{P_2}{P_1} - 1\right) + 1}. \tag{B-3}$$

Then, the state of the contact surface can be given by

$$u_2 = u_3, \tag{B-4}$$

$$P_2 = P_3. \tag{B-5}$$

Finally, the state of the expansion fan can be given by

$$u(x,t) = \frac{2}{\gamma+1}\left(\frac{x}{t} + \frac{\gamma-1}{2}u_4 + a_4\right), \tag{B-6}$$

$$a(x,t) = u(x,t) - \frac{x}{t} = \frac{2}{\gamma+1}\left(\frac{x}{t} + \frac{\gamma-1}{2}u_4 + a_4\right) - \frac{x}{t}, \tag{B-7}$$

$$P = P_4\left(\frac{a}{a_4}\right)^{2\gamma/(\gamma-1)} . \tag{B-8}$$

Then, consider the simple wave condition $u + 2a/(\gamma+1) = constant$, the relation of the expansion fan can be given by

$$u_3 + \frac{2a_3}{\gamma-1} = u_4 + \frac{2a_4}{\gamma-1} \tag{B-9}$$

Combining Equations (B-8) and (B-9) gives

$$u_3 = u_4 + \frac{2a_4}{\gamma-1}\left[1 - \left(\frac{P_3}{P_4}\right)^{(\gamma-1)/2\gamma}\right] \tag{B-10}$$

And combining Equations (B-4), (B-5) and (B-9) gives

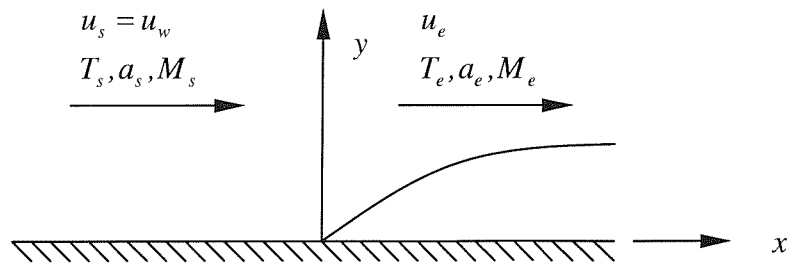$$u_2 = u_4 + \frac{2a_4}{\gamma-1}\left[1 - \left(\frac{P_2}{P_4}\right)^{(\gamma-1)/2\gamma}\right] \tag{B-11}$$

Therefore, solving the Equations (B-2) and (B-11) can give

$$\frac{P_4}{P_1} = \frac{P_2}{P_1}\left\{1 + \frac{\gamma-1}{2a_4}\left[u_4 - u_1 - \frac{a_1}{\gamma}\frac{\frac{P_2}{P_1}-1}{\sqrt{\frac{\gamma+1}{2\gamma}\left(\frac{P_2}{P_1}-1\right)+1}}\right]\right\}^{-2\gamma/(\gamma-1)} \tag{B-12}$$

# Appendix C

# Shock Relations

In the Mirels' works [27], for convenience, some normal shock relations are re-written as:



In the shock-fixed coordinate system, the flow may be assumed to be steady. Then, assume that subscript "s" designates the undisturbed flow in front of the shock; and subscript "e" designates the flow behind the shock and external to the boundary layer. Here, $M_s = u_s/a_s = u_w/a_s$.

$$\frac{u_w}{u_e} = \frac{(\gamma+1)M_s^2}{2+(\gamma-1)M_s^2} = \frac{4M_s^2}{M_s^2+3} \qquad \text{for } \gamma = 1.667 \qquad (C\text{-}1)$$

$$M_e^2 = \frac{2}{(\gamma+1)\frac{u_w}{u_e}-(\gamma-1)} = \frac{3}{4\frac{u_w}{u_e}-1} \qquad \text{for } \gamma = 1.667 \qquad (C\text{-}2)$$

$$\frac{T_e}{T_s} = \frac{(\gamma+1)\frac{u_w}{u_e}-(\gamma-1)}{(\gamma+1)\frac{u_w}{u_e}-(\gamma-1)\frac{u_w}{u_e}^2} = \frac{4\frac{u_w}{u_e}-1}{4\frac{u_w}{u_e}-\frac{u_w}{u_e}^2} \qquad \text{for } \gamma = 1.667 \qquad (C\text{-}3)$$

# Bibliography

[1]  S. Amaratunga. Surface Catalytic effects in Non-equilibrium, Viscous Hypersonic Flow. Ph. D. Thesis, University of Southampton, 1998.

[2]  J. D. Anderson, Jr. Modern Compressible Flow with Historical Perspective. McGraw-Hill, 1990.

[3]  P. Batten, D. M. Ingram, R. Saunders and D. M. Causon. A Time-Splitting Approach to Solving the Navier-Stokes Equations. Computers and Fluids, Vol. 25, No. 4, pp. 421-431, 1996.

[4]  P. Batten, N. Clarke, C. Lambert and D. Causon. On the Choice of Wavespeeds for the HLLC Riemann Solver. SIAM, Journal of Science Computing, Vol. 18, No. 6, pp. 1553-1570, November, 1997.

[5]  J. L. Cambier, S. Tokarcik and D. K. Prabhu. Numerical Simulations of Unsteady Flow in a Hypersonic Shock Tunnel Facility. AIAA Paper 92:4029, 1992.

[6]  P. Colella, H. M. Glaz. Efficient Solution Algorithms for the Riemann Problem for Real Gases. Journal of Computational Physics, Vol. 59, pp. 264-289, 1985.

[7]  L. Davies. The Interaction of the Reflected Shock with the Boundary Layer in a shock Tube and its Influence on the Duration of Hot Flow in the Reflected-Shock Tunnel. Part 1. NPL Aero Report 1158 (A.R.C. 27 110), 1965.

[8]  R. E. Dillon. A Numerical Study of the Test Time in a Hypersonic Shock Tunnel. NASA Report AD-A194057, 1988.

[9]  R. E. Duff. Shock-Tube Performance at Low Initial Pressure. The Physics of Fluids, Vol. 2, No. 2, pp. 207-216, 1959.

[10] B. Einfeldt. On Godunov-Type Methods for Gas Dynamics. SIAM Journal of Numerical Analysis, Vol. 25, No. 2, pp. 294-318, 1988.

[11] J. Erdos, J. Galleja and J. Tamagno. Increase in the Hypervelocity Test Envelope of the HYPULSE Shock-Expansion Tube. AIAA Paper 94-2524, 18th AIAA Aerospace Ground Testing Conference, Colorado Spring, Colo., June, 1994.

[12] I. I. Glass, W. Martin and G. N. Patterson. A theoretical and experimental study of the shock tube. University of Toronto, UTIA Report No. 2, 1953.

[13] I. I. Glass. Shock Tubes. University of Toronto, UTIA Review No. 12, 1958.

[14] S. K. Godunov. A Difference Method for the Numerical Calculation of Discontinuous Solutions of Hydrodynamics Equations. Mat. Sbornik. 47, pp. 271-290, 1959.

[15] A. Harten, P. D. Lax and B. Van Leer. On Upstream Differencing and Godunov-Type Schemes for Hyperbolic Conservation Laws. SIAM Review, Vol.25, pp. 35-61, 1983.

[16] B. D. Henshall. On Some Aspects of the Use of Shock Tubes in Aerodynamic Research. A. R. C. Reports and Memoranda No. 3044, 1955.

[17] C. Hirsch. Numerical Computation of Internal and External Flows Vol. 2. A Wiley-Interscience Publication, 1990.

[18] K. A. Hoffmann and S. T. Chiang. Computational Fluid Dynamics for Engineers Vol. 2. Engineering Education System, Texas, 1993.

[19] D. W. Holder and D. L. Schultz. On the Flow in a Reflected-Shock Tunnel. ARC Reports and Memoranda No. 3265, London, 1962.

[20] P. A. Jacobs. Numerical Simulation of Transient Hypervelocity Flow in an Expansion Tube. Computers and Fluids, Vol. 23, No. 1, pp. 77-101, 1994.

[21] K. Kage, G. T. Roberts and K. Ishimatsu. Numerical Study of Shock-Diaphragm Interaction in Shock-Expansion Tubes. In 22nd International Symposium on Shock Waves, Imperial College, London, Paper 1730, 1999.

[22] C. B. Laney. Computational Gasdynamics. Cambridge University Press, 1998

[23] C. G. Miller and J. J. Jones. Incident Shock-Wave Characteristics in Air, Argon, Carbon Dioxide and Helium in a Shock Tube with Unheated Helium Driver. Technical Report TN D-8099, NASA, Langley Research Center, Hampton, VA 23665.

[24] J. K. Milthorpe. Numerical Simulation of Two-Dimensional and Axi-Symmetric Compressible Flows. Proceeding of 18th International Symposium on Shock Waves, Vol. 2, pp. 1133-1138, 1991.

[25] J. K. Milthorpe. Numerical Simulation of Two-Dimensional Compressible Flows. International Journal of Numerical Methods for Heat and Fluid Flow, Vol. 3, pp. 223-231, 1993.

[26] H. Mirels. Laminar Boundary Layer behind Shock Advancing into Stationary Fluid. NACA TN 3401, 1955.

[27] H. Mirels. Boundary Layer behind Shock or Thin Expansion Wave moving into Stationary Fluid. NACA TN 3712, 1956.

[28] H. Mirels. Test Time in Low-Pressure Shock Tubes. The Physics of Fluids, Vol. 6, No. 9, pp. 1201-1214, 1963.

[29] H. Mirels. Shock Tube Test Time Limitation Due to Turbulent-Wall Boundary Layer. AIAA Journal, Vol. 2, No. 1, pp. 84-93, 1964.

[30] H. Mirels. Correlation Formulas for Laminar Shock Tube Boundary Layers. The Physics of Fluids, Vol. 9, No. 7, pp. 1265-1272, 1966.

[31] R. G. Morgan. Superorbital Expansion Tubes. In Proceeding of the 21st International Symposium on Shock Waves, Plenary Lecture, Vol. 1, 1997.

[32] D. M. Murray, O. R. Tutty and S. B. Gabriel. Numerical Modelling of Ion Thruster Hollow Cathode interior plasma flow. 35th Aerospace Sciences Meeting, Jan. 1997, AIAA 97-0793.

[33] P. J. Petrie-Repar and P.A. Jacobs. A Computational Study of Shock Speeds in High-Performance Shock Tubes. Shock Waves, Vol. 8, pp. 79-91, 1998.

[34] G. T. Roberts. Shock Tube Studies of Convective Heat Transfer. Ph. D. Thesis, University of Southampton, 1984.

[35] G. T. Roberts. Influence of Secondary Diaphragm on Flow Quality in Expansion Tubes. AASU Memo, University of Southampton, 1993.

[36] G. T. Roberts, R. G. Morgan and R. J. Stalker. Influence of Secondary Diaphragm on Flow Quality in Expansion Tubes. Shock Waves @ Marseille, Springer Verlag, pp. 203-208, 1995.

[37] P. L. Roe. Approximate Riemann Solver, Parameter Vectors and Difference Schemes. Journal of Computational Physics, Vol. 43, pp. 357-372, 1981.

[38] S. P. Sharma. Test-Times in Hypersonic Shock Tubes. AIAA Paper 95-0713, 33rd Aerospace Sciences Meeting and Exhibit, 1995.

[39] S. P. Sharma. Computations of Axisymmetric Flows in Hypersonic Shock Tubes. Journal of Thermophysics and Heat Transfer, Vol. 10, No. 1, pp. 169-176, 1996.

[40] Y. Sheng, J. P. Sislian and J. J. Liu. A Computational Technique for High Enthalpy Shock Tube and Shock Tunnel Flow Simulation. Shock Waves, Vol. 8, pp. 203-214, 1998.

[41] G. A. Sod. Numerical Methods in Fluid Dynamics: Initial and Boundary Value Problems. Cambridge University Press, 1985.

[42] E. F. Toro and R. E. Brown. The WAF Method and Splitting Procedures for Viscous Shocked Flows. In Proceeding of the 18th International Symposium on Shock Waves, Vol. 2, pp. 1119-1126, 1991.

[43] E. F. Toro, M. Spruce and W. Speares. Restoration of the Contact Surface in the HLL-Riemann Solver. Shock Waves, Vol. 4, pp. 25-34, 1994.

[44] E. F. Toro. Riemann Solvers and Numerical Methods for Fluid Dynamics A Practical Introduction. Springer-Verlag, 1999.

[45] R. L. Trimpi. A Preliminary Theoretical Study of the Expansion Tube, a New Device For Producing High-Enthalpy Short Duration Hypersonic Gas Flows. NASA Technical Report R-133, 1962.

[46] B. Van Leer. Towards the Ultimate Conservative Difference Scheme. V. A Second-Order Sequel to Godunov's Method. Journal of Computational Physics, Vol. 32, pp. 101-136, 1979.

[47] F. M. White. Viscous Fluid Flow. 2'nd. ed., McGraw Hill, New York, 1991.

[48] G. J. Wilson. Time-Dependent Quasi-One-Dimensional Simulations of High Enthalpy Pulse Facilities. AIAA Paper 92:5096, 1992.

[49] G. J. Wilson, S. P. Sharma and W. D. Gillespie. Time-Dependence Simulations of Reflected-Shock/Boundary Layer Interaction. AIAA Paper 93:0480, 1993.

[50] G. J. Wilson, M. A. Sussman and R. J. Bakos. Numerical Simulations of the Flow in the HYPULSE Expansion Tube. NASA TM 110357, 1995.

[51] H. C. Yee. A Class of High-Resolution Explicit and Implicit Shock-Capturing Methods. NASA TM 101088, 1989.

[52] H-r. Yu, B. Esser, M. Lenartz and H. Grönig. Gaseous Detonation Driver for a Shock Tunnel. Shock Waves, Vol. 2, pp. 245-254, 1992.